Научном већу Института за физику, Београд

Прегревица 118, Земун

Предмет: Реизбор Јелене Пешић у звање истраживач сарадник

МОЛБА

Молим научно веће Инситута за физику да покрене поступак за мој реизбор у звање истраживач сараник.

Прилажем:

- Мишљење руководиоца
- Стручну биографију
- Списак објављених радова
- Кратак преглед научне активности
- Фотокопије објављених радова
- Уверење о уписаним докторским студијама
- Копију решења о претходном избору у звање истраживач сарадник

У Београду,

07. 07. 2017. Године

Подносилац молбе

Јелена Пешић

Научном већу Института за физику, Београд

Предмет: Мишљење руководиоца пројекта о реизбору
Јелене Пешић и звање истраживач сарадник

        Докторант Јелена Пешић је запослена као истраживач приправник на пројекту «Физика уређених наноструктура и нових материјала у фотоници» , број 171005 од новембра 2013. 23. децембра 2014 је изабрана у звање истраживач сарадник
Докторант Јелена Пешић је активно ангажована на истраживањима из области графена и других дводимензионих материјала. Задужена за извођење нумеричких симулација и бави се испитивањем електрон-фононске интеракције у графену и другим дводимензионим материјалима методом теорије функционала густине. Фокус истраживања је на суперпроводност у допираном графену и монослоју магнезијум-диборида. Ангажована је и на експерименталном делу пројекта који се бави механички ексфолираним графеном и других 2Д материјала.
Јелена Пешић је до сад објавила осам радова, од тога 2 категорије М21а, 3 категорије М21 и 3 категорије М22.
У октобру 2016. (10. октобар 2016.) године докторанту Јелени Пешић је на Већу Универзитета у Београду усвојена тема докторске дисертације под називом: „Investigation of Superconductivity in Graphene and Related Materials Based on Ab-initio Methods" (Истраживање суперпроводности у графену и сличним материјалима коришћењем ab-initio метода). 23. јуна 2017. године Јелена Пешић је предала дисертацију Физичком факултету Универзитета у Београду. Одбрана дисертације се очекује у току јесени 2017. Године.
        Како кандидат Јелена Пешић испуњава све формалне и суштинске услове који су потребни за реизбор у звање истраживач сарадник, како од стране Министарства просвете, науке и технолошког развоја Републике Србије, тако и од стране Инситута за Физику Београд, Универзитет у Београду, сагласан сам са покретањем поступка у њен реизбор у звање истраживач сарадник.
        Предлажем комисију у саставу:

1. др Радош Гајић, научни саветник, Институт за физику, Београд

2. др Ненад Вукмировић, научни саветник, Институт за физику, Београд

3. др Владимир Дамљановић, научни сарадник Институт за физику, Београд

4. др Борислав Васић, научни сарадник, Институт за физику, Београд

5. др Саша Дмитровић, доцент, Физички факултет, Универзитет у Београду

У Београду,
07. 07. 2017. године

др Радош Гајић
Руководиоц пројекта ОИ171005

Стручна биографија

Јелена Пешић је рођена у Београду, општина Савски Венац, Република Србија, 17. децембра 1986. године. Основну школу и гимназију је завршила у Земуну. Основне студије је уписала 2005. године на Физичком факултету, Универзит у Београду, на смеру за Теоријску и експерименталну физику. Основне студије је завршила у јануару 2013. године са просеком од 8.9 и дипломским испитом 10, са темом дипломског рада: "Примена GPU програмирања у DFT прорачунима", ментор др Радош Гајић. Докторске студије је уписала на Физичком факултету, Универзитет у Београду, школске 2012/13. године, ужа научна област: Физика Кондензоване Материје и Статистичка Физика. У Центру за физику чврстог стања и нове материјале Института за физику у Београду је волонтирала од 01. фебруара 2013 године до 06. новембра 2013. године када је запослена као истраживач-приправник на пројекту ОИ171005 "Физика уређених наноструктура и нових материјала у нанофотоници". 23. децембра 2014 је изабрана у звање истраживач сарадник. У октобру 2016. године докторанту Јелени Пешић је на Већу Универзитета у Београду усвојена тема докторске дисертације под називом: „Investigation of Superconductivity in Graphene and Related Materials Based on Ab-initio Methods" (Истраживање суперпроводности у графену и сличним материјалима коришћењем ab-initio метода). За ментора је усвојен др Радош Гајић.
23. јуна 2017. године Јелена Пешић је предала дисертацију Физичком Факултету Универзитета у Београду. Одбрана дисертације се очекује у току јесени 2017. године.

Јелена Пешић се бави тероијским истраживањем електронских и вибрационих особина ако и електрон-фонон интерације у графену и сличним 2Д материјалима коришћењем ab-initio метода на бази тероије функционала густине (ДФТ). Ангажована је и на експерименталном делу пројекта који се бави механички ексфолираним графеном и других 2Д материјала.

За време докторских студија Јелена Пешић је учествовала у три интернационалана пројекта. Први је пројекат билатералне сарадње са НР Кином и Универзитетом у Шангају, који се бави специфичним собинама нормалног стања у суперпроводном REBCO кристалу. Други је билатерални пројекатса Аустријом, Универзитет у Леобену и трећи јер пројекат Texas A & M Универзитета у Катару који се бави истраживањем утицаја субстрата на интеркалирани графен. У току 2015 године Јелена Пешић је учествовала и на пројекту билатералне сарадње са Немачком, Универзитет у Потсдаму, о коришћењу графена као заштитног слоја за органске наноструктуре. У јануару 2017. Јелена Пешић је учествовала на у школи "Advanced Workshop on High-Performance & High-Throughput Materials Simulations using Quantum ESPRESSO"организованој од стране International Center for

Theoretical Physics у Трсту, Италија. Током докторских студија је остварила сарадњу са Johannes Kepler Универзитетом у Линцу, Аустрија, као сарадник у оквиру Zentrum für Oberflächen- und Nanoanalytik који води проф. др. Курт Хингерл. У периоду 2014-2015 Јелена Пешић је учествовала у иновационом пројекту Министарства просвете, науке и технолошког развоја Републике Србије који је истраживао коришћење течних дисперзија графена као мастила за флексибилну штампану електронику.

До сад има објаљених 8 радова у међународним часописима, 2 категорије М21а, 3 категорије М21 и 3 категорије М22., и 14 учешћа на конференцијама и школама. Додатно у току писања овог извештаја Јелена Пешић има један рад на рецензији и један у припреми за слање у међународни часопис.

Списак публикација кандидата

РАДОВИ У МЕЂУНАРОДНИМ ЧАСОПИСИМА ИЗУЗЕТНИХ ВРЕДНОСТИ (М21А):

- Matković A., Milošević I., Milićević M., Tomašević-Ilić T., **Pešić J**., Musić M., Spasenović M., Jovanović Đ, Vasić B., Deeks C., Panajotović R., Belić M. and Gajić R., „Enhanced sheet conductivity of Langmuir–Blodgett assembled graphene thin films by chemical doping" 2D Mater. 3 015002 (2016)

- Prinz, J., Matković, A., **Pešić, J.**, Gajić, R. and Bald, I, "Hybrid Structures for Surface-Enhanced Raman Scattering: DNA Origami/Gold Nanoparticle Dimer/Graphene" Small, doi:10.1002/smll.201601908 (2016)

РАДОВИ У ВРХУНСКИМ МЕЂУНАРОДНИМ ЧАСОПИСИМА (М21):

- **Pešić J.**, Damljanović V., Gajić R., Hingerl K. and Belić M., „Density functional theory study of phonons in graphene doped with Li, Ca and Ba" EPL, 112 6 67006 (2015)

- **Pešić J.** , Gajić R., Hingerl K. and Belić M., "Strain-enhanced superconductivity in Li-doped graphene", EPL 108 67005 (2014)

- Matković A., Vasić B., **Pešić J**., Prinz J., Bald I., Milosavljević A. and Gajić R., „Enhanced structural stability of DNA origami nanostructures by graphene encapsulation", New J. Phys. 18 025016 (2016)

РАДОВИ У ИСТАКНУТИМ МЕЂУНАРОДНИМ ЧАСОПИСИМА (М22):

- **Pešić J.** and Gajić R., „Ab-initio study of the optical properties of the Li-intercalated graphene and MoS2", Opt Quant Electron, 48:368 (2016)

- **Pešić J.**, and R. Gajić. "Advantages of GPU technology in DFT calculations of intercalated graphene" Phys. Scr.T162 014027 (2014)

- Tomašević-Ilić T., **Pešić J.**, Milošević I., Vujin J., Matković A., Spasenović M., Gajić R. „Transparent and conductive films from liquid phase exfoliated graphene", Opt. Quant. Electron. 48:319 (2016)

ПРЕДАВАЊЕ ПО ПОЗИВУ СА МЕЂУНАРОДНОГ СКУПА ШТАМПАНО У ИЗВОДУ М32:

- A. Matković, I. Milošević, M. Milićević, A. Beltaos, T. Tomašević-Ilić, **J. Pešić**, M. M. Jakovljević, M. Musić, U. Ralević, M. Spasenović, Dj. Jovanović, B. Vasić, G. Isić and R. Gajić "Spectroscopic and Scanning Probe Microscopic Investigations and Characterization of Graphene", *XIX Symposium on Condensed Matter Physics, SFKM 2015,* Beograd, Srbija, 07.09.2015 - 11.09.2015, str 32

САОПШТЕЊЕ СА МЕЂУНАРОДНОГ СКУПА ШТАМПАНО У ИЗВОДУ М34:

- **J. Pešić**, I. Popov, V. Damljanović, R. Gajić, "Enhancement of electron-phonon coupling in alkali-doped graphene and thin MgB2 layers" *18th International Workshop on Computational Physics and Materials Science: Total Energy and Force Methods* January 12-14, 2017 Miramare, Trieste, Italy

- M. Spasenović, T.Tomašević-Ilić, **J. Pešić**, A. Matković, R. Gajić, "Transparent and Conductive Films With Liquid Phase Exfoliated Graphene" *Researcher and Society* 2016, Marie Curie Alumni Association (MCAA), Velika Britanija, 28.07.2016, - 29.07.2016,

- B. Vasić, A. Matković, **J. Pešić**, J. Prinz, I. Bald, A. Milosavljević, R. Gajić, "Graphene as a protective coating for macromolecules: AFM manipulation study", *The Second European Workshop on Understanding and Controlling Nano and Mesoscale Friction* 2016, COST Action MP1303, Letonija, 04.07.2016, - 07.07.2016

- M. Spasenović, T.Tomašević-Ilić, **J. Pešić**, A. Matković, R. Gajić, "Transparent and Conductive Films With Liquid Phase Exfoliated Graphene", *Euroscience Open Forum (ESOF) (M34)*, 2016, EuroScience Foundation (ESF), Velika Britanija, 23.07.2016, - 27.07.2016,

- J. Prinz, A. Matković, **J. Pešić**, B. Vasić, I. Bald, "DNA origami-gold nanoparticle-graphene double hybrid structures for surface-enhanced Raman scattering", DNA-Nanotechnoliogy, Jena, Nemačka, 19.05.2016 – 21.05.2016.

- **J. Pešić,** R.Gajić "Ab-initio study of optical properties of alkali metal-intercalated graphene and MoS2", *Photonica 2015,* 978-86-7306-131-3, Beograd, Srbija, 24.08.2015 - 28.08.2015., str 193

- T. Tomašević-Ilić, **J. Pešić,** I. Milošević, J. Vujin, A. Matković, M. Spasenović, R. Gajić "Transparent and conductive films from liquid phase exfoliated graphene" *Photonica 2015,* 978-86-7306-131-3, Beograd, Srbija, 24.08.2015 - 28.08.2015., str. 191

- A. Matković, I. Milošević, M. Milićević, T. Tomašević-Ilić, **J. Pešić,** M. Musić, M. Spasenović, Dj. Jovanović, B. Vasić, M. R. Belić and R. Gajić, "Chemical Doping of

Langmuir-Blodgett Assembled Graphene Films for Flexible Transparent Conductive Electrodes" *XIX Symposium on Condensed Matter Physics, XIX Symposium on Condensed Matter Physics, SFKM 2015,* Beograd, Srbija, 07.09.2015 - 11.09.2015, str. 93

- **J. Pešić** , R. Gajić, "Density Functional Theory Study of Li and Ti-Intercalated graphene", *XIX Symposium on Condensed Matter Physics, SFKM 2015,* Beograd, Srbija, 07.09.2015 - 11.09.2015, str. 99

- **J. Pešić**, V. Damljanović, R. Gajić, M. Milićević, K. Hingerl, "Density Functional Theory Study of Phonons in mono and bilayer intercalated graphene"*10 years from the discovery of graphene"* 2014, Univ. of Patras & FORTH/ICE-HT, Patras, Grčka, 14.07.2014 - 17.07.2014,

- A. Matković, M. Milićević, I. Milošević, **J. Pešić**, B. Vasić, M. Spasenović, R. Gajić, "Relating nanoscopic structure to macroscopic properties of liquid-phase exfoliated graphene", *13th Young Researchers' Conference – Materials Science and Engineering* 2014, Beograd, Srbija, 10.12.2014 - 12.12.2014, str 71.

- **J. Pešić**, V. Damljanović, R. Gajić, "First Principle Calculation of Phonons and Electron-Phonon Interaction in Graphene", *13th Young Researchers' Conference – Materials Science and Engineering* 2014, Beograd, Srbija, 10.12.2014 - 12.12.2014, str 19.

- **J. Pešić**, R. Gajić, ", Advantages of GPU technology on the DFT" *IV International School and Conference on Photonics-PHOTONICA'13 ,* 2013, 978-86-82441-36-6, Beograd, Srbija, 26.08.2013 - 30.08.2013, str 100

Научна активност кандидата

Јелена Пешић се бави теоријским истраживањем графена и сличних дводимензионих материјала коришћењем ab-initio метода заносваних на теорије функционала густине (ДФТ). Фокус истраживања је на електрон-фононској интеркацији у овим материјалима и појави суперпроводности.

У току досадашњег рада на овој теми Јелена Пешић је објавила **три рада у међународним часописима**. Прву целину истраживања чини проучавање монослоја графена допираног алкалним металима (литијум, баријум и калцијум) по узору на интеркалирани графит. Електронске и вибрационе особине су проучаване у овим материјалима а посебно електрон-фононска интеркација у графену допираном литијумом. Изучавана је могућност појачања електрон-фононске интеракције и подизање критичне температуре применом механичких модификација, тј напрезања/истезања. Показано је да применом двоосовинског истезања, због омекшавања фононских мода, долази до појачања електрон-фононске интеракције и повећања критичне температуре до 29К. У оквиру ове целине проучаване су и оптичке особине монослоја графена допираног литијумом.

Друга целина се бави новим дводимензионим суперпроводним материјалом, структурно и електронски сличном графену, монослоју магнезијум-диборида. Истраживање обухвата проучавње електронске и фононске слике у овом материјалу, студију стабилности и симетријску анализу овог материјала. Електрон-фононска интеркација и суперпроводност су проучавани и дискутована је паралела са допираним графеном. Показано је да монослој магнезијум-диборида има критичну температуру на 18К. По узору на претходну целину, проучавана је могућност појачања електрон-фононске интеракције применом напрезања/истезања где је показано да се критична температура може повећати до 31К. Резултати овог истраживања су у процесу објављивања у време подношења овог извештаја.

Идеја истраживања није само појединачно проучавање дводимензионих суперпроводних материјала већ и тражење заједничких особина и правилности уз циљу бољег разумевања суперпроводноси у нискодимензионим материјалима као и могућности предвиђања нових суперпроводних материјала.

Истраживање Јелена Пешић обухвата још две додатне целине. Трећа целина је проучавање примене хардверских убрзања у ДФТ прорачунима. Фокус је на истраживању коришћења графичких процесора (ГПУ) у прорачунима нискодимензионих материјала. Ово истраживање је објављено **у једном раду у међународном часопису** а у току је припрема још једне публикације на ову тему. Четврта целина обухвата експериментално истраживање графена и других дводимензионих материјала. Јелена Пешић се бави механичком ексфолијацијом графена и његовом применом као заштитног слоја за наноструктуре али и применом течно-ексфолираног графена у макроскопским применама, као проводно мастило за штампу, за флексибилну електронику итд. У оквиру експерименталног истраживања Јелена Пешић је коаутор на **четири публикације у међународним часописима**.

Strain-enhanced superconductivity in Li-doped graphene

JELENA PEŠIĆ[1], RADOŠ GAJIĆ[1], KURT HINGERL[2] and MILIVOJ BELIĆ[3]

[1] *Institute of Physics, University of Belgrade - Pregrevica 118, 11080 Belgrade, Serbia*
[2] *Center for Surface and Nanoanalytics, Johannes Kepler University - Linz, Austria*
[3] *Science Program, Texas A&M University at Qatar - P.O. Box 23874, Doha, Qatar*

Abstract – We present a new way to enhance the electron-phonon coupling constant and the critical superconducting temperature of graphene, significantly beyond all reported values. Using density functional theory, we explore the application effects of the tensile biaxial strain on the lithium-intercalated graphene. Both effects together, the presence of adatom and the strain, trigger the enhancement of critical temperature, up to 300%, compared to non-strained lithium-intercalated graphene.

Introduction. – Graphene, a single atomic layer of carbon atoms arranged in a honeycomb lattice, has been attracting remarkable attention for its unique properties ever since it was successfully isolated in 2004 [1]. As the first case of real-2D atomic crystals (MoS_2, BN, $NbSe_2$, Bi_2Te_3, InSe), graphene proved to be an interesting system with properties essentially different from 3D objects. In addition, due to a hexagonal lattice with two carbon atoms per unit cell, the electronic spectrum of graphene has a Dirac cone analog to relativistic massless fermions. As a consequence, the chiral Dirac electrons appear, resulting in peculiar quantum effects like Klein tunneling [2], Zitterbewegung of electrons [3,4] or anomalous quantum Hall effect [5,6]. On the other hand, the electron-phonon interaction in graphene is also quite interesting. Namely, because of the specific Fermi surface, there is a pronounced Kohn anomaly like in graphite [7] around Γ and K points [8]. In addition, the peculiar electronic band structure of graphene gives rise to the breakdown of the adiabatic Born-Oppenheimer approximation [9]. Extraordinary effects in graphene make it a promising material for future research as well as for various applications. Nevertheless, one important effect has been missing on the list of graphene exceptional properties so far. This is superconductivity that has not been observed yet neither in pristine nor in doped graphene although considerable theoretical efforts have been invested in exploring possible pairing instabilities [10–12].

Particularly, the existence of superconductivity in graphene has been a highly investigated subject in the past few years. Various superconducting mechanisms have been extensively researched. Numerous superconducting models in graphene have been proposed, *e.g.*, a chiral superconductivity [13], an interlayer pairing of chiral electrons [14] as well as many other exotic pairing mechanisms [15] that have been studied [16]. Whereas all these theoretical studies result in the possible appearance of the superconductivity in graphene, the electron-phonon mechanism is still the most probable cause for potential superconductivity. Nonetheless, this is the naturally first choice in the search for superconductivity in 2D carbon layer, pristine as well as the intercalated one [17–21]. Moreover, the phonon-mediated superconductivity has been observed and proven by photoemission spectroscopy [22] in graphite-intercalated compounds [23–26].

Strong electron-phonon coupling could be caused by a large number of carriers, strong deformation potentials, and coupling of electrons and phonon modes at low energies. Unfortunately pristine graphene does not fulfil any of these. The enhancement of coupling to the out-of-plane vibrations is an imperative for appearance of superconductivity so the new states at the Fermi level should be introduced, in a manner similar to the graphite-intercalated compound (GIC). Intercalation of atoms into the layered materials has been known as a method of introduction of new properties in the pristine materials [27].

GIC doped with various alkaline atoms displays superconductivity in many cases [24–26]. In the superconducting GIC at the Fermi level, an interlayer band has been formed and it enhances the electron-phonon coupling constant λ [26]. Therefore, due to the presence of interlayer band, the number of carriers is augmented, the coupling to carbon out-of-plane vibrations is enhanced and there is coupling to the intercalant vibrations as well. The electron-phonon coupling constant is proportional to the DOS at the Fermi level and the deformational potential D and inversely proportional to the square of phonon frequency of the mode coupled to electrons

$$\lambda = \frac{N(0)D^2}{M\,\omega_{ph}^2}. \tag{1}$$

In eq. (1) ω_{ph} is the phonon frequency of the phonon vibrations involved in superconductivity, $N(0)$ is the electronic DOS per spin at the Fermi level and M is an effective atomic mass. For the appearance of superconductivity it is necessary to have the charge transfer to graphene layer, but also the interlayer band must be formed on the Fermi level. The electron-phonon coupling constant increases with the deformation potential D which depends on the distance between adatoms and the graphene, h. The smaller the distance is, the larger D becomes. The distance h cannot be decreased infinitely, since a too small h will cause a complete charge transfer and an upshift of the intercalant band, which then becomes empty and forms above the Fermi level. Another important prerequisite for the introduction of superconductivity is the existence of coupling between carbon out-of-plane vibrations and electrons (which is essential since the coupling with in-plane vibration is not large enough and λ has small value). This is achieved by the transitions between the graphene π^* states and the interlayer band.

The different intercalants and geometries allow tuning of the properties of carbon, producing the largest increase in T_c (for calcium-doped graphite it is $11.5\,\mathrm{K}$) [25,28,29]. Although GICs show interesting properties, not all types of intercalant atoms produce superconductivity or significantly increase T_c. It seems that the charge transfer from the interlayer is crucial. Though charge transfer is necessary, the completion of the charge transfer is deleterious for the enhancement of the superconductivity. In some of GICs, the charge transfer between adatom and graphene is incomplete and they display a superconductivity, on the other hand, like Li-GIC, where the charge transfer is complete resulting in low T_c ($0.9\,\mathrm{K}$). In the Li-GIC, a strong confinement for electrons along the z-axis exists and it prevents occupation of the interlayer state. Because the quantum confinement is removed in monolayer [18,30] this results in the reduction of charge transfer and it is beneficial for superconductivity. Thus the Li-doped graphene is shown to be superconductive ($8.1\,\mathrm{K}$) with much higher T_c than in Ca-doped graphene ($1.4\,\mathrm{K}$). After the superconductivity in Li-intercalated graphene has been established, much attention has been devoted to the study of
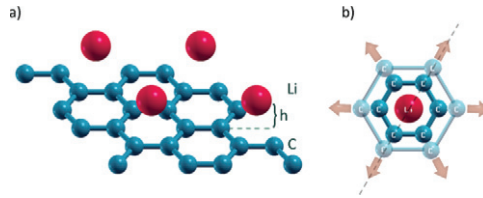

Fig. 1: (Color online) (a) Lithium-intercalated graphene, h is the adatom graphene distance. (b) Schematic description of biaxial tensile strain.

its enhancement [31–33]. As a conclusion beside to the Li doping, an increase of electron-phonon paring potential is necessary. In order to increase λ, the phonon frequencies must be softened.

Based on this concept, we study the effects of the tensile equibiaxial strain on the Li-intercalated graphene. Application of the strain is an intensively studied topic, both in theory and experiment [34–37]. Namely, an application of strain on graphene can induce changes of the vibrational properties [38,39], in the electronic band gaps [40,41] and significant changes in conductivity both at local and macroscopic level [42–44]. The type of the strain is a very important feature, since the graphene lattice symmetry determines its band structure. The breaking of the hexagonal symmetry will modify the band structure of graphene [8,45], causing the opening of the band gap and many other effects [46,47]. Since our intention is to soften modes, without drastically modifying the structure, the tensile equibiaxial strain is employed in the calculations on the lithium-intercalated graphene (LiG) (fig. 1(b)). Here it is shown that such a strain causes softening of the phonons, in particular, the in-plane phonons will be dramatically softened, whereas the out-of-plane ones will be less affected [47]. This greatly affects λ.

We investigate the enhancement of the electron-phonon interaction in LiG using the first-principle density functional theory (DFT) calculation in the local density approximation (LDA) and based on the prior discussion, we find that λ is sensitive to the tensile equibiaxial strain, therefore producing a higher T_c. For instance, the strain of 10% makes a T_c increase of almost 300%!

Computational details. – As mentioned above, we employed DFT with LDA [48], using Quantum Espresso (version 5.0.3) [49]. The ionic positions in the cell are fully relaxed, in all calculations, to their minimum energy configuration using the Broyden-Fletcher-Goldfarb-Shanno (BFGS) algorithm. The hexagonal cell parameter c was set to $c = 12.5\,\text{Å}$ in order to simulate a two-dimensional system and avoid an interaction due to periodicity. The norm-conserving pseudopotential and the plane wave cutoff energy of $65\,\mathrm{Ry}$ were used in the calculation. Although DFT with LDA may have problems in application in certain situations where electronic correlations are strong, for graphene, with large electronic bands, it is quite a suitable assumption [47,50]. As stated before,

Table 1: Physical properties of graphene under different values of tensile equibiaxial strain.

Strain %	h distance (Å)	C-C bond lenght (Å)	λ	$\omega_{\log}$	T_c
0%	1.80	1.42	0.61	278.88	8.1
3%	1.69	1.46	0.47	876.17	6.42
5%	1.64	1.49	0.49	976.20	9.43
7%	1.61	1.52	0.55	1009.05	14.73
10%	1.54	1.57	0.73	827.09	28.72

there is the Kohn anomaly. Although DFT is known to underestimate the electron-exchange correlation energy in the presence of the Kohn anomaly [51], the usage of DFT here is justified. The differences appear only in a small portion of the first Brillouin zone and do not lead to significant inconsistencies when the electron interaction with entire phonon system is observed [52]. The unit cell for the LiG monolayer was modeled in the $\sqrt{3} \times \sqrt{3}$R 60° in-plane unit cell, consisting of one Li atom placed above the center of the carbon hexagon, with an adatom-graphene distance $h = 1.8$ Å. (fig. 1). λ was calculated with the electron momentum k-mesh up to $40 \times 40 \times 1$ and the phonon q-mesh $20 \times 20 \times 1$. The Eliashberg function is defined as

$$\alpha^2 F(\omega) = \frac{1}{N(0)N_k N_q} \sum_{n\mathbf{k},\ m\mathbf{q},\nu} \left| g^\nu_{n\mathbf{k},\ mk+\mathbf{q}} \right|^2 \\ \times \delta(\varepsilon_{n\mathbf{k}})\delta(\varepsilon_{m\mathbf{k+q}})\delta(\omega - \omega^\nu_{\mathbf{q}}),$$

where $N(0)$ is the total DOS per spin and N_k and N_q are the total numbers of k and q points, respectively. The electron eigenvalues are labelled with the band index (n and m) and the wave vector (k and $k+q$), while the phonon frequencies with the mode number (ν) and the wave vector (q). $g^\nu_{n\mathbf{k},\ mk+\mathbf{q}}$ represents the electron-phonon matrix element. The total electron-phonon coupling $\lambda(\omega)$ is given:

$$\lambda(\omega) = 2 \int_0^\omega \mathrm{d}\omega' \frac{\alpha^2 F(\omega')}{\omega'}. \quad (2)$$

The superconducting critical temperature was estimated using the Allen-Dynes formula with $\mu^* = 0.112$ [53]

$$T_c = \frac{\omega_{\log}}{1.2} \exp\left[\frac{-1.04(1+\lambda)}{\lambda(1-0.62\mu^*) - \mu^*} \right], \quad (3)$$

where

$$\omega_{\log} = \exp\left[\frac{2}{\lambda} \int \frac{\mathrm{d}\omega}{\omega} \alpha^2 F(\omega) \log \omega \right]. \quad (4)$$

Results. – In order to strain the LiG monolayer and increase the lattice constant, the in-plane distance between C atoms is increased leaving the hexagonal symmetry preserved. The Li adatom is placed above the H site in graphene (the center of hexagon) (fig. 1), which, according to DFT study is the favorable adsorption site [54]. The modification of the lattice constant does not interfere with
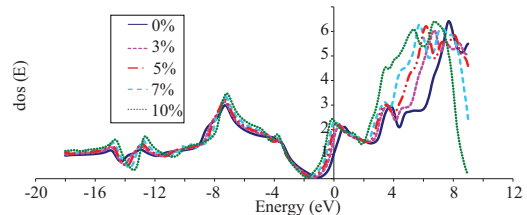

Fig. 2: (Color online) Electron density of states for LiC6 under tensile equibiaxial strain.

the Li adatom position which remains fixed in the center of the hexagon, leaving the symmetry unbroken. Due to the expansion of the carbon atom distances and the invariance of the hexagonal symmetry, the Li adatom shifts only along the z-axis. The effects of several values of the strain, which increase the lattice constant by 3%, 5%, 7%, and 10%, are studied. Larger strains are not applied due to the instabilities that occur after the attempt of geometrical optimization and relaxation.

Table 1 presents the physical parameters of the Li-doped graphene under the various strains. The distance between the Li adatom and graphene decreases with the strain, as the Li adatom moves down deeper towards graphene. When strain is applied, the distance between neighboring C atoms increases and the graphene π bonds less repulse the Li adatom, which then moves down along the z-axis. In fig. 2, the electron DOS is shown. The small shift of the Fermi level can be observed with the strain. Here it is worth mentioning that in graphene, a truly 2D system with low electron density, the long-range Coulomb force is weakly screened and the electron-electron interaction cannot be neglected. The two-dimensionality in graphene can cause enhanced excitonic effects, like the M-point exciton [55,56] or the charge density waves (CDWs) formation (the Peierls transition) as a result of the Fermi nesting. Especially an interplay between superconductivity and CDWs seems to be important [57,58]. Namely, CDWs make a pre-existing environment for superconductivity [59]. Various strains in graphene have been studied as a method for the introduction of different broken symmetry phases. CDWs in graphene have been thoroughly investigated both theoretically [60–63] and experimentally [64] showing interesting results. For instance, the presence of axial magnetic field caused by a buckle
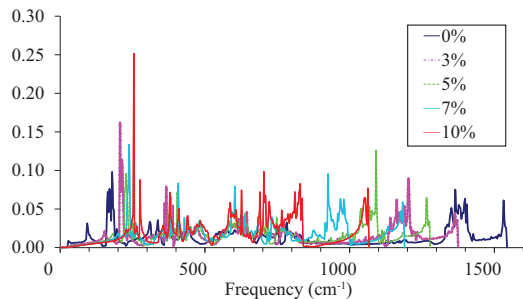
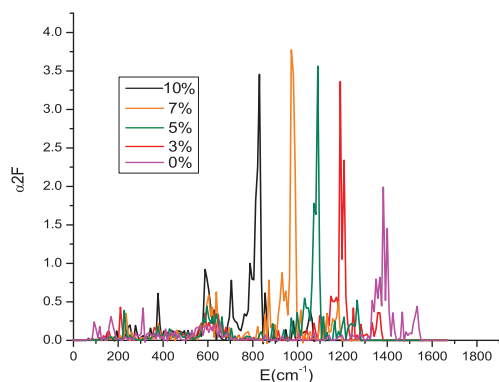Fig. 3: (Color online) Comparison of phonon DOS for various strains.

Fig. 5: (Color online) Electron-phonon coupling constant behavior with tensile equibiaxial strain.

Fig. 4: (Color online) Comparison of Eliashberg function for equibiaxial strain.

strain can lead to realization of CDWs [60]. Also, in CaC_6 electron-electron repulsion is dominant within graphene sheets [64] producing the CDW stripes. In the case of strained LiG, DOS near the Dirac point gets enhanced (fig. 2), hence the question about interplay of electron-electron and electron-phonon interaction can be imposed. The problem of CDW in graphene, doped and strained, is discussed comprehensively and its very existence in LiG is not in conflict with our discussion and results. Moreover, CDW and superconductivity appear together in different systems like high-T_c superconductors or intercalated graphite [57–59] and can be even used as a criterion for high-temperature superconductivity.

Considerable changes are present in the phonons. In the phonon dispersion spectrum three regions can be distinguished: the adatom-related modes are associated with low-energy regions (0–400 cm^{-1}), where 300–400 cm^{-1} are Li modes mixed with the out-of-plane carbon modes (C_z), the mid-region (400–900 cm^{-1}) can be associated with C_z modes and the high-energy region with carbon-carbon stretching modes [18]. The main contributions to λ come from the low-energy lithium modes and the carbon vibrations along the z-axis, with an additional contribution from the C-C stretching modes (in agreement with [18] and [30]).

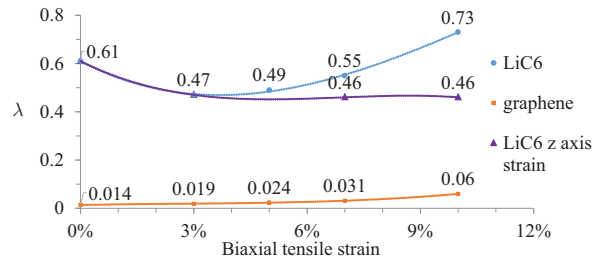Phonon density of states (PDOS) as a function of strain is depicted in fig. 3. Although low-energy modes slightly move upwards in energy, the main effect on the electron-phonon coupling is the softening of graphene high energy C-C stretching modes. They significantly soften with the strain. In contrast to non-strained LiG, the stretching modes have a main influence on λ (fig. 4). The Eliashberg spectral function (fig. 4) describes which phonon modes couple with the electrons on the Fermi level. The intensity of the Eliashberg function is greatly increased in the area of the C-C stretching modes, with the strain. This results in a great increase of λ and T_c. For 10% tensile equibiaxial strain we get $\lambda = 0.73$ and $T_c = 29$ K. λ is presented as function of strain in fig. 5. It is worth mentioning that there is a reduction in λ for small values of strain (0–3%) (fig. 5). Particularly, with strain, the C-C bonds expand, causing a decrease of the Coulomb repulsion between the π orbitals and the Li adatom. That allows the Li adatom to come down toward the center on the graphene hexagon. As emphasized before, a too small intercalant-graphite layer distance in the GIC is destructive for superconductivity. On the other hand, this effect vanishes for larger strains, while an increase in T_c, even up to three times larger than the value reported for non-strained LiG, can be observed. This effect is associated to an overlap of the carbon π and the Li orbitals.

For small strain, the Li adatom drops down toward the center of hexagon and its orbitals overlap more with the carbon π orbitals. That causes an increase in charge transfer and emptying of the interlayer band, which reduces λ. When more strain is applied, the carbon bonds are elongated and the π orbitals move away, both from each other and the center of the hexagon. The orbital overlap is reduced, and after the certain critical value, λ increases, following the strain (circle in fig. 5). In order to corroborate this interpretation, we perform two additional calculations: the calculation on non-strained graphene, where the Li adatom position is shifted along the z-axis; and the second one with the strained pristine graphene. Here it is proven that an increase of λ is a mutual effect of strain and doping. For the first calculation, the π orbitals remain fixed in their positions (since there is no strain). The overlap with the Li and π orbitals increases and one can clearly see that λ is decreased (violet triangles in fig. 5) due to an approach to the charge transfer completion and emptying of the interlayer band. The effects of the strain on
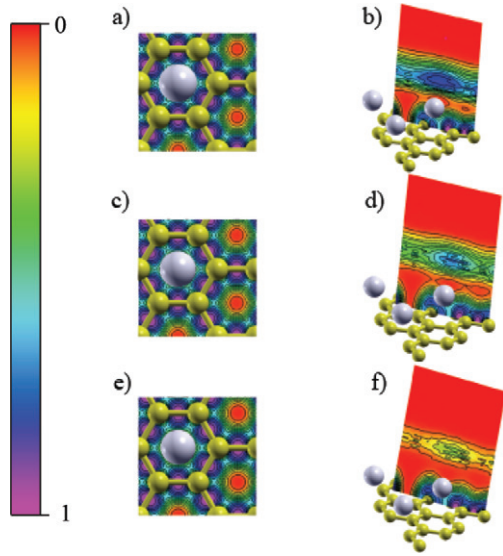
Fig. 6: (Color online) ELF (electron localization function) for LiG with strain: (a) ELF for LiG without strain on the xy plane; (b) ELF for LiG without strain on the xz plane; (c) ELF for LiG for 5% strain on the xy plane; (d) ELF for LiG for 5% strain on the xz plane; (e) ELF for LiG for 10% strain on the xy plane; (f) ELF for LiG for 10% strain on the xz plane. In panels (a), (c) and (e) we can see slight changes in ELF projected on the xy plane, localization region at Li adatom is enlarged. In panels (b), (d) and (f) are shown effects of strain, projected on the xz plane. Notable change is present for 10% of strain, where electron localization region is significantly lowered due to the described effects.

the pristine graphene λ are also depicted in fig. 5 (orange squares). Graphene has a very small λ which is increased with strain almost four times, but effect of this enhancement is negligible ($\lambda = 0.06$).

On the other hand, fig. 6 presents the effects of the different strain on electronic localization function (ELF). The significant changes for the large strain are presented, proving the above-described effects. For ELF at 10% of the strain, the electron localization region is greatly lowered as graphene and adatom separate one from another and as a C-C bond are elongated.

As expected, the strain alone will not boost the λ considerably, nor the doping itself. A complex mechanism of the enhancement is a mutual effect of the mechanical effects with the presence of the interlayer level, all owing to the unique structure of graphene. For the notable enhancement of λ the presence of both the adatom and the strain is essential.

Conclusions. – In this work, using DFT, we have studied the effects of tensile equibiaxial strain on the enhancement of λ in the LiG. Since no symmetry is broken, there are no major changes in the electronic structure of the system. On the other hand, strain softens the phonon modes significantly. The critical temperature is enhanced by the strain, up to $T_c = 29\,\mathrm{K}$ where the electron-phonon

coupling constant is 0.73. We conclude that both the presence of the adatom and the strain are necessary for the enhancement of λ. It is important to stress that this increase in T_c, achieved by the described mechanism, can be experimentally realized. A pristine graphene is experimentally confirmed to be elastically stretchable up to 25% [37]. A recent study confirms the fabrication of the intercalated graphene [65] which additionally raises an interest in such compounds and their properties. Therefore, an experimental realization of the high-T_c superconducting intercalated graphene is to be anticipated, opening a completely new field of graphene applications.

$$* * *$$

REFERENCES

[1] NOVOSELOV K. S., GEIM A. K., MOROZOV S. V., JIANG D., ZHANG Y., DUBONOS S. V., GRIGORIEVA I. V. and FIRSOV A. A., *Science*, **306** (2004) 666.
[2] KATSNELSON M. I., NOVOSELOV K. S. and GEIM A. K., *Nat. Phys.*, **2** (2006) 620.
[3] KATSNELSON M. I., *Eur. Phys. J. B*, **51** (2006) 157.
[4] RUSIN T. M. and ZAWADZKI W., *Phys. Rev. B*, **78** (2008) 125419.
[5] ZHANG Y., TAN Y., STORMER H. L. and KIM P., *Nature*, **438** (2005) 201.
[6] NOVOSELOV K. S., JIANG Z., ZHANG Y., MOROZOV S. V., STORMER H. L., ZEITLER U., MAAN J. C., BOEBINGER G. S., KIM P. and GEIM A. K., *Science*, **315** (2007) 1379.
[7] PISCANEC S., LAZZERI M., MAURI F., FERRARI A. C. and ROBERTSON J., *Phys. Rev. Lett.*, **93** (2004) 85503.
[8] ZHOU S. Y. *et al.*, *Nat. Mater.*, **6** (2007) 770.
[9] PISANA S., LAZZERI M., CASIRAGHI C., NOVOSELOV K. S., GEIM A. K., FERRARI A. C. and MAURI F., *Nat. Mater.*, **6** (2007) 198.
[10] ZHAO E. and PARAMEKANTI A., *Phys. Rev. Lett.*, **97** (2006) 230404.
[11] ROY B. and HERBUT I. F., *Phys. Rev. B*, **82** (2010) 035429.
[12] HONERKAMP C., *Phys. Rev. Lett.*, **100** (2008) 146404.
[13] NANDKISHORE R., LEVITOV L. S. and CHUBUKOV A. V., *Nat. Phys.*, **8** (2012) 158.
[14] HOSSEINI M. V. and ZAREYAN M., *Phys. Rev. Lett.*, **108** (2012) 147001.
[15] ROY B. and JURICIC V., *Phys. Rev. B*, **90** (2014) 041413.
[16] VUCICEVIC J., GOERBIG M. O. and MILOVANOVIC M. V., *Phys. Rev. B*, **86** (2012) 214505.
[17] EINENKEL M. and EFETOV K. B., *Phys. Rev. B*, **84** (2011) 214508.

[18] PROFETA G., CALANDRA M. and MAURI F., *Nat. Phys.*, **8** (2012) 131.

[19] LOZOVIK Y. and SOKOLIK A., *Phys. Lett. A*, **374** (2010) 2785.

[20] MAZIN I. and BALATSKY A., *Philos. Mag. Lett.*, **90** (2010) 731.

[21] DIETEL J., BEZERRA V. H. F. and KLEINERT H., *Phys. Rev. B*, **89** (2014) 195435.

[22] VALLA T. and PAN Z., *Physics and Applications of Graphene - Experiments*, edited by MIKHAILOV S. (InTech) 2011.

[23] CALANDRA M. and MAURI F., *Phys. Rev. Lett.*, **95** (2005) 237002.

[24] JISHI R. A. and DRESSELHAUS M. S., *Phys. Rev. B*, **45** (12465).

[25] EMERY N., HÉROLD C., D'ASTUTO M., GARCIA V., BELLIN C., MARÊCHÉ J. F., LAGRANGE P. and LOUPIAS G., *Phys. Rev. Lett.*, **95** (2005) 087003.

[26] DRESSELHAUS M., DRESSELHAUS G., EKLUND P. and CHUNG D., *Mater. Sci. Eng.*, **31** (1977) 141.

[27] ATTACCALITE C., WIRTZ L., LAZZERI M., MAURI F. and RUBIO A., *Nano Lett.*, **10** (2010) 1172.

[28] WELLER T. E., ELLERBY M., SAXENA S. S., SMITH R. P. and SKIPPER N. T., *Nat. Phys.*, **1** (2005) 39.

[29] SAVINI G., FERRARI A. C. and GIUSTINO F., *Phys. Rev. Lett.*, **105** (2010) 037002.

[30] CALANDRA M., PROFETA G. and MAURI F., *Phys. Status Solidi B*, **12** (2012) 2544.

[31] SZCZNIAK D., DURAJSKI A. P. and SZCZNIAK R., *J. Phys.: Condens. Matter*, **26** (2014) 255701.

[32] KALONI T. P., BALATSKY A. V. and SCHWINGENSCHLÖGL U., *EPL*, **104** (2013) 47013.

[33] GUZMAN D. M., ALYAHYAEI H. M. and JISHI R. A., *2D Mater.*, **1** (2014) 021005.

[34] NI Z. H., YU T., LU Y. H., WANG Y. Y., FENG Y. P. and SHEN Z. X., *ACS Nano*, **11** (2008) 2301.

[35] HUANG M., YAN H., CHEN C., SONG D., HEINZ T. F. and HONE J., *Proc. Natl. Acad. Sci. U.S.A.*, **106** (2009) 7304.

[36] PEREIRA V. M., CASTRO NETO A. H. and PERES N. M. R., *Phys. Rev. B*, **80** (2009) 045401.

[37] LEE C., WEI X., KYSAR J. W. and HONE J., *Science*, **321** (2008) 385.

[38] DING F., JI H., CHEN Y., HERKLOTZ A., DORR K., MEI Y., RASTELLI A. and SCHMIDT O. G., *Nano Lett.*, **10** (2010) 3453.

[39] MOHIUDDIN T. M. G. *et al.*, *Phys. Rev. B*, **79** (2009) 205433.

[40] LEVY N., BURKE S. A., MEAKER K., PANLASIGUI M. L., ZETTL A., GUINEA F., NETO A. H. C. and CROMMIE M. F., *Science*, **329** (2010) 544.

[41] GUINEA F., KATSNELSON M. I. and GEIM A. K., *Nat. Phys.*, **6** (2009) 30.

[42] TEAGUE M. L., LAI A. P., VELASCO J., HUGHES C. R., BEYER A. D., BOCKRATH M. W., LAU C. N. and YEH N.-C., *Nano Lett.*, **9** (2009) 2542.

[43] HUANG M., PASCAL T. A., KIM H., GODDARD W. A. and GREER J. R., *Nano Lett.*, **11** (2011) 1241.

[44] FU X.-W., LIAO Z.-M., ZHOU J. X., ZHOU Y.-B., WU H.-C., ZHANG R., JING G., XU J., WU X., GUO W. and YU D., *Appl. Phys. Lett.*, **99** (2011) 213107.

[45] XIAO D., YAO W. and NIU Q., *Phys. Rev. Lett.*, **99** (2007) 236809.

[46] GUI G., LI J. and ZHONG J., *Phys. Rev. B*, **78** (2008) 075435.

[47] MARIANETTI C. A. and YEVICK H. G., *Phys. Rev. Lett.*, **105** (2010) 245502.

[48] PERDEW J. P. and ZUNGER A., *Phys. Rev. B*, **23** (1981) 5048.

[49] GIANNOZZI P. *et al.*, *J. Phys.: Condens. Matter*, **21** (2009) 395502.

[50] KOTLIAR G. *et al.*, *Rev. Mod. Phys.*, **78** (2006) 865.

[51] LAZZERI M., ATTACCALITE C., WIRTZ L. and MAURI F., *Phys. Rev. B*, **78** (2008) 081406.

[52] BORYSENKO K. M., MULLEN J. T., BARRY E. A., PAUL S., SEMENOV Y. G., ZAVADA J. M., NARDELLI M. B. and KIM K. W., *Phys. Rev. B*, **81** (2010) 121412(R).

[53] ALLEN R. B. and DYNES R. C., *Phys. Rev. B*, **12** (1975) 3.

[54] CHAN K. T., NEATON J. B. and COHEN M. L., *Phys. Rev. B*, **77** (2008) 235430.

[55] MATKOVIC A., RALEVIC U., ISIC G., JAKOVLJEVIC M. M., VASIC B., JOVANOVIC DJ., MILOSEVIC I., MARKOVIC D. and GAJIC R., *Phys. Scr.*, **T149** (2012) 014069.

[56] MATKOVIC A., BELTAOS A., MILICEVIC M., RALEVIC U., VASIC B., JOVANOVIC DJ. and GAJIC R., *J. Appl. Phys.*, **112** (2012) 123523.

[57] SILVA NETO E. H., AYNAJIAN P., FRANO A., COMIN R., SCHIERLE E., WESCHKE E., GYENIS A., WEN J., SCHNEELOCH J., XU Z., ONO S., GU G., LE TACON M. and YAZDANI A., *Science*, **343** (2014) 6169.

[58] COMIN R., FRANO A., YEE M. M., YOSHIDA Y., EISAKI H., SCHIERLE E., WESCHKE E., SUTARTO R., HE F., SOUMYANARAYANAN A., HE YANG, LE TACON M., ELFIMOV I. S., HOFFMAN J. E., SAWATZKY G. A., KEIMER B. and DAMASCELLI A., *Science*, **343** (2014) 6169.

[59] CHANG J., BLACKBURN E., HOLMES A. T., CHRISTENSEN N. B., LARSEN J., MESOT J., LIANG R., BONN D. A., HARDY W. N., WATENPHUL A., ZIMMERMANN M. V., FORGAN E. M. and HAYDEN S. M., *Nat. Phys.*, **8** (2012) 871.

[60] ROY B. and SAU D. J., *Phys. Rev. B*, **90** (2014) 075427.

[61] KOTOV N. V., UCHOA B., PEREIRA M. V., GUINEA F. and CASTRO NETO A. H., *Rev. Mod. Phys.*, **84** (2012) 1067.

[62] KHEVSHCHENKO D. V., *Phys. Rev. Lett.*, **87** (2001) 246802.

[63] TŐKE C. and FAL'KO V. I., *Phys. Rev. B*, **90** (2014) 035404.

[64] RAHNEJAT K. C., HOWARD C. A., SHUTTLEWORTH N. E., SCHOFIELD S. R., IWAYA K., HIRJIBEHEDIN C. F., RENNER CH., AEPPLI G. and ELLERBY M., *Nat. Commun.*, **2** (2011) 558.

[65] YANG S. L. *et al.*, *Nat. Commun.*, **5** (2014) 3493.

Density functional theory study of phonons in graphene doped with Li, Ca and Ba

Jelena Pešić[1], Vladimir Damljanović[1], Radoš Gajić[1], Kurt Hingerl[2] and Milivoj Belić[3]

[1] *Institute of Physics, University of Belgrade - Pregrevica 118, 11080, Belgrade, Serbia*
[2] *Center of Surface and Nanoanalytics, Johannes Kepler University - Linz, Austria*
[3] *Science Program, Texas A&M University at Qatar - P.O. Box 23874, Doha, Qatar*

Abstract – Vibrational frequencies and phonon displacement patterns of the H-site doped graphene are calculated by the density functional theory (DFT). DFT calculations, as well as the group theory study, are used to describe these structures as interesting materials for single layer superconductivity. In this paper, graphene doped with Li, Ca and Ba adatoms is systematically analysed and compared. Due to the effect of zone folding, displacement patterns of calculated modes correspond to the ones of the K and Γ point phonons of graphene and this offers the possibility for comparison with the experimental results for graphene. Our objective was to provide compendious and practical guidelines for the experimental research and characterization of these structures.

Introduction. – Graphene, an atom thick honeycomb lattice of carbon atoms, for the past ten years has been rapidly changing materials science. Ever since its discovery [1] in 2004, graphene's unique properties and interesting phenomena, like quantum Hall effect [2,3], Klein tunneling [4] and electronic correlations [5] have been drawing the attention of the scientific population. The mutual influence of electrons and phonons in graphene is a highly debated topic and the origin of some very interesting phenomena. The semi-metallic character of its electronic structure is an important issue in understanding the behavior of phonons. The atomic vibrations are partially screened by electrons but in metal this screening can change rapidly for vibrations associated with certain q points which are determined by the shape of the Fermi surface [6]. Graphene is a material where the adiabatic Bohr-Openheimer approximation [7] is no longer valid, which means electrons relax non-adiabatically to the lattice motion and that leads to the softening of phonon. Such anomalous behaviour of phonon dispersion is called Kohn anomaly [6]. It may occur only for q such that there are two electron states, k_1 and $k_2 = k_1 + q$, both on the Fermi surface [8]. For graphene, the electronic gap is zero only at two Brillouin zone points K and $K' = 2K$

so we know that the Kohn anomaly occurs at $q = \Gamma$ and $q' = K$. The Kohn anomaly can be experimentally observed in graphene with Raman spectroscopy (Γ point) [6,9–11].

The opto-electronic properties of graphene and graphite are directly affected by their environmental conditions and adatoms in graphene. As a result, the phonons appearing because of the structural re-arrangement of the system tend to change and displace as a function of doping, strain and electronic conditions in the structure [12]. Moreover, the theoretical studies treating superconductivity [13,14] indicate that the dominant pairing mechanism is an electron-phonon interaction [15]. Graphite intercalation compounds (GICs) [16,17] show various fascinating physical properties which pristine graphite lacks, and intercalation of graphene offers new possibilities for both applications and fundamental research. Superconductivity has been discovered in the bulk graphite intercalated with calcium ($T_c = 11.5\,\mathrm{K}$) or ytterbium ($T_c = 6.5\,\mathrm{K}$) [16,18,19]. The recent studies of graphene doping with the alkali metals and a comparison to GICs, both theoretical and experimental, have brought up new exciting questions, like superconductivity in low-dimensional systems [20–23]. With regard

to fundamental research, the most interesting question is a recent prediction that Li covered graphene (LiC$_6$-mono) is superconducting [22,24,25]. The Li intercalated graphite is debated to be superconducting, with the theoretical predicted critical temperature of $0.9\,$K [24] but an experimental realization was never demonstrated [26]. The more interesting phenomenon is superconductivity in the two-dimensional limit, where the Li-doped graphene has the critical temperature of $8.1\,$K [24]. In this paper, we used DFT to calculate vibrational frequencies and displacement patterns at the Γ point for Li, Ca and Ba-doped graphene (LiC$_6$-mono, CaC$_6$-mono and BaC$_6$-mono, respectively). These materials have been studied for their superconducting properties [22,24,25,27,28]. Describing phonons in the doped monolayer graphene is important for the understanding of the electron-phonon coupling and the appearence of superconductivity in this materials. The dopant-related vibrations are crucial for achieving superconductivity [29] and phonon softening is shown to be an indication of a strong electron-phonon coupling enhancing superconductivity [25]. A detailed description, as in this paper, could be used as a practical guide for an experimental research, identifying and characterizing these materials, and as a theoretical ground for further research. The recent experimental and theoretical studies of the electron-phonon coupling and superconductivity in single layer iron-selenides [30,31] strengthen the need for a quality description of phonons in the monolayer superconductive structures, like the doped monolayer graphene. Due to the fact that DFT and DFPT (density functional perturbation theory [32]) (used for this work) are based on the adiabatic Born-Oppenheimer approximation, which is not sufficient for the study of the Kohn anomaly, necessary analytical corrections are required for certain modes. The group theory methods are additionally used to support the calculation. Finally *ab initio* results are compared to experimental data for graphene.

Computational details. – All results reported here are obtained from the first-principles calculations, DFT in the local density approximation (LDA), using the Quantum Espresso program package [33]. The ionic positions in the cell are fully relaxed, in all calculations, to their minimum energy configuration using the Broyden-Fletcher-Goldfarb-Shanno (BFGS) algorithm. The hexagonal cell parameter c was set to $c = 12.5\,$Å in order to simulate a two-dimensional system and avoid an interaction due to periodicity. The norm-conserving pseudopotential [34] and the plane wave cutoff energy of 65–75 Ry are used in the calculation, accordingly convergence is achieved with an error less than 1% for all calculated frequencies, by varying values of the plane wave energy cutoff. The unit cell for the H-site doped monolayer was modeled in the $\sqrt{3} \times \sqrt{3}\,$R60° in-plane unit cell, consisting of one adatom placed above the center of the carbon hexagon. According to the DFT study [35], the favorable adsorption site, for Li, Ca and Ba adatoms on the surface of

graphene, is above the center of the graphene hexagon called H-site. This configuration has been theoretically studied as an optimal structure [22,24] and experimentally realised for the Li-doped monolayer [23] and Ca-doped bilayer graphene [21]. The adatom-graphene distance for LiC$_6$-mono is $h = 1.8\,$Å, for CaC$_6$-mono $h = 2.04\,$Å, for BaC$_6$-mono $h = 2.17\,$Å. The phonon frequencies are determined by the DFPT for evaluating the effects of the adatoms on the phonon spectrum. All calculations are performed at the Γ point of the Brillouin zone. The symmetry groups of these structures are $Dg80 = TD_{6h}$ for pristine graphene and $Dg77 = TC_{6v}$ for graphene doped at the H-site [36,37]. All groups are diperiodic (*i.e. Dg*) and represented as a semi-direct product of the translational subgroup T and a point group. Translational subgroups of these symmetry groups need not to be mutually identical.

Results and discussion. – Total energies for all considered structures and graphene are calculated and, as expected, graphene doped at the H-site has a higher total energy than graphene. This does not represent an obstacle for stability. If the provided reservoir of adatoms is large enough, adatoms will be adsorbed in graphene, because the thermodynamical potential is a grand-canonical one and then becomes minimized:

$$-k_B T \ln \mathcal{Z} = \Phi_G = \langle E \rangle - TS - \mu \langle N \rangle. \tag{1}$$

The transfer of the adatoms on the graphene will reduce $\mathcal{Z}$, even if μ is small.

We begin with the group theory discussion and the symmetry assignment of the modes. The symmetry group $Dg77 = T'C_{6v}$ of the H-site adatom doped graphene is a subgroup of the diperiodic group $Dg80 = TD_{6h}$, a symmetry group of graphene. In order to find which of the phonon modes of the H-site adatom doped graphene monolayer corresponds to a certain phonon mode of graphene, it was necessary to reduce the corresponding irreducible representation of group $Dg80$ to its subgroup $Dg77$. For the modes belonging to the Γ point:

$$\begin{aligned} \Gamma E_{2g}(Dg80) \downarrow Dg77 &= \Gamma E_2, \\ \Gamma B_{1g}(Dg80) \downarrow Dg77 &= \Gamma B_1. \end{aligned} \tag{2}$$

($\downarrow$ is the notation for the subduction operation). Since the translational subgroup of these diperiodic groups is represented by the number one in irreducible representations belonging to the Γ point, the formulae (2) are obtained using the point group character tables (see, *e.g.*, [38]). For the modes belonging to the K point, the characters of $Dg80$ for irreducible representations at this point [39] are necessary. The reduction procedure gives

$$\begin{aligned} KA_1'(Dg80) \downarrow Dg77 &= \Gamma A_1 + \Gamma B_2, \\ KA_2'(Dg80) \downarrow Dg77 &= \Gamma A_2 + \Gamma B_1, \\ KE'(Dg80) \downarrow Dg77 &= KE''(Dg80) \downarrow Dg77 = \\ \Gamma E_1 + \Gamma E_2. \end{aligned} \tag{3}$$
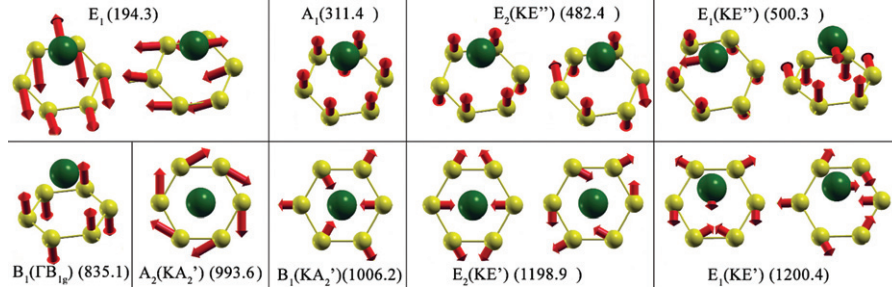
Fig. 1: (Color online) Vibrational frequencies (in wave numbers) and displacement patterns for the monolayer LiC$_6$-mono. The modes of graphene with a similar displacement pattern are denoted in parentheses.

Fig. 2: (Color online) Vibrational frequencies (in wave numbers) and displacement patterns for the monolayer CaC$_6$-mono. The modes of graphene with a similar displacement pattern are denoted in parentheses.

Fig. 3: (Color online) Vibrational frequencies (in wave numbers) and displacement patterns for the monolayer BaC$_6$-mono. The modes of graphene with a similar displacement pattern are denoted in parentheses.

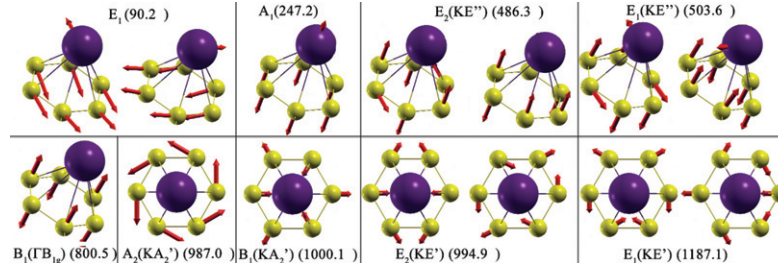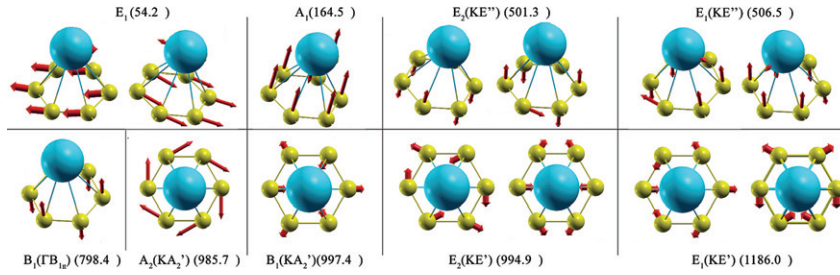Therefore, the modes ΓB_{1g}, ΓE_{2g}, KA_1', KA_2', KE', KE'' of graphene correspond to the modes B_1, E_2, A_1 and B_2, A_2 and B_1, E_1 and E_2, E_1 and E_2 for the graphene doped at the H-site, respectively. There is a perfect agreement with the irreducible representation shown in figs. 1–3. T' is a translational subgroup of $Dg77$ while T is translational subgroup of $Dg80$. T' is a subgroup of T such that for all elements of T' the phase factor $\cos(\vec{k}_K \cdot \vec{R})$ is equal to one. This factor appears in the characters of irreducible representations of $Dg80$ for the K point [39]. The vibrational frequencies and displacement patterns for the LiC$_6$-mono, CaC$_6$-mono, BaC$_6$-mono are shown in fig. 1, fig. 2, fig. 3, respectively (visualization [40]). For all compounds, true acoustic mode (with $\omega = 0$ at the Γ point) are not represented. Also, modes where Kohn annomaly is present are not presented. For all H-site doped graphene, the two lowest modes can be related to three acoustic modes of graphene. Therefore, their frequencies are the lowest. The remaining modes have displacement patterns

similar to graphene phonons at the Γ and K points. This is indicated in fig. 4 (Kohn anomaly is marked with red) and it is a consequence of the Brillouin zone folding. The K point of graphene became equivalent to the Γ point of H-site doped graphene, due to the reduction of the basis vectors length in the reciprocal space [17]. This reduction is caused by an increase in the size of the primitive cell in direct space, as depicted in fig. 5. The K point of the Brillouin zone (BZ) of graphene is folded to the Γ point of the reconstructed BZ in the H-site doped graphene and the phonon bands at the Γ and K points in graphene are ascribed to the folded superstructure, as shown in fig. 4. The Γ point is the same for both structures. The displacement patterns of phonons at high symmetry points of the BZ of monolayer graphene can be determined solely by symmetry arguments [41–43]. For the complete system of eigenvectors of the honeycomb lattice at the Γ and K points, see ref. [43]. There are several reports on the experimental realization of doped graphene [29,44–46]. None of
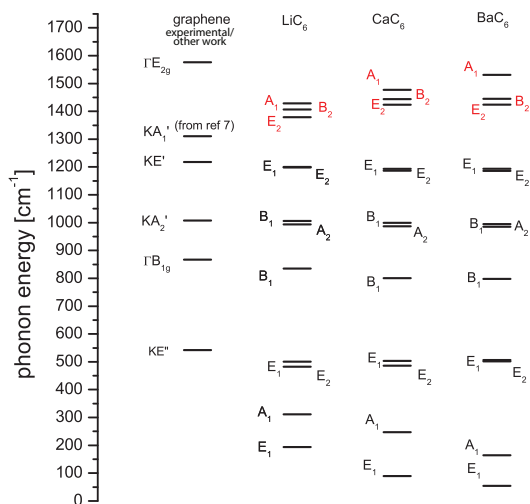
Fig. 4: (Color online) Comparison of calculated vibration frequencies for various stacking and experimental data. Modes which require non-adiabatic corrections are marked in red. The experimental values are taken from ref. [47].

Fig. 5: (Color online) (a) Unit cell of pristine graphene (black) and H-site doped graphene (red); (b) corresponding BZ.

them contains Raman or infra-red spectra of these structures. Therefore, we compared our results with inelastic X-ray scattering experiments on graphite [47]. In this paper graphite is considered as a system of weakly interacting graphene sheets. The bonds between the two carbon atoms in the plane are much stronger than the weak van der Waals interactions between the layers. The graphite phonon modes correspond approximately to the in-phase and out-of-phase vibrations of the two graphene planes. Most of the phonon branches in graphite are almost the same as in graphene [6,47]. The group of wave vectors for all H-site doped graphene at the Γ point is C_{6v}. The modes of E_2 symmetry are Raman active while those of the A_1 and E_1 symmetries are both Raman and infrared active. According to ref. [47], the experimentally determined values for phonon frequencies are $542\,\mathrm{cm^{-1}}$, $867\,\mathrm{cm^{-1}}$, $1007\,\mathrm{cm^{-1}}$, $1218\,\mathrm{cm^{-1}}$, $1576\,\mathrm{cm^{-1}}$, for KE'', ΓB_{1g}, KA_2', KE', ΓE_{2g}, respectively, while the KA_1' mode is unresolved (its value is known from other *ab initio* calculations, and it is $1310\,\mathrm{cm^{-1}}$ [6]). If we compare our calculated modes with experimental data [47], small discrepancies exist due to the presence of the adatoms. Significant discrepancies can be seen for modes related to the Kohn anomaly. In graphene, the Kohn anomaly exists in E_{2g} and KA_1' modes due to strong electron-phonon coupling. The fact that the Kohn anomaly can be observed in a two-dimensional system is quite remarkable since this phenomenon is typical for one-dimensional systems. The Kohn anomaly can be observed and measured using Raman spectroscopy [6]. As mentioned before, the zone folding effects in graphene occur because the graphene's unit cell consists of two carbon atoms, where the presence of an additional adatom enlarges the unit cell. This affects the electron [21] and phonon configuration as well. Comparing the phonon dispersion relations
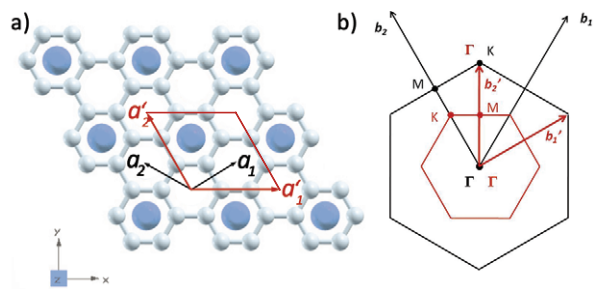
of the pristine and doped graphene, the phonon bands along the ΓK direction in graphene correspond to the ones at the H-site doped graphene along the $\Gamma M \Gamma'$ direction. A small shift in energies can be observed due to the adatom presence. In the phonon dispersion relations of doped graphene one can distinguish three regions: the low-energy region (0–$400\,\mathrm{cm^{-1}}$) with the adatom-related modes, the mid-energy region (400–$900\,\mathrm{cm^{-1}}$) can be associated with the C_z and the high-energy region consisting of the carbon-carbon stretching modes [24]. Comparing the phonon dispersion bands, like in fig. 6 for graphene and LiC$_6$-mono, one can see how, due to the zone folding, graphene's Γ and K point modes correspond to the Γ modes of the H-site doped graphene with small discrepancies which originate due to the presence of an adatom. For the graphene's out-of-plane optical phonon (Γ at $867\,\mathrm{cm^{-1}}$ [47]) and the corresponding H-site doped graphene's mode there is a discrepancy in energies which depends on the type of adatom (different shifts appear for the Li, Ba and Ca doping). A similar behaviour appears for the two optical in-plane modes of graphene and its corresponding H-site doped ones. Due to the zone folding, it is also expected that the Kohn anomaly will be also present in modes which are related to these two. All frequencies in this paper are computed by the static perturbation theory of the DFT energy, from the linearized forces acting on the atoms due to the static displacement of the other atoms from their equilibrium positions. As stated, a DFT approach is based on the adiabatic Born-Oppenheimer approximation, which is broken for graphene so modes where the Kohn anomaly appears require a dynamic approach, *i.e.* time-dependent perturbation theory. As a conclusion, our calculated frequencies, for modes where the Kohn anomaly does not exist, are in a satisfying agreement with those reported in [47]. There is a discrepancy around 10% (10–$90\,\mathrm{cm^{-1}}$ depending on the mode) between experimental results for graphene presented in [47] and calculated energies of graphene-related modes, that we can attribute to the presence of the adatom in H-site doped graphene. The occurrence of non-adiabatic effects in the GIC is observed and studied [48] thoroughly. In Li, Ca and Ba GIC, for modes with present Kohn anomaly, non-adiabatic correction is
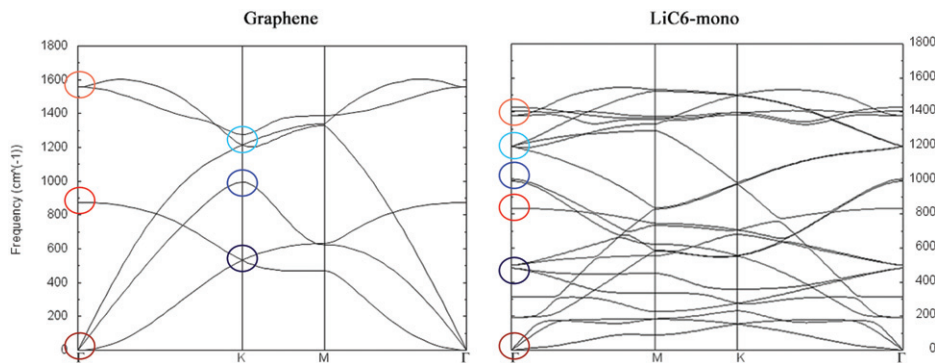
Fig. 6: (Color online) Phonon dispersion for graphene and LiC$_6$-mono. Red circles mark modes in the Γ point and blue circles at the K point. Due to the zone folding, graphene modes from the Γ and K points fold to modes in the Γ point at LiC$_6$-mono.

Table 1: Raman tensors and symmetry classification of optical modes for doped monolayer graphene.

	Raman tensors		
graphene $Dg80 = TD_{6h}$ $O_z \parallel C_6$ $O_x \parallel C'_2$	A_{1g} $\begin{pmatrix} a & 0 & 0 \\ 0 & a & 0 \\ 0 & 0 & b \end{pmatrix}$	E_{1g} $\begin{pmatrix} 0 & 0 & 0 \\ 0 & 0 & c \\ 0 & c & 0 \end{pmatrix} \begin{pmatrix} 0 & 0 & -c \\ 0 & 0 & 0 \\ -c & 0 & 0 \end{pmatrix}$	E_{2g} $\begin{pmatrix} d & 0 & 0 \\ 0 & -d & 0 \\ 0 & 0 & 0 \end{pmatrix} \begin{pmatrix} 0 & -d & 0 \\ -d & 0 & 0 \\ 0 & 0 & 0 \end{pmatrix}$
$A\alpha$ $Dg77 = TC_{6v}$ $O_z \parallel C_6$ $O_x \parallel \sigma_v$	A_1 $\begin{pmatrix} a & 0 & 0 \\ 0 & a & 0 \\ 0 & 0 & b \end{pmatrix}$	E_1 $\begin{pmatrix} 0 & 0 & c \\ 0 & 0 & 0 \\ c & 0 & 0 \end{pmatrix} \begin{pmatrix} 0 & 0 & 0 \\ 0 & 0 & c \\ 0 & c & 0 \end{pmatrix}$	E_2 $\begin{pmatrix} d & 0 & 0 \\ 0 & -d & 0 \\ 0 & 0 & 0 \end{pmatrix} \begin{pmatrix} 0 & -d & 0 \\ -d & 0 & 0 \\ 0 & 0 & 0 \end{pmatrix}$
	Optical modes		
$A\alpha$	$\Gamma_{opt} = 2A_1 + A_2 + 2B_1 + B_2 + 3E_1 + 3E_2$		

less than 20%. ($\Delta\omega$ for E_{2g} mode in Li GIC is $218\,\text{cm}^{-1}$, Ca GIC is $83\,\text{cm}^{-1}$ and for Ba GIC is $59\,\text{cm}^{-1}$ [48].) It is expected that the doped graphene has the same correction since we considered graphite as a system of weakly interacting graphene sheets. In all cases, the vibrational frequencies for modes with displacement pattern similar to the corresponding phonon in monolayer graphene are almost the same. The frequency splitting is due to the presence of the adatoms. The Raman tensors and optical modes [49] for all considered structures are summarized in table 1.

Conclusions. – In summary, by using DFT, we have calculated the vibration frequencies and displacement patterns of the Γ point phonons for monolayer graphene doped with lithium, calcium and barium. We found that they have a similar displacement pattern as those for graphene at the Γ and K points. We presented the group theoretical analysis that demonstrates the correspondence between phonon modes of graphene and the H-site doped graphene. A satisfying agreement with experimental data [47] additionally supports these calculations. The results provided in this work are important for the characterization of those structures and their further investigation and application. Graphene doped with other alkali adatoms, in a manner of GIC, is an interesting direction

for future research. A recent study [23] has shown the first successful experimental realisation of monolayer Li-doped graphene. Using angle-resolved photoemission spectroscopy (ARPES) it is shown that Li deposited on graphene at low temperature strongly modifies the phonon density of states, leading to an enhancement of the electron-phonon coupling, which is the first experimental proof of superconductivity in graphene. Hopefully our work will stimulate further experimental studies for doped graphene and its remarkable properties.

$* * *$

REFERENCES

[1] Novoselov K. S., Geim A. K., Morozov S. V., Jiang D., Zhang Y., Dubonos S. V., Grigorieva I. V. and Firsov A. A., *Science*, **306** (2004) 666.

[2] Zhang Y., Tan Y. W., Stormer H. L. and Kim P., *Nature*, **438** (2005) 201.

[3] Novoselov K. S., Jiang Z., Zhang Y., Morozov S. V., Stormer H. L., Zeitler U., Maan J. C., Boebinger G. S., Kim P. and Geim A. K., *Science*, **315** (2007) 1379.

[4] Katsnelson M. I., Novoselov K. S. and Geim A. K., *Nat. Phys.*, **2** (2006) 620.

[5] Kotov V. N., Uchoa B., Pereira V. M., Guinea F. and Castro Neto A. H., *Rev. Mod. Phys.*, **84** (2012) 1067.

[6] Piscanec S., Lazzeri M., Mauri Francesco, Ferrari A. C. and Robertson J., *Phys. Rev. Lett.*, **93** (2004) 185503.

[7] Pisana S., Lazzeri M., Casiraghi C., Novoselov K. S., Geim A. K., Ferrari A. C. and Mauri F., *Nat. Mater.*, **6** (2007) 198.

[8] Kohn W., *Phys. Rev. Lett.*, **2** (1959) 393.

[9] Piscanec S., Lazzeri M., Robertson J., Ferrari A. C. and Mauri F., *Phys. Rev. B*, **75** (2014) 035427.

[10] Lazzeri M., Piscanec S., Mauri F., Ferrari A. C. and Robertson J., *Phys. Rev. B*, **73** (2006) 155426.

[11] Lazzeri M., Piscanec S., Mauri F., Ferrari A. C. and Robertson J., *Phys. Rev. Lett.*, **95** (2005) 236802.

[12] Chacón-Torres J. C., Wirtz L. and Pichler T., *Phys. Status Solidi. B*, **251** (2014) 2337.

[13] Boeri L., Bachelet G. B., Giantomassi M. and Andersen O. K., *Phys. Rev. B*, **76** (2007) 064510.

[14] Castro Neto A. H., Guinea F., Peres N. M. R., Novoselov K. S. and Geim A. K., *Rev. Mod. Phys.*, **81** (2009) 109.

[15] Sanna A., Profeta G., Floris A., Marini A., Gross E. K. U. and Massidda S., *Phys. Rev. B*, **75** (2007) 020511.

[16] Weller T. E., Ellerby M., Saxena S. S., Smith R. P. and Skipper N. T., *Nat. Phys.*, **1** (2005) 39.

[17] Dresselhaus M. S., Dresselhaus G., Eklund P. C. and Chung D. D. L., *Mater. Sci. Eng.*, **31** (1977) 141.

[18] Calandra M. and Mauri F., *Phys. Rev. Lett.*, **95** (2005) 237002.

[19] Emery N., Hérold C., d'Astuto M., Garcia V., Bellin Ch., Marêché J. F., Lagrange P. and Loupias G., *Phys. Rev. Lett.*, **95** (2005) 087003.

[20] Yang S.-L., Sobota J. A., Howard C. A., Pickard C. J., Hashimoto M., Lu D. H., Mo S.-K., Kirchmann P. S. and Shen Z.-X., *Nat. Commun.*, **5** (2014) 3493.

[21] Kanetani K., Sugawara K., Sato T., Shimizu R., Iwaya K., Hitosugi T. and Takahashi T., *Proc. Natl. Acad. Sci. U.S.A.*, **109** (2012) 19610.

[22] Calandra M., Profeta G. and Mauri F., *Phys. Status Solidi (b)*, **249** (2012) 2544.

[23] Ludbrook B., Levy G., Nigge P., Zonno M., Schneider M., Dvorak D., Veenstra C., Zhdanovich S., Wong D., Dosanjh P., Strasser C., Stohr A., Forti S., Ast C., Starke U. and Damascelli A., *Proc. Natl. Acad. Sci. U.S.A.*, **112** (2015) 11795.

[24] Profeta G., Calandra M. and Mauri F., *Nat. Phys.*, **8** (2012) 131.

[25] Pešić J., Gajić R., Hingerl K. and Belić M., *EPL*, **108** (2014) 67005.

[26] Pan Z.-H., Camacho J., Upton M. H., Fedorov A. V., Howard C. A., Ellerby M. and Valla T., *Phys. Rev. Lett.*, **106** (2011) 187002.

[27] Csanyi G., Littlewood P. B., Nevidomskyy A. H., Pickard C. J. and Simons B. D., *Nat. Phys.*, **1** (2005) 42.

[28] Kaloni T. P., Balatsky A. V. and Schwingenschlgl U., *EPL*, **104** (2013) 47013.

[29] Fedorov A. V., Verbitskiy N. I., Haberer D., Struzzi C., Petaccia L., Usachov D., Vilkov O. Y., Vyalikh D. V., Fink J., Knupfer M., Bchner B. and Grüneis A., *Nat. Commun.*, **5** (2014) 3257.

[30] Ge J.-F., Liu Z.-L., Liu C., Gao C.-L., Qian D., Xue Q.-K., Liu Y. and Jia J.-F., *Nat. Mater.*, **14** (2015) 285.

[31] Koufos A. P. and Papaconstantopoulos D. A., *Phys. Rev. B*, **89** (2014) 035150.

[32] Baroni S., de Gironcoli S., Dal Corso A. and Giannozzi P., *Rev. Mod. Phys.*, **73** (2001) 515.

[33] Giannozzi P. *et al.*, *J. Phys.: Condens. Matter*, **21** (2009) 395502.

[34] Perdew J. P. and Zunger Alex, *Phys. Rev. B*, **23** (1981) 5048.

[35] Ji Zhi, Contreras-Torres Flavio F., Jalbout Abraham F. and Ramrez-Trevio Alberto, *Appl. Surf. Sci.*, **285** (2013) 846.

[36] Milošević I., Nikolić B., Damnjanović M. and Krčmar M., *J. Phys. A: Math. Gen.*, **31** (1988) 3625.

[37] Wood E. A., *Bell Syst. Tech. J.*, **43** (1964) 541.

[38] Altmann S. L. and Herzig P., *Point-Group Theory Tables* (Clarendon Press, Oxford; Oxford University Press, New York) 1994.

[39] Damljanović V., Kostić R. and Gajić R., *Phys. Scr.*, **T162** (2014) 014022.

[40] Kokalj A., *Comput. Mater. Sci.*, **28** (2003) 155.

[41] Damljanović V., Kostić R. and Gajić R., *Rom. Rep. Phys.*, **65** (2013) 193.

[42] Mapelli C., Castiglioni C., Zerbi G. and Müllen K., *Phys. Rev. B*, **60** (1999) 12710.

[43] Damljanović V. and Gajić R., *Phys. Scr.*, **T149** (2012) 014067.

[44] Sugawara K., Kanetani K., Sato T. and Takahashi T., *AIP Adv.*, **1** (2011) 022103.

[45] Virojanadara C., Watcharinyanon S., Zakharov A. A. and Johansson L. I., *Phys. Rev. B*, **82** (2010) 205402.

[46] Kumar A., Leela A., Reddy M., Mukherjee A., Dubey M., Zhan X., Singh N., Ci L., Billups W. E., Nagurny J., Mital G. and Ajayan P. M., *ACS Nano*, **5** (2011) 4345.

[47] Mohr M., Maultzsch J., Dobardžić E., Reich S., Milošević I., Damnjanović M., Bosak A., Krisch M. and Thomsen C., *Phys. Rev. B*, **76** (2007) 035439.

[48] Marco Saitta A., Lazzeri M., Calandra M. and Mauri F., *Phys. Rev. Lett.*, **100** (2008) 226401.

[49] Poulet H. and Mathieu J. P., *Vibration Spectra and Symmetry of Crystals* (Gordon and Breach, New York, London, Paris) 1976.

CrossMark

Ab-initio study of the optical properties of the Li-intercalated graphene and MoS₂

Jelena Pešić[1] · **Radoš Gajić[1]**

Abstract Ab-initio calculations based on density functional theory have been performed to study the optical properties of the Li intercalated graphene and MoS₂. Comparative study of imaginary part of dielectric function for the Li doped, pristine graphene monolayer and their bulk counterparts has been done. The dielectric matrix has been calculated using the Quantum Espresso software package and its postprocessing code epsilon.x. The presented results show reliable qualitative description especially for computationally inexpensive calculation.

Keywords Graphene · Optical properties · MoS₂ · DFT

1 Introduction

In the past ten years the discovery of the graphene (Novoselov et al. 2004) and other 2D materials had started a completely new chapter in the material science. Graphene, a single atomic layer of carbon atoms arranged in a honeycomb lattice, has been attracting a remarkable attention for its unique properties (Zhang et al. 2005; Novoselov et al. 2007; Katsnelson et al. 2006; Kotov et al. 2012) ever since it was successfully isolated in 2004. Graphene's specific electronic structure and unique combination of the optical electronic properties have risen numerous investigations of its optoelectronic properties and possible applications in photonics, energy applications and detectors. Graphene electrical conductivity and visual transparency makes it excellent candidate for ITO replacement in touch

✉ Jelena Pešić
   yelena@ipb.ac.rs

1   Institute of Physics Belgrade, University of Belgrade, Pregrevica 118, Belgrade 11080, Serbia

screen technology. Graphitic films (films of various thicknesses, monolayer to ultrathin graphite) are explored for its possible applications in optoelectronics. Several studies have presented excellent performances of graphene films of 30 Ω per square at 90 % transmittance for doped four layer CVD graphene (Bae et al. 2010) and 10 kΩ per square at 78 % transmittance in the visible, for large-scale liquid exfoliated graphene LBA films (Matković et al. 2016). It is known that optical transmittance of graphite increases upon metallization by intercalation with e.g caesium (Hennig 1965). This unusual property results from the unique band structure of the graphene layer; intercalation heavily dopes ultrathin graphite, shifting the Fermi level upward more than any other band engineering method (Hennig 1965; Khrapach et al. 2012; Wang et al. 2008; Efetov and Kim 2010) suppressing interband optical transitions due to Pauli blocking thus increasing transmittance of light in the visible range. Intercalation of atoms into layered materials is a well known method for providing new properties that are usually distinctly different from those of the pristine materials. Specially interesting is the intercalation of graphene with alkali metals (Wang et al. 2009; Kim et al. 2009; Reina et al. 2009; Buldum and Tetiker 2013; Profeta et al. 2012; Pešić et al. 2015). Graphene doped with Li is well-studied for energy storage applications such are Li-ion batteries and supercapacitators (Wang et al. 2009; Kim et al. 2009; Elias et al. 2009; Kim et al. 2008; Sekitani et al. 2008; Szczniak et al. 2014). Graphene intercalation is even more interesting knowing that doped graphene can be atomic thin superconductor (Profeta et al. 2012; Szczniak et al. 2014; Calandra and Mauri 2005; Pešić et al. 2014; Durajski 2015a; Margine and Giustino 2014; Si et al. 2013). Li doped graphene, since its very recent experimental realization (Ludbrook et al. 2015) has been drawing even more attention, first its theoretical prediction and afterwards its experimental realisation, has inspired search for other new 2D superconductors and their behaviour (Eom et al. 2006; Durajski 2015b; Penev et al. 2016). With all above considered, graphene doped with Li is interesting for many applications, from energy storage to optoelectronic and detail description of its optical properties is an important topic. Li doped graphitic materials are studied for optical properties, mostly in form of the ultrathin films(3–60 layers) (Bao et al. 2014), inspired by its recent experimental realization (Ludbrook et al. 2015), and we focus on graphene monolayer doped with Li, in a manner similar to intercalated graphite. Interest for application of other 2D materials in optoelectronics grown with experimental realisation of MoS_2 (Mak et al. 2010). The MoS_2 monolayer is a member of transitional metal dichalcogenides 2D materials family, and it has a hexagonal structure, like graphene, with the monoatomic Mo plane placed between two monoatomic S planes, and it displays some interesting electronic and photocatalytic properties (Sivek et al. 2013; Liu et al. 2010) Unlike the graphene, which does not have a band gap, a property essential for many optical applications, MoS_2 is direct-gap semiconductor (Mak et al. 2010) which opens possibilities for many optical applications. In this
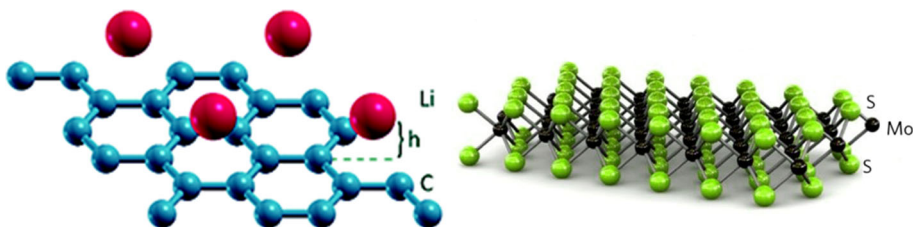

Fig. 1 Model of intercalated graphene and MoS_2

paper we study optical properties of graphene doped with lithium and MoS_2 (as shown in Fig. 1), in particular we discuss the imaginary part of dielectric function, using approaches based on DFT, implemented in the Quantum Espresso software package (Giannozzi 2009). We are interested in the study of the optical properties of this two materials using DFT as a computational inexpensive method for the qualitative description. First, we study MoS_2 and compare it with existing studies in order to approve this technique as sufficient for study and then we investigate graphene doped with Li and compare it with pristine graphene.

2 Computational details

For presented analysis, Quantum Espresso code (Giannozzi 2009), based on DFT, was used. The approach is based on an iterative solution of the Kohn–Sham equations of the DFT in a plane-wave basis set. The unit cell for Li-intercalated graphene was modeled in the $\sqrt{3} \times \sqrt{3}$ R60° in-plane unit cell, and consists of one adatom atom placed above the center of the carbon hexagon. The ionic positions in the cell are fully relaxed, in all calculations, to their minimum energy configuration using the Broyden–Fletcher–Gold-farb–Shanno (BFGS) algorithm. The hexagonal cell parameter c was set to c = 12.5 Å in order to simulate a two-dimensional system and to avoid an interaction due to periodicity. According to the DFT study (Ji et al. 2013) the favorable adsorption site, for the Li adatom on surface of the graphene, is above the center of the graphene hexagon called H-site. The norm-conserving pseudopotential (Perdew and Zunger 1981) and the plane wave kinetic energy cutoff of 65 Ry were used in the calculation of Li-intercalated graphene. The uniform k-point grid was composed of 4096 points in the first Brillouin zone. For MoS_2, GGA exchange-correlation functional, Perdew–Burke–Ernzerhof (PBE) (Krack 2005) was used for relaxation of the system. Also, similar as in graphene, to avoid periodicity effects, 20 Å vacuum between layers was added. The plane wave kinetic energy cutoff of 50 Ry was used and the uniform k-point grid was composed of 4096 points in the first Brillouin zone. Dielectric function $\epsilon(\omega)$ was calculated, in range 1–20 eV, within the framework of the random-phase approximation (RPA) (Brener 1975) based on DFT ground-state cal-culations, starting from eigenvectors and eigenvalues, implemented in Quantum Espresso code as epsilon.x post-processing utility. Matrix elements were accounted only for inter-band transitions that can cause an inaccuracy $\epsilon(\omega)$. RPA does not include the nonlocal part of the pseudo-potential and it is not able to include in the calculation the non-local field effects and excitonic effects. We are interested in the study of the optical properties of this two materials using DFT as a computational inexpensive method for the qualitative description. For more precise and detailed approach many-body theory and its methods are required (Bethe–Salthpeter equation (BSE) and GW approximtion).

3 Results

The imaginary part of the dielectric function of the MoS_2, pristine and Li-intercalated graphene is calculated (because it can be used to obtain the absorption spectra). The optical properties have been calculated in the energy range from 1 to 20 eV.

We calculate the dielectric function for the MoS_2 monolayer. The imaginary part of the dielectric function of MoS_2 for the **E** vector perpendicular to the c axis is presented in the

green color and **E** parallel to the c axis is presented in the violet on the Fig. 2. Four distinct structures on the Fig. 2, at 1 (2.7 eV), 2 (3.7 eV), 3 (4.2 eV) and 4 (5.3 eV) can be connected to the interband transitions, marked on the inset of the electronic band structure, with 1, 2, 3 and 4 as well. All the interband transition depicted here are mainly due to the transition from the p valence bands of S to the d conduction bands of the Mo (Kumar and Ahluwalia 2012). The peak 1 is determined by the interband transitions from the valence bands I, II below the Fermi energy to the conduction bands I, II and III above the Fermi energy along ΓM and $K\Gamma$ direction. The peak 2 is due the interband transitions from the valence bands II below the Fermi energy to the conduction bands II and III above the Fermi energy along ΓM direction and near the M. The peak 3 exists due to the interband transitions from the valence bands III below the Fermi energy to the conduction bands II and III above the Fermi energy along $K\Gamma$ direction. Peak 4 is determined by the interband transitions from the valence bands IV below the Fermi energy to the conduction band I above the Fermi energy in the vicinity of the M high symmetry point. Our calculations are in agreement with the other similar DFT studies (Kumar and Ahluwalia 2012) and experimental research as well (Li et al. 2014) but for the more precise results an advance approach is needed (BSE). By concluding this, we proceed to imaginary part of the dielectric function of the prisitine and intercalated graphene. Results are presented on the Fig. 3. For the pristine graphene, there is a significant peak at small frequencies at 4 eV and another peak at 14 eV. The origin of these peak structures is $\pi \rightarrow \pi^*$ and $\sigma \rightarrow \sigma^*$ interband transition (Marinopoulos et al. 2004), respectively. Ellipsometry measurements show first peak is at 4.6 eV (Matković et al. 2012; Isić et al. 2011; Kostić et al. 2009) and it is connected with the van Hove singularity in graphenes density of states (the M point). The lower value compared to one derived from the experiment, could be due to neglecting of the interaction between graphene film and substrat and many-body interactions within the RPA calculation (Trevisanutto et al. 2010; Sedelnikova et al. 2011). There is also present singularity at zero frequency in (due to metallic property of studied system). Intercalation did not introduce the band gap so peaks are not shifted as it can be seen on the Fig. 3. The intensity of peaks obtained in this study cannot be discussed in proper way due to approximative nature of the used method. The variation in peak heights for the same material, can be observed in calculations based on various models (Bulusheva et al. 2016). We can discuss qualitatively, for peak at 4 eV, it is expected that, analogues to bulk graphite and bulk LiC_6, due to the up-shift of the Fermi level, part of the π^*-like final bands in graphite fall below the Fermi level in LiC_6 and lead to a reduction of the peak
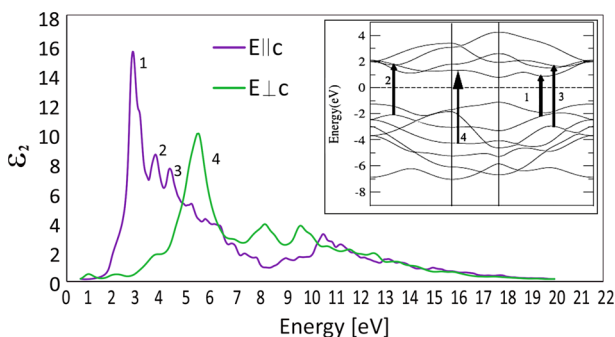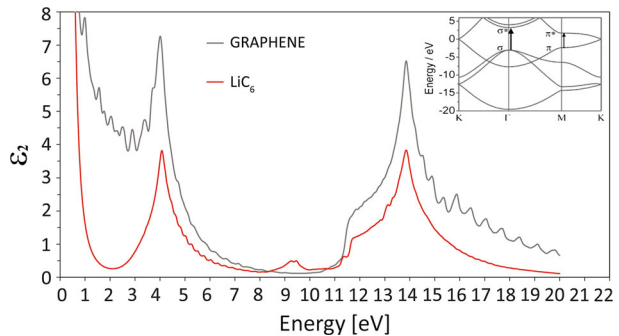

Fig. 2 The calculated imaginary part of the dielectric function for MoS_2

Fig. 3 The calculated imaginary part of the dielectric function for the pristine and intercalated graphene for the E vector perpendicular to the c axis

height (Chen and Rabii 1985). Similar is expected to happen in graphene and LiC_6-monolayer. Similar effect is discussed in graphene monolayer doped with various amounts of B and N (Rani et al. 2014). Continuing analogy with LiC_6 bulk, for other peak a 14 eV, this structure also corresponds to transitions at graphite, however, due to zone folding, they correspond to contributions from different regions in the LiC_6 Brillouin zone (Chen and Rabii 1985; Eklund et al. 1986).

4 Conclusion

In this paper we have studied the optical properties i.e. the dielectric function of the MoS_2 as a monolayer transitional metal dichalcogenidemonolayer and the Li-intercalated graphene, as representative material for the alkali intercalated graphene and important material for energy and optoelectronic applications, using DFT techniques. We can conclude that the Li intercalation in monolayer graphene does not significantly affects the imaginary part of the dielectric function and hence the absorption spectra. Because of the similarity in there properties, in Li doped and pristine graphene, we can expect that they can be used in similar optic application. Experimental data for comparison are not yet available for LiC_6 but parallels with graphene and bulk LiC_6 can be drawn and discusses. Although used technique qualitatively well describes MoS_2 and LiC_6, effects present in those materials due to the exitonic effects and interband transitions, demand detail and advanced approach (but computationally significantly more expensive, time-demanding and resource-consuming). In technical aspect we can conclude that DFT techniques can be used for study of the optical properties of these and similar 2D materials, and they provide the reliable and computationally non-expensive solution (even available for calculating on personal computer) for the satisfactory qualitative description.

References

Bae, S., Kim, H., Lee, Y., Xu, X., Park, J.-S., Zheng, Y., Balakrishnan, J., Lei, T., Kim, H.R., Il Song, Y., Kim, Y.-J., Kim, K.S., zyilmaz, B., Ahn, J.-H., Hong, B.H., Iijima, S.: Roll-to-roll production of 30-inch graphene films for transparent electrodes. Nat. Nanotechnol. **5**, 574–578 (2010)

Bao, W., Wan, J., Han, X., Cai, Xi, Zhu, H., Kim, D., Ma, D., Xu, Y., Munday, J.N., Drew, H.D., Fuhrer, M. S., Hu, L.: Approaching the limits of transparency and conductivity in graphitic materials through lithium intercalation. Nat. Commun. **5**, 4224 (2014)

Brener, N.E.: Random-phase-approximation dielectric function for diamond, with local field effects included. Phys. Rev. B **12**, 1487–1492 (1975)

Buldum, A., Tetiker, G.: First-principles study of graphene-lithium structures for battery applications. J. Appl. Phys. **113**, 154312 (2013)

Bulusheva, L.G., Sedelnikova, O.V., Okotrub, A.V.: Many-body effects in optical response of graphene-based structures. Int. J. Quantum Chem. **116**, 270–281 (2016)

Calandra, M., Mauri, F.: Theoretical explanation of superconductivity in C_6Ca. Phys. Rev. Lett. **95**, 237002 (2005)

Chen, N.-X., Rabii, S.: Theoretical investigation of the optical spectra of LiC_6. Phys. Rev. B **31**, 4784–4791 (1985)

Durajski, A.P.: Influence of hole doping on the superconducting state in graphane. Supercond. Sci. Technol. **28**, 035002 (2015a)

Durajski, A.P.: Effect of layer thickness on the superconducting properties in ultrathin Pb films. Supercond. Sci. Technol. **28**, 095011 (2015b)

Efetov, D.K., Kim, P.: Controlling electron-phonon interactions in graphene at ultrahigh carrier densities. Phys. Rev. Lett. **105**, 256805–256809 (2010)

Eklund, P.C., Yang, M.H., Doll, G.L., Dresselhaus, M.S.: Optical Properties of Donor-Type Graphite Intercalation Compounds-Intercalation in Layered Materials, pp. 257–270. Springer, Boston (1986)

Elias, D.C., Nair, R., Mohiuddin, T.M., Morozov, S.V., Blake, P., Halsall, M.P., Ferrari, A.C., Boukhvalov, D.W., Katsnelson, M.I., Geim, A.K., Novoselov, K.S.: Control of graphene's properties by reversible hydrogenation: evidence for graphane. Science **323**, 610–613 (2009)

Eom, D., Qin, S., Chou, M.-Y., Shih, C.K.: Persistent superconductivity in ultrathin Pb films: a scanning tunneling spectroscopy study. Phys. Rev. Lett. **96**, 027005 (2006)

Giannozzi, P., et al.: QUANTUM ESPRESSO: a modular and open-source software project for quantum simulations of materials. J. Phys. Condens. Matter **21**, 395502 (2009)

Hennig, G.R.: Optical transmission of graphite compounds. J. Chem. Phys. **43**, 1201–1206 (1965)

Isić, G., Jakovljevi, M., Filipović, M., Jovanović, Dj, Vasić, B., Lazović, S., Puač, Nevena, Lj Petrović, Z., Kostić, R., Gajić, R., Humlček, J., Losurdo, M., Bruno, G., Bergmair, I., Hingerl, K.: Spectroscopic ellipsometry of few-layer graphene. J. Nanophoton. **5**, 051809 (2011)

Ji, Z., Contreras-Torres, F.F., Jalbout, A.F., Ramrez-Trevio, A.: Methods, surface diffusion and coverage effect of Li atom on graphene as studied by several density functional theory. Appl. Surf. Sci. **285**, 846–852 (2013)

Katsnelson, M.I., Novoselov, K.S., Geim, A.K.: Chiral tunnelling and the Klein paradox in graphene. Nat. Phys. **2**, 620–625 (2006)

Khrapach, I., Withers, F., Bointon, T.H., Polyushkin, D.K., Barnes, W.L., Russo, S., Craciun, M.F.: Novel highly conductive and transparent graphene-based conductors. Adv. Mat. **24**, 2844–2849 (2012)

Kim, D.-H., Ahn, J.-H., Choi, W.M., Kim, H.-S., Kim, T.-H., Song, J., Huang, Y.Y., Liu, Z., Lu, C., Rogers, J.A.: Stretchable and foldable silicon integrated circuits. Science **320**, 507–511 (2008)

Kim, K.S., Zhao, Y., Jang, H., Lee, S.Y., Kim, J.M., Kim, K.S., Ahn, J.-H., Kim, P., Choi, J.-Y., Hong, B.H.: Large-scale pattern growth of graphene films for stretchable transparent electrodes. Nature **457**, 706–710 (2009)

Kostić, R., Mirić, M., Radić, T., Radović, M., Gajić, R., Popović, Z.V.: Optical characterization of graphene and highly oriented pyrolytic graphite. Acta Phys. Pol. A **116**, 718–721 (2009)

Kotov, V.N., Uchoa, B., Pereira, V.M., Guinea, F., Castro Neto, A.H.: Electron–electron interactions in graphene: current status and perspectives. Rev. Mod. Phys. **84**, 1067–1125 (2012)

Krack, M.: Pseudopotentials for H to Kr optimized for gradient-corrected exchange-correlation functionals. Theor. Chem. Acc. **114**, 145–152 (2005)

Kumar, A., Ahluwalia, P.K.: A first principle comparative study of electronic and optical properties of 1H–MoS2 and 2H–MoS2. Mater. Chem. Phys. **135**, 755–761 (2012)

Li, W., Birdwell, A.G., Amani, M., Burke, R.A., Ling, X., Lee, Y.-H., Liang, X., Peng, L., Richter, C.A., Kong, J., Gundlach, D.J., Nguyen, N.V.: Broadband optical properties of large-area monolayer CVD molybdenum disulfide. Phys. Rev. B **90**, 195434 (2014)

Liu, Y., Ren, L., He, Y., Cheng, H.P.: Titanium-decorated graphene for high-capacity hydrogen storage studied by density functional simulations. J. Phys. Condens. Matter **22**, 445301 (2010)

Ludbrook, B.M., Levy, G., Nigge, P., Zonno, M., Schneider, M., Dvorak, D.J., Veenstra, C.N., Zhdanovich, S., Wong, D., Dosanjh, P., Straer, C., Sthr, A., Forti, S., Ast, C.R., Starke, U., Damascelli, A.: Evidence for superconductivity in Li-decorated monolayer graphene. PNAS **112**, 11795–11799 (2015)

Mak, K.F., Lee, C., Hone, J., Shan, J., Heinz, T.F.: Atomically thin MoS: a new direct-gap semiconductor. Phys. Rev. Lett. **105**, 136805 (2010)

Margine, E.R., Giustino, F.: Two-gap superconductivity in heavily n-doped graphene: Ab initio Migdal–Eliashberg theory. Phys. Rev. B **90**, 014518 (2014)

Marinopoulos, A.G., Reining, L., Rubio, A., Olevano, V.: Ab initio study of the optical absorption and wave-vector-dependent dielectric response of graphite. Phys. Rev. B **69**, 245419 (2004)

Matković, A., Beltaos, A., Milićević, M., Ralević, U., Vasić, B., Jovanović, Dj, Gajić, R.: Spectroscopic imaging ellipsometry and Fano resonance modeling of graphene. J. Appl. Phys. **112**, 123523 (2012)

Matković, A., Milošević, I., Milićević, M., Tomašević-Ilić, T., Pešić, J., Musić, M., Spasenović, M., Jovanović, D., Vasić, B., Deeks, C., Panajotović, R., Belić, M., Gajić, R.: Enhanced sheet conductivity of Langmuir–Blodgett assembled graphene thin films by chemical doping. 2D Mater **3**, 015002 (2016)

Novoselov, K.S., Geim, A.K., Morozov, S.V., Jiang, D., Zhang, Y., Dubonos, S.V., Grigorieva, I.V., Firsov, A.A.: Electric field effect in atomically thin carbon films. Science **306**, 666–669 (2004)

Novoselov, K.S., Jiang, Z., Zhang, Y., Morozov, S.V., Stormer, H.L., Zeitler, U., Maan, J.C., Boebinger, G. S., Kim, P., Geim, A.K.: Room-temperature quantum hall effect in graphene. Science **315**, 1379 (2007)

Penev, E.S., Kutana, A., Yakobson, B.I.: Can two-dimensional boron superconduct? Nano Lett. **16**, 2522–2526 (2016)

Perdew, J.P., Zunger, Alex: Self-interaction correction to density-functional approximations for many-electron systems. Phys. Rev. B **23**, 5048–5080 (1981)

Pešić, J., Gajić, R., Hingerl, K., Belić, M.: Strain-enhanced superconductivity in Li-doped graphene. EPL **108**, 67005 (2014)

Pešić, J., Damljanović, V., Gajić, R., Hingerl, K., Belić, M.: Density functional theory study of phonons in graphene doped with Li, Ca and Ba. EPL **112**, 67006 (2015)

Profeta, G., Calandra, M., Mauri, F.: Phonon-mediated superconductivity in graphene by lithium deposition. Nat. Phys. **8**, 131–134 (2012)

Rani, P., Dubey, G.S., Jindal, V.K.: DFT study of optical properties of pure and doped graphene. Phys. E **62**, 28–35 (2014)

Reina, A., Jia, X., Ho, J., Nezich, D., Son, H., Bulovic, V., Dresselhaus, M.S., Kong, J.: Large area, few-layer graphene films on arbitrary substrates by chemical vapor deposition. Nano Lett. **9**, 30–35 (2009)

Sedelnikova, O.V., Bulusheva, L.G., Okotrub, A.V.: Ab initio study of dielectric response of rippled graphene. J. Chem. Phys. **134**, 244707 (2011)

Sekitani, T., Noguchi, Y., Hata, K., Fukushima, T., Aida, T., Someya, T.: A rubberlike stretchable active matrix using elastic conductors. Science **321**, 1468–1472 (2008)

Si, C., Liu, Z., Duan, W., Liu, F.: First-principles calculations on the effect of doping and biaxial tensile strain on electron–phonon coupling in graphene. Phys. Rev. Lett. **111**, 196802 (2013)

Sivek, J., Leenaerts, O., Partoens, B., Petters, F.M., Adsorption of Titanium and Titanium Dioxide on Graphene: n and p-type Doping. arXiv:1301.3654 [cond-mat.mtrl-sci] (2013)

Szczniak, D., Durajski, A.P., Szczniak, R.: Influence of lithium doping on the thermodynamic properties of graphene based superconductors. J. Phys. Condens. Matter **26**, 255701 (2014)

Trevisanutto, P.E., Holzmann, M., Ct, M., Olevano, V.: Ab initio high-energy excitonic effects in graphite and graphene. Phys. Rev. B **81**, 121405 (2010)

Wang, F., Zhang, Y., Tian, C., Girit, C., Zettl, A., Crommie, M., Shen, Y.R.: Gate-variable optical transitions in graphene. Science **320**, 206–209 (2008)

Wang, X., Li, X., Zhang, L., Yoon, Y., Weber, P.K., Wang, H., Guo, J., Dai, H.: N-doping of graphene through electrothermal reactions with ammonia. Science **324**, 768–771 (2009)

Zhang, Y., Tan, Y.W., Stormer, H.L., Kim, P.: Experimental observation of the quantum Hall effect and Berry's phase in graphene. Nature **438**, 201–204 (2005)

Advantages of GPU technology in DFT calculations of intercalated graphene

J Pešić and R Gajić

Center for Solid State Physics and New Materials, Institute of Physics, University of Belgrade, Pregrevica 118, 11080 Belgrade, Serbia

E-mail: yelena@ipb.ac.rs

Abstract

Over the past few years, the expansion of general-purpose graphic-processing unit (GPGPU) technology has had a great impact on computational science. GPGPU is the utilization of a graphics-processing unit (GPU) to perform calculations in applications usually handled by the central processing unit (CPU). Use of GPGPUs as a way to increase computational power in the material sciences has significantly decreased computational costs in already highly demanding calculations. A level of the acceleration and parallelization depends on the problem itself. Some problems can benefit from GPU acceleration and parallelization, such as the finite-difference time-domain algorithm (FTDT) and density-functional theory (DFT), while others cannot take advantage of these modern technologies. A number of GPU-supported applications had emerged in the past several years (www.nvidia.com/object/gpu-applications.html). Quantum Espresso (QE) is reported as an integrated suite of open source computer codes for electronic-structure calculations and materials modeling at the nano-scale. It is based on DFT, the use of a plane-waves basis and a pseudopotential approach. Since the QE 5.0 version, it has been implemented as a plug-in component for standard QE packages that allows exploiting the capabilities of Nvidia GPU graphic cards (www.qe-forge.org/gf/proj). In this study, we have examined the impact of the usage of GPU acceleration and parallelization on the numerical performance of DFT calculations. Graphene has been attracting attention worldwide and has already shown some remarkable properties. We have studied an intercalated graphene, using the QE package PHonon, which employs GPU. The term 'intercalation' refers to a process whereby foreign adatoms are inserted onto a graphene lattice. In addition, by intercalating different atoms between graphene layers, it is possible to tune their physical properties. Our experiments have shown there are benefits from using GPUs, and we reached an acceleration of several times compared to standard CPU calculations.

Keywords: GPU, DFT, graphene, intercalation, first principle

(Some figures may appear in colour only in the online journal)

Introduction

A development of general-purpose graphic-processing unit (GPGPU) technology has had great impact on computational science, and it is shown to be a valuable resource when it comes to the high-resource-demanding calculations of solid-state physics. GPGPUs use a graphic-processing unit to perform calculations usually handled by the central-processing unit (CPU).

We used Quantum Espresso code and examined the impact of GPU acceleration and parallelization on the density functional theory (DFT) calculations of graphene.

Calculation method

Although GPUs have been an essential part of any computer for decades, it became much more important during the last

decade of twentieth century. The era of three-dimensional (3D) graphics in the gaming industry started in the mid-1990s, but for scientific use, GPUs showed their true potential in the first years of 2000s when GPU programmability was introduced.

High-performance computing (HPC) became widely available thanks to GPU computing and the fact that it brought the performance of the most powerful super-computers of ten years ago to today's affordable workstations [1]. GPUs nowadays are an important platform for general-purpose computing.

A GPU is a massively parallel processor with a large memory bandwidth. Its memory is hierarchically organized, and the transitions between various memory levels are explicitly defined and organized by the programmer.

One or several GPUs can be easily included in a common workstation and supercomputer nodes as well. Hybrid combinations of one or more GPUs with aCPU are one of the main choices of HPC laboratories worldwide because of their indisputable combination of high performance and low price.

GPUs are valuable tools for calculations and numerical simulations, but it is very important to emphasize that not all problems can benefit equally from using a GPU. Certain problems are native for parallelization and GPU acceleration. However, the DFT calculation method is shown to have great success in exploiting the advances of GPU technology.

DFT is a method for *ab-initio* electronic structure calculations based on Kohn-Sham equations. For solving Kohn-Sham equations, there are several numerical approaches and approximations, each based on discretization of equations and the treatment of core electrons [2]. An iterative procedure, known as the self-consistent field (SCF) method, is used to find solutions to eigenproblems.

Quite a few codes and programs have been developed for DFT calculations. In the past few years, certain codes have been reported to support GPU technology. The main idea behind porting existing DFT code to GPUs is to discover methods for improving the computationally expensive parts of the SCF loop and re-implementing them with GPUs [2]. This is achieved by replacing common computational libraries with GPU versions, such as compute unified basic linear algebra subroutines (CUBLAS), compute unified fast Fourier transform (CUFFT), among others, and by writing custom kernels for GPUs. The final goal is performance speedup by more than several timeswhileminimizing the poor transfer time of data between a CPU and a GPU, which is one of the biggest bottlenecks.

Quantum Espresso (QE) is an integrated suite of open-source computer codes for electronic-structure calculations and materials modeling at the nano-scale [3] and is based on DFT, the use of a plane-waves basis and a pseudopotential approach. Since version 5.0, certain packages of QE have been able to exploit the capabilities of Nvidia GPUs by porting the most computationally expensive parts of the SCF cycle to run on GPUs. QE uses CUFFT and the Magma computational software, as well as phiGEMM numerical library operations, which are parallel hybrid replacements for GEMM [4]. It has been shown that the best practice is to
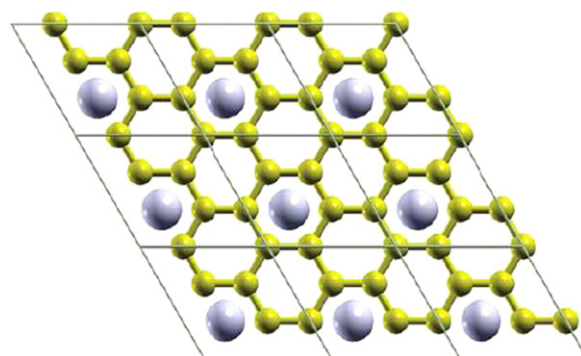

Figure 1. Crystal structure of monolayer graphene with lithium adatoms. Small yellow spheres represent carbon atoms, whereas larger violet spheres represent lithium adatoms placed in the hollow sites of the graphene layer at H-sight.

Table 1. Optimized structural parameters, lattice constant (a) and adatom-graphene distance (h) in Å.

	a	h
LiC_6	4.27	1.73

employ OpenMP parallelizations within one node, MPI parallelizations across multiple nodes, and GPU acceleration where possible for the studied problem.

Graphene

Graphene has been attracting attention worldwide and has shown some remarkable properties [5]. Our goal is to show the advantages of applying GPU technology to DFT calculations for graphene. We chose the QE package PHonon, which employs GPU technology. It implements density-functional perturbation theory (DFPT) to calculate second- and third-order derivatives of energies with respect to atomic displacement and electric fields [6].

In this study, we examined intercalated graphene. The term 'intercalation' refers to a process where foreign adatoms are inserted onto a graphene lattice. Studies have shown it is possible to tune properties of the graphene by doping the surface with alkaline metal adatoms [6]. This is analogous to graphite-intercalated compounds (GIC).

Results

Methods

The reported results were obtained from first-principles DFT in a local density approximation (LDA). We used QE with a norm-conserving pseudopotential and the plane-wave cutoff energy of 65Ry. A monolayer system was simulated in $\sqrt{3} \ x \ \sqrt{3} R30°$ in-plane unit cell with one lithium adatom per unit cell and 6 Å of vacuum between layers (to simulate a monolayer) (figure 1).
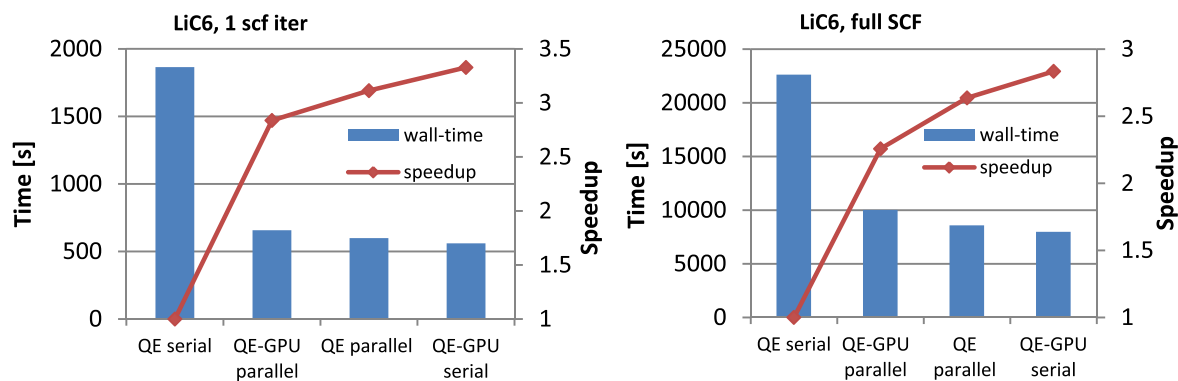
Figure 2. QE-PWscf calculation on Intel Core i7-3930K at 3.8 GHz with Nvidia Tesla K20 (a) single SCF iteration and (b) full SCF calculation.

All structures were relaxed to their minimum energy configuration (in respect to the stress tensor of the unit cell and the internal forces on atoms) (table 1).

GPU acceleration

All QE PH calculations consist of several parts:

1. SCF calculations on a dense grid that consists of all k and k + q grid points.
2. and 3. Normal SCF and phonon dispersion calculations on the coarse k-point grid.

To show differences in calculation wall-times, the same input was used for four different system configurations.

- QE in serial configuration
- QE in parallel configuration
- QE in serial configuration + GPU
- QE in parallel configuration + GPU

Computational resources

We present data obtained using a heterogeneous system equipped with a GPU. All calculations have been executed on the workstation at the GPU Group for Simulations in Solid State Physics at the Center for Solid State Physics and New Materials at the Institute of Physics, with Intel Core i7-3930K at 3.8 GHz with 32 GB RAM. Calculations were performed employing OpenMPI parallelization on a four-core system, with two parallel processes and MKL multi-threading, using four MKL threads.

The GPU-accelerated calculations have been executed on the Nvidia's Tesla K20, which consists of 2496 compute unified device architecture (CUDA) cores[1].

We compared wall-times for QE-PWscf.

[1] www.nvidia.com/object/nvidia-kepler.html.

Table 2. Wall time and speedup for the QE-SCF calculation on a dense grid for the monolayer graphene with Li adatoms for four different system configurations.

Configuration	Wall time 1 SCF iter [s]	Speedup 1 iter	Wall-time full SCF [s]	Speed up full SCF
QE serial	1864.7	1	22 620	1
QE-GPU parallel	657.1	2.84	10 020	2.26
QE parallel	598.8	3.11	8580	2.64
QE-GPU serial	560.3	3.33	7980	2.83

Conclusion and further study

We have shown that using GPU technologies together with CPU processing can decrease the calculation duration for graphene with adatoms by up to three times (figure 2).

An important fact is that the level of acceleration that can be reached depends significantly on the problem itself. As shown in table 2, for this kind of calculation with the workstation used, the best wall-times are achieved for QE serial with GPU. It is important to emphasize that the problem used in this calculation is rather small, and on larger systems the GPU acceleration would be even more visible [1]. GPUs were designed in a highly parallel structure that allows large sets of data to be processed at the same time; similar computations are being made on data at the same time. This is the reason additional GPU acceleration makes calculation more efficient. CPUs are made to handle requests more linearly, even in parallel mode. For our problem, CPU parallelization also shows good results, but with a larger observed system, the benefit from parallel computation would be also more obvious (we could create more processes for the processor unit).

Here we have an example where improvement in the communication speed and bandwidth between CPU and GPU would be highly beneficial. If the test problem were more complex, the parts of the problem calculated on the GPU would also be more complex, and the speedup achieved

would compensate for insufficient CPU–GPU communication speed and bandwidth. In our problem, we have substantial CPU processes and GPU communication for a rather short calculation during the steps in between.

In addition, to improve the speed for this resource-demanding calculation, in further studies the focus should be on exploring better ways to distribute GPU resources on parallel processes whileovercoming these components' poor communication speeds.

Acknowledgements

References

[1] Girotto I, Varini N, Spiga F, Cavazzoni C, Ceresoli D, Martin-Samos L and Gorni T 2012 Enabling of Quantum-ESPRESSO to petascale scientific challenges *PRACE Whitepapers.* (www.prace-ri.eu/IMG/pdf/ enabling_of_quantum_espresso_to_petascale_scientific_ challenges.pdf)
[2] Harju A, Siro T, Federici-Canova F, Hakala S and Rantalaiho T 2013 Computational physics on graphics processing units *Applied Parallel and Scientific Computing* vol 7782 (Berlin: Springer) pp 3–26
[3] Giannozzi P *et al* 2009 *J. Phys.:Condens. Matter* **21** 395502
[4] Spiga F and Girotto I 2012 phiGEMM: a CPU-GPU library for porting Quantum ESPRESSO on hybrid systems *Proc. 20th Euromicro Int. Conf. on Parallel, Distributed and Network Based Computing –Special Session on GPU Computing and Hybrid Computing* pp 368–75
[5] Novoselov K S, Falko V I, Colombo L, Gellert P R, Schwab M G and Kim K 2012 *Nature* **490** 192
[6] Profeta G, Calandra M and Mauri F 2012 *Nat. Phys.* **8** 131–4

2D Materials

PAPER

Enhanced sheet conductivity of Langmuir–Blodgett assembled graphene thin films by chemical doping

Aleksandar Matković[1], Ivana Milošević[1], Marijana Milićević[1], Tijana Tomašević-Ilić[1], Jelena Pešić[1], Milenko Musić[1], Marko Spasenović[1], Djordje Jovanović[1], Borislav Vasić[1], Christopher Deeks[2], Radmila Panajotović[1], Milivoj R Belić[3] and Radoš Gajić[1]

1   Center for Solid State Physics and New Materials, Institute of Physics, University of Belgrade, Pregrevica 118, 11080 Belgrade, Serbia
2   Thermo Fisher Scientific, Unit 24, The Birches Industrial Estate, East Grinstead, RH19 1UB, UK
3   Texas A & M University at Qatar, PO Box 23874 Doha, Qatar

E-mail: amatkovic@ipb.ac.rs

Abstract

We demonstrate a facile fabrication technique for highly conductive and transparent thin graphene films. Sheet conductivity of Langmuir–Blodgett assembled multi-layer graphene films is enhanced through doping with nitric acid, leading to a fivefold improvement while retaining the same transparency as un-doped films. Sheet resistivity of such chemically improved films reaches 10 k$\Omega/\square$, with optical transmittance 78% in the visible. When the films are encapsulated, the enhanced sheet conductivity effect is stable in time. In addition, stacking of multiple layers, as well as the dependence of the sheet resistivity upon axial strain have been investigated.

1 Introduction

Graphene has a multitude of potential applications from high-speed electronics, to energy storage and conversion, to use as transparent conductor [1–3]. As graphene technology matures, applications are moving from the lab to the market, and the performance-to-cost ratio is becoming a crucial parameter in technology adoption, raising the importance of scalable and cost effective routes for production of graphene and related materials [4–7].

Transparent conductive electrodes (TCEs) [8] are an exemplary technology for which graphene offers key advantages compared to established standards. The unique properties that graphene TCEs offer are flexibility [9], thermal and chemical stability [10, 11], functionalization [12] and ease of integration with organic semiconductors [13–15]. Therefore, the use of graphene has already been demonstrated in photovoltaic solar cells [11, 16–18], liquid crystal displays [10], touch-screen panels [19], organic light emitting diodes [20, 21] and many others.

Most of these applications currently rely on graphene obtained through chemical vapor deposition (CVD) [22–24]. Although the CVD process produces some of the highest quality graphene films [25], there are several drawbacks of this technique. CVD of graphene requires high growth temperatures, a vacuum environment and transfer from the metallic substrate, during which the costly metal is usually sacrificed [26]. Nonetheless, multiple layers of CVD graphene grown on copper, transferred, stacked [27] and chemically doped [19, 28] have managed to surpass the industry standard [8] for TCEs set by indium–tin–oxide.

A low-cost alternative to CVD is solution-processed synthesis of graphene and related materials, the first experiments of which yielded graphene oxide [29–31]. Solution-processed sheets of reduced graphene oxide are functionalized with hydroxyls and epoxides and cannot be fully reduced to graphene, which limits film conductance. This issue can be overcome by using a non-covalent liquid phase exfoliation (LPE) of graphite in organic solvents with matching surface energy. LPE was first demonstrated for graphene [10, 32, 33], and then adopted for other two-dimensional materials such as boron-nitride, MoS_2, WS_2, WSe_2 and other [7, 34–36]. LPE of graphite results in a dispersion of graphene and multi-layer graphene sheets (GSs) in the solvent. There are many ways
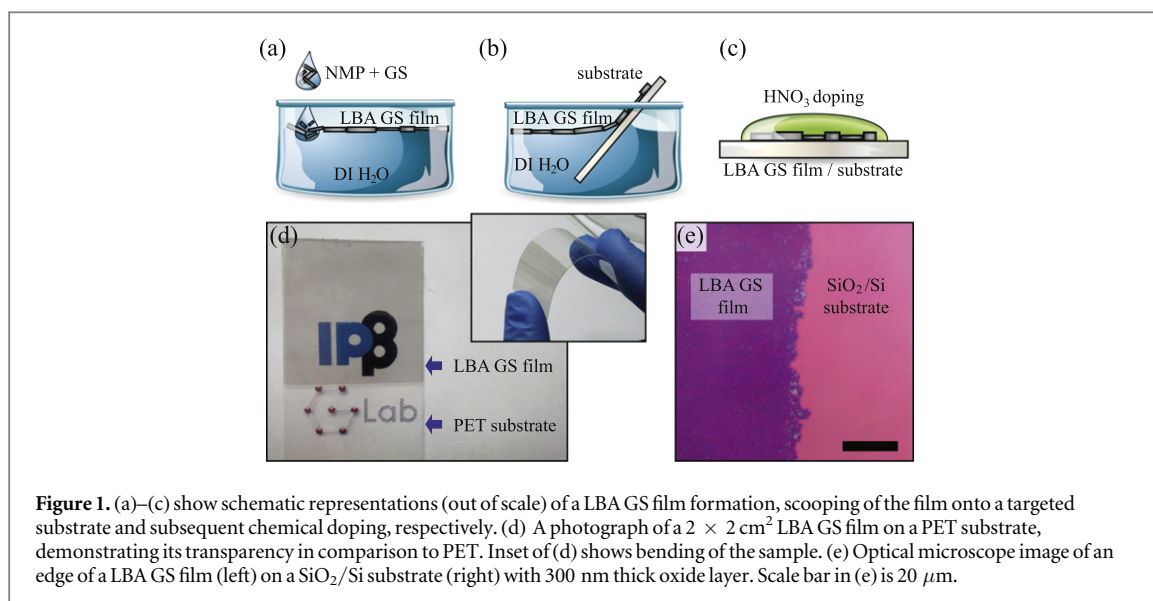
Figure 1. (a)–(c) show schematic representations (out of scale) of a LBA GS film formation, scooping of the film onto a targeted substrate and subsequent chemical doping, respectively. (d) A photograph of a $2 \times 2\,cm^2$ LBA GS film on a PET substrate, demonstrating its transparency in comparison to PET. Inset of (d) shows bending of the sample. (e) Optical microscope image of an edge of a LBA GS film (left) on a SiO_2/Si substrate (right) with 300 nm thick oxide layer. Scale bar in (e) is 20 μm.

to deposit these sheets onto a targeted substrate, for example spray coating [10], ink-jet printing [37–39], vacuum filtration [31, 40], Langmuir–Blodgett assembly (LBA) [41–44], or self-assembly on a liquid–liquid interface [45–47]. Still, the electronic conductance of LPE films is inferior to that of CVD graphene, and any improvement is a step towards industrial applications of solution processed graphene.

We make transparent conductive films of multilayer GSs on flexible polyethylene terephthalate (PET) by LBA on a water–air interface. The sheets adhere strongly to the PET substrate, which allows immersion into other liquids without the risk of the film washing away. We make use of the strong adhesion to chemically dope the graphene in nitric acid for enhanced conductivity, and to stack multiple films on top of each other, opening a gateway to liquid phase assembly of Van der Waals heterostructures [36, 48, 49]. The power of this method is demonstrated by the fivefold reduction in sheet resistivity for a single LBA layer, while maintaining the same optical transparency of the unperturbed films.

We show that LBA GS films can be very effectively p-doped by nitric acid, making them a more suitable low-cost alternative to CVD graphene for various TCE applications. As indicated by the work function measurements and by the measurements of the sheet resistivity under axial strain, chemical doping does not only increase carrier concentration of individual GSs, but also reduces the contact resistance between GSs, which additionally contributes to a larger reduction factor of the sheet resistivity.

2 LBA GS film fabrication and morphological characterization

2.1 Preparation of GS dispersion
As a starting material for the formation of LBA layers, a dispersion of GSs in *N*-methylpyrrolidone (NMP) has

been used. The dispersion fabrication process is based on the earlier established protocol [32]. An initial concentration of graphite powder (Sigma Aldrich-332461) was 18 mg ml^{-1} in NMP (Sigma Aldrich-328634). The solution was sonicated in a low-power ultrasonic bath for 14 h, and centrifuged for one hour at 3000 rpm immediately after sonication. The results of this process are GSs in solution, with a concentration of 0.36 mg ml^{-1}. The concentration was determined via UV–VIS spectrophotometry (SUPER SCAN, Varian) [32]. This particular set of LPE parameters was chosen since the resulting dispersion of GSs in NMP was found to be stable for over six months.

2.2 Langmuir–Blodgett assembly
GSs suspended in NMP were used to fabricate transparent and conductive films by LBA at a water–air interface [43]. Since the LPE process introduces a low degree of oxidation and covalent functionalization, resulting GSs have high hydrophobicity, which is very favorable for the formation of LBA layers [41]. Furthermore, driven by the minimization of interfacial energy, LBA produces a close packed structure of GSs [45]. A schematic representation of LBA GS film formation is presented in figure 1(a). Beakers filled with deionized water (18.2 MΩ) with a water–air interface surface-to-water volume ratio of 0.5 cm^{-1} were used for film formation. A 1.5–2 vol% of GS +NMP was added to the interface with a continuous flow rate of 5–10 μl s^{-1}. A closely packed LBA GS film was found to form on the water–air interface with this set of parameters. Formation of the LBA film was found to be self-limiting, meaning that prior to the film formation on the whole given surface, added GSs are fixed at the interface, and after the complete film was formed, any additional GSs fall through the interface to the bottom of the beaker. Only several microliters of the GS+NMP solution are needed to

fabricate several square centimeters of film. When scaled up, one liter of GS+NMP solution would be sufficient to produce 150×150 m^2 of LBA GS films. Compared to CVD graphene, fabrication cost of these TCEs would be at least three orders of magnitude smaller [4].

2.3 Deposition on a substrate and chemical doping
Interestingly, as proposed by Kim *et al* [43], this process dissolves NMP in the water, effectively removing most of the solvent from the graphene layer. After the film is formed, it is slowly scooped onto the targeted substrate, as schematically presented in figure 1(b). The substrate was either pre-positioned vertically at the edge of the beaker, or was introduced after the LBA film was formed, puncturing the film near the edge of the beaker. Films are then left to dry for several minutes in ambient conditions. After the films were transferred onto the targeted substrates their sheet conductivity was enhanced by chemical doping. This was achieved either by dipping into or covering LBA GS films with a 65% solution of nitric acid in water (see figure 1(c)), followed by quick drying with an air gun.

Our procedure yields quality films on all tested substrates, including SiO$_2$/Si, quartz, glass and PET. We typically pre-fabricated ~50 nm thick gold electrodes on the substrates prior to GS deposition. Figures 1(d) and (e) show LBA GS films on the PET and SiO$_2$/Si substrate, respectively. Films fabricated with this method are uniform over the entire substrate area. Up to several square centimeters of uniform LBA GS films on various substrates were fabricated using this technique, with sheet conductivity and optical transparency not varying more than 5% from the mean value over the entire film.

2.4 Film morphology
The morphology of the obtained LBA GS films was characterized with atomic force microscopy (AFM) and scanning electron microscopy (SEM). AFM measurements were carried out on an atomic force microscope, NTEGRA Spectra, in tapping mode. A typical AFM profile of an LBA GS film on a SiO$_2$/Si substrate is shown in figure 2(a). SiO2/Si was chosen as a substrate for AFM due to its low surface roughness. Figure 2(b) shows a height histogram of a 5×5 μm^2 AFM topography image containing a sharp edge of the LBA GS layer (inset). Ten height histograms of sample/substrate edge areas were used to estimate the thickness of LBA GS films. Each histogram had two clearly resolved peaks corresponding to LBA GS film and the substrate. An average film thickness was estimated as a peak-to-peak distance. While the substrate peak is narrow, due to the low roughness of the SiO$_2$, (left peak in figure 2(b)), the LBA GS film has a much broader height distribution. The sample peak was fitted with a log-normal curve, yielding a mean

film thickness (3.4 ± 0.7) nm. This indicates that LBA GS films have an average thickness of ~10 layers.

The lateral profile of graphene flakes was analyzed with a Tescan MIRA3 field-emission gun SEM. A histogram of flake diameter is presented in figure 2(c). The distribution of flake diameters from six 5×5 μm^2 SEM images (~2000 flakes) was fitted with a log-normal curve, giving an average flake diameter of 120 nm. Both AFM and SEM images were used to estimate a surface coverage of over 90%.

3 Results and discussion
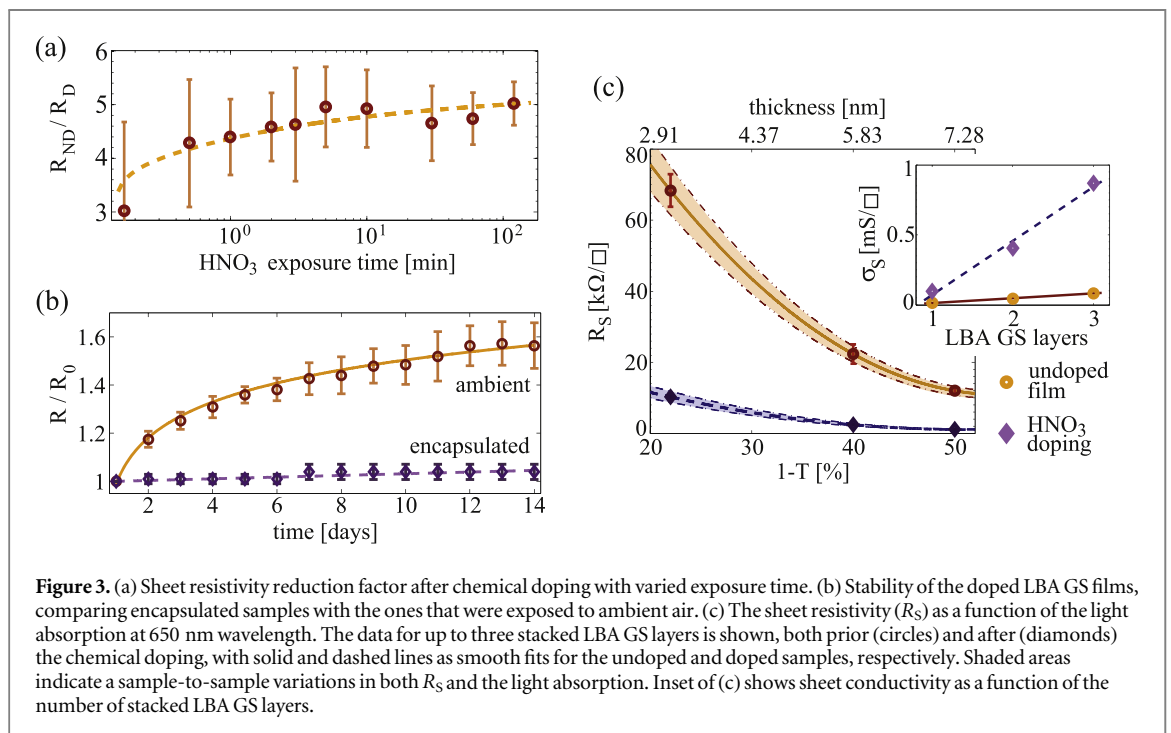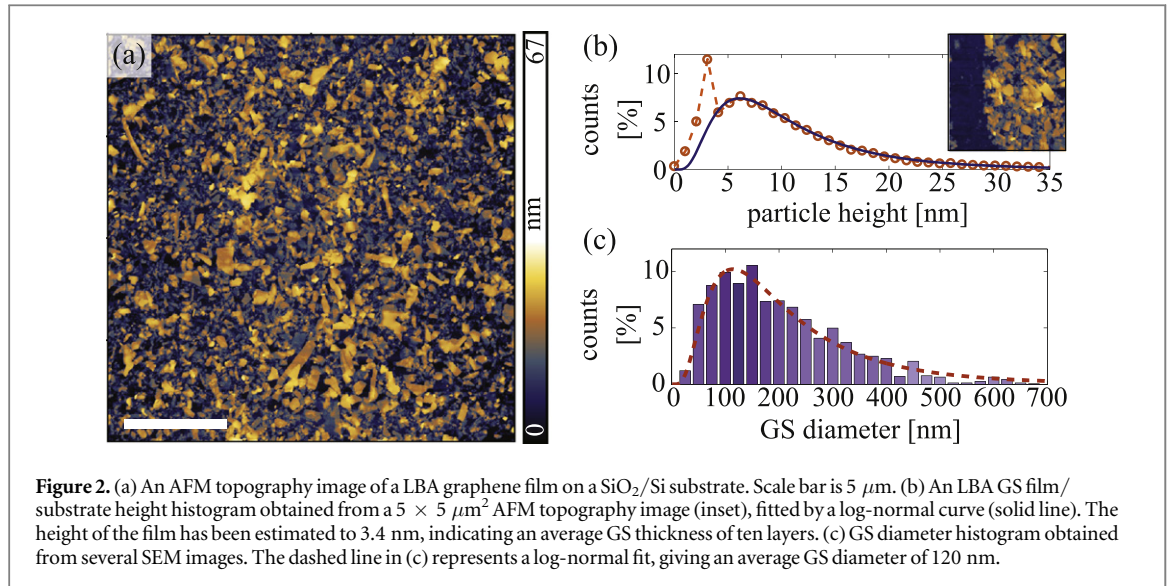
3.1 Nitric acid doping
The key result of this study is doping of LBA GS films with nitric acid for improved sheet conductivity. Chemical doping of graphene can be accomplished with various liquids, vapors and polymers [10, 16, 17, 19, 28, 50–53]. One of the most efficient p-type chemical dopants of graphite and graphene is nitric acid [19, 28, 52, 54, 55]. Nitric acid has been used to chemically dope CVD graphene, and reduce the sheet resistivity by a factor of two to three [17, 19, 28, 50]. It was also used to chemically dope reduced GO [53]. Nitric acid doping of graphene was found to be very favorable for photovoltaic solar cells, where graphene is used as a top anode [16, 17, 50, 56]. Besides a reduction in sheet resistivity, the doping increases graphene's work function from about 4.5 to 5 eV, making these TCEs more suitable anode electrodes for various types of hybrid solar cells [17, 50, 52, 56, 57]. Recently, nitrogen-doped reduced GO and carbon have been demonstrated to show enhancement in energy storage [58, 59]. In the following sections we discuss the results of doping LBA GS films with nitric acid.

3.2 Nitric acid exposure time
In order to determine optimal conditions for chemical doping, the exposure time of a single layer LBA GS layer to nitric acid was varied between 10 s and 2 h. Figure 3(a) shows the exposure time dependent reduction factor of the sheet resistivity, obtained as the ratio of the sheet resistivity prior and after the doping (R_{ND}/R_D). Even after only 30 s of the exposure, the reduction factor greater than four was achieved, and after several minutes the reduction factor was found to saturate at (5 ± 1). In order to ensure the control over chemical doping, the exposure time of 5 min was chosen as an optimal value in this study.

3.3 Time stability of the enhanced conductivity effect
Considering that nitric acid is volatile and that dopants can be desorbed from the sample, the stability of the sheet resistivity was examined over an extended period of time. Two batches of LBA GS films were prepared,

Figure 2. (a) An AFM topography image of a LBA graphene film on a SiO$_2$/Si substrate. Scale bar is 5 μm. (b) An LBA GS film/ substrate height histogram obtained from a 5 × 5 μm^2 AFM topography image (inset), fitted by a log-normal curve (solid line). The height of the film has been estimated to 3.4 nm, indicating an average GS thickness of ten layers. (c) GS diameter histogram obtained from several SEM images. The dashed line in (c) represents a log-normal fit, giving an average GS diameter of 120 nm.

Figure 3. (a) Sheet resistivity reduction factor after chemical doping with varied exposure time. (b) Stability of the doped LBA GS films, comparing encapsulated samples with the ones that were exposed to ambient air. (c) The sheet resistivity (R_S) as a function of the light absorption at 650 nm wavelength. The data for up to three stacked LBA GS layers is shown, both prior (circles) and after (diamonds) the chemical doping, with solid and dashed lines as smooth fits for the undoped and doped samples, respectively. Shaded areas indicate a sample-to-sample variations in both R_S and the light absorption. Inset of (c) shows sheet conductivity as a function of the number of stacked LBA GS layers.

one with the doped LBA GS surface exposed to the ambient conditions, and the other encapsulated (covered with Scotch tape) immediately after chemical doping. Figure 3(b) shows the relative change of sheet resistivity in time as $R(t)/R_0$, where R_0 stands for the initial sheet resistivity. Encapsulated samples show excellent time stability, with less than 5% change in sheet resistivity over two weeks.

3.4 Stacking of multiple LBA GS layers

The excellent adhesion of LBA GS sheets to the PET substrate allows not only for straightforward methods of chemical doping using liquids, but also for reproducible stacking of additional LBA layers. This is a very promising technique for making solution-based GRM

heterointerfaces [36], using a simple, one-step, low-cost and high-yield self-assembly process.

Figure 3(c) shows the sheet resistivity (R_S) as a function of optical transmittance of stacked LBA GS layers. After stacking, samples were exposed to nitric acid for 5 min. The lowest sheet resistivity obtained were on the order of 800 $\Omega/\square$, albeit at only 50% transmittance. The fact that subsequent doping can affect the entire film could be attributed to intercalation of nitric acid into the LBA GS stacks [28].

The sheet conductivity ($\sigma_S = 1/R_S$) of both doped and undoped samples was found to linearly depend on the number of LBA layers, as shown in the inset of figure 3(c). This indicates that appended LBA layers act as additional transport channels, and that the current is homogenously distributed across the entire film
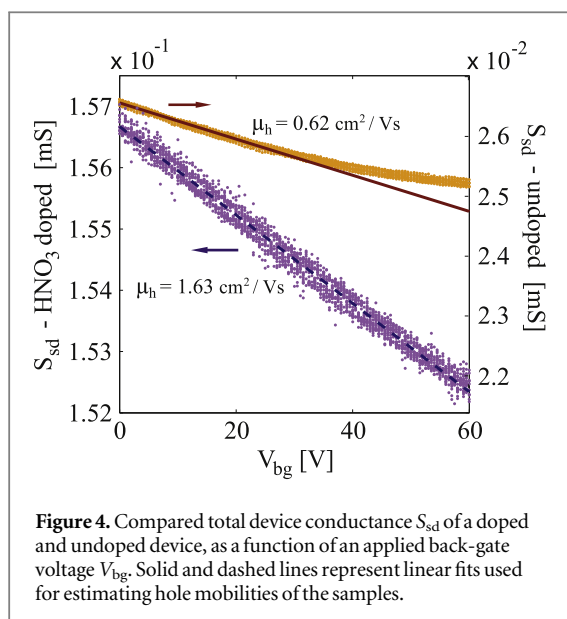
Figure 4. Compared total device conductance S_{sd} of a doped and undoped device, as a function of an applied back-gate voltage V_{bg}. Solid and dashed lines represent linear fits used for estimating hole mobilities of the samples.

when the distance between the electrodes is in the millimeter range [28].

3.5 Sheet resistivity and DC electrical characteristics measurements

The total resistance of each sample was measured in a two-point probe configuration, and the sheet resistivity was obtained by including the sample geometry factors. More details are given in supplementary information. The contact resistance was neglected being a three orders of magnitude smaller than the LBA GS film resistance. Sheet resistivity of as produced LBA GS films on PET was (70 ± 6) kΩ/□ for films with average thickness of 10 graphene layers. The sheet resistivity of the films after the doping was found to be reduced by the factor of five to six, reaching the value of (12 ± 3) kΩ/□. This change is two times larger than that reported for nitric acid doping of CVD graphene [17, 19, 28, 50]. Such a large reduction of sheet resistivity can be attributed to the fact that LPE based films have a large amount of un-functionalized GS edges, thus having more sites available for adsorption of NO_3^- and hydroxyl groups [53].

In order to characterize electrical properties of both undoped and chemically doped LBA GS films, measurements of direct-current (DC) electrical characteristics were carried out at room temperature. Device preparation, schematic representation of the measurement setups and measurements of the current between source (s) and drain (d) electrodes as a function of applied source–drain voltage V_{sd} are given in supplementary information.

Figure 4 shows the dependence of the total conductance (S_{ds}) as a function of back gate voltage (V_{bg}) for several consequent sweeps between 0 and 60 V. The negative slope of $S_{ds}(V_{bg})$ confirms that both undoped and chemically doped LBA GS films have holes as dominant charge carriers. Unintentional
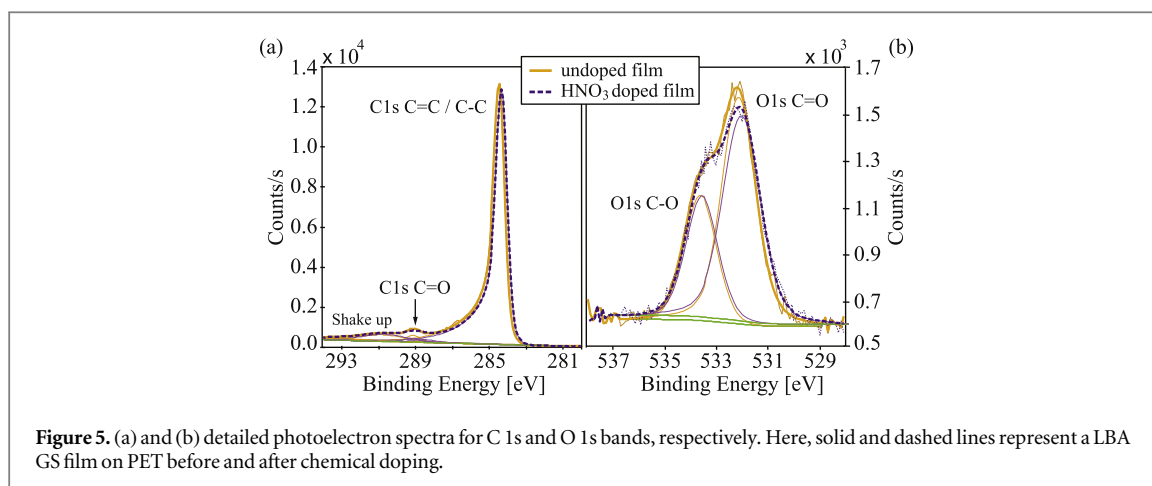
p-doping of the sample prior to the exposure to nitric acid is attributed to the remaining water and NMP residue at the interface during film transfer [32]. Conductance function was approximated to be linear, neglecting the deviation of the undoped sample at higher voltages, which is likely due to approaching a charge neutrality point. Using the linear approximation, carrier mobility has been estimated [43, 60] to be 0.6–0.8 cm^2 V^{-1} s^{-1} for the undoped samples, and 1.55–1.75 cm^2 V^{-1} s^{-1} for the samples that were exposed to nitric acid.

3.6 X-ray photoelectron spectroscopy (XPS)

XPS was used to elucidate the mechanisms behind the doping of graphene with HNO$_3$. Measurements were carried out on a Thermo Scientific Theta Probe XPS system, providing the quantitative elemental analysis. The samples were not encapsulated, and the measurements were carried out at room temperature without *in situ* heating. In addition, angle resolved XPS was used to obtain qualitative information of elemental distribution along the depth of the samples. Experimental details are given in supplementary information. XPS indicated the presence of carbon, oxygen, and nitrogen in the sample (see supplementary information figure S2). Nitrogen 1s core level intensities of undoped LBA GS film on PET imply nitrogen concentrations of $\sim$0.5 at%, which is an indication of intrinsic film doping by residual NMP [32].

Figures 5(a) and (b) show C 1s and O 1s core-level XPS spectra of the pristine and HNO$_3$-treated graphene films deposited on PET. In figure 5(a) the C 1s band is deconvoluted to reveal peaks corresponding to binding energies of graphene (sp^2)/C–C bonds (284.4 eV), as well as the C–O (288,6 eV) and C=O bonds (289.1 eV). The origin of a small C=O peak in the pristine graphene/PET sample may be from photoelectrons ejected from the PET substrate or from the water molecules trapped between the flakes in the film.

In figure 5(b), the O 1s band peak has been deconvoluted to reveal the C–O (533.6 eV) and C=O (532 eV) bonds. In both C 1s and O 1s bands the chemical modification by HNO$_3$ is evident through the change in the intensity of C=O peaks. This change is small (oxygen content is reduced from 7.3 to 5.9 at%) and can not solely account for the change in conductivity of graphene films after the treatment with nitric acid. The relative depth plot (see supplementary information figure S3) reveals the change in the elemental distribution across the graphene layer. In pristine graphene films, oxygen atoms are mostly placed closer to the surface layer, while in the acid-treated films the situation is reversed. This can be an indication of the rearrangement in the LBA graphene films on the substrate, with oxygen bonds established between the edges of the graphene flakes deeper in the film. This result is in accordance with the reduction of

Figure 5. (a) and (b) detailed photoelectron spectra for C 1s and O 1s bands, respectively. Here, solid and dashed lines represent a LBA GS film on PET before and after chemical doping.

the relative intensity of the D- and G-modes in our Raman spectra, corresponding to the GS edges.

The amount of nitrogen in acid-treated films increased from 0.5 to 1 at%. The nature of the measurements could potentially diminish in a small fraction the amount of nitrogen present in the sample. However, the samples were not heated and the nitrogen is incorporated within the film, therefore the change in at% of nitrogen that could arise from these measurements is neglected. In the high-resolution spectrum of N 1s band (see supplementary information figure S3), there is no evidence of the shift in binding energy corresponding to N–O or N–C chemical bonding. Its binding energy (399.8 eV) corresponds to previously reported conjugated nitrogen which does not belong to the graphene molecule [61].

XPS analysis indicates that nitrogen is not incorporated in the honeycomb lattice structure as this would result in n-doping of graphene [51]. The $C=O^-$, $C(O)OH^-$, and NO_3^- bonds are changing the carbon atoms hybridization and possibly allowing for the creation of edge-plane like catalytic sites in graphene [52, 62]. Which one of these chemical moieties is the most important factor contributing to the improved conductivity of HNO_3-treated graphene is not clear.

3.7 Transmittance measurements

The effect of chemical doping on optical properties of LBA GS films was investigated with measurements of optical transmittance, using a spectroscopic ellipsometer in photometric mode (SOPRA GES5E IRSE). Figure 6(a) shows the transmittance of a LBA GS film in the visible and UV ranges on quartz. In the UV, the transmittance of graphene is dominated by an exciton-shifted van Hove peak in absorption [63–65]. For this reason the measured data was fitted with a Fano resonant function [65, 66]. Average transmittance of a single LBA GS film at a wavelength of 650 nm was (78 ± 4)%. Considering that each layer of graphene absorbs 2.3% of incident light in the visible part of the spectrum [67] and has a thickness of 0.335 nm, the

average film thickness indicated by transmittance measurements is (3.2 ± 0.6) nm, in agreement with AFM measurements.

The transmittance of the doped film at the same wavelength is 74%, which is within the experimental error and the variation between individual samples (figure 6(a), shaded area). While the transmittance decreased only slightly with chemical doping, the sheet resistivity of this sample decreased by a factor of ~ 4.5.

3.8 Raman spectroscopy

Raman spectra of LBA GS films prior to and after nitric acid doping were also investigated. Room temperature measurements of Raman spectra were obtained using a TriVista 557 S&I GmbH Raman spectrometer ($\lambda = 532$ nm). Figure 6(b) shows Raman spectra of a LBA GS film on a glass substrate prior to (solid line) and after (dashed line) chemical doping, compared with graphite powder (dotted-line) before the LPE process. Analogous results were obtained for films on a PET substrate (see supplementary information), however in this case Raman spectra is dominated by PET modes. No significant shifts of any characteristic Raman modes of graphene (graphite) were detected after chemical doping. The only notable change of the Raman spectra due to chemical doping was the reduction of a $I(D)/I(G)$ relative intensity by 25% (see figure 6(b) inset). The relative intensity $I(D)/I(G)$ is indicative of the amount of GS edge scattering [68], hence our results point to a weakening of edge effects in doped films.

3.9 Work function measurements

The work function of a surface holds important information about the electronic structure. Using Kelvin probe force microscopy (KPFM, NTEGRA Spectra), we measured the work function of LBA GS films prior to and after chemical treatment, using the tabulated value of the work function for highly ordered pyrolytic graphite (HOPG) [69, 70] as a reference for
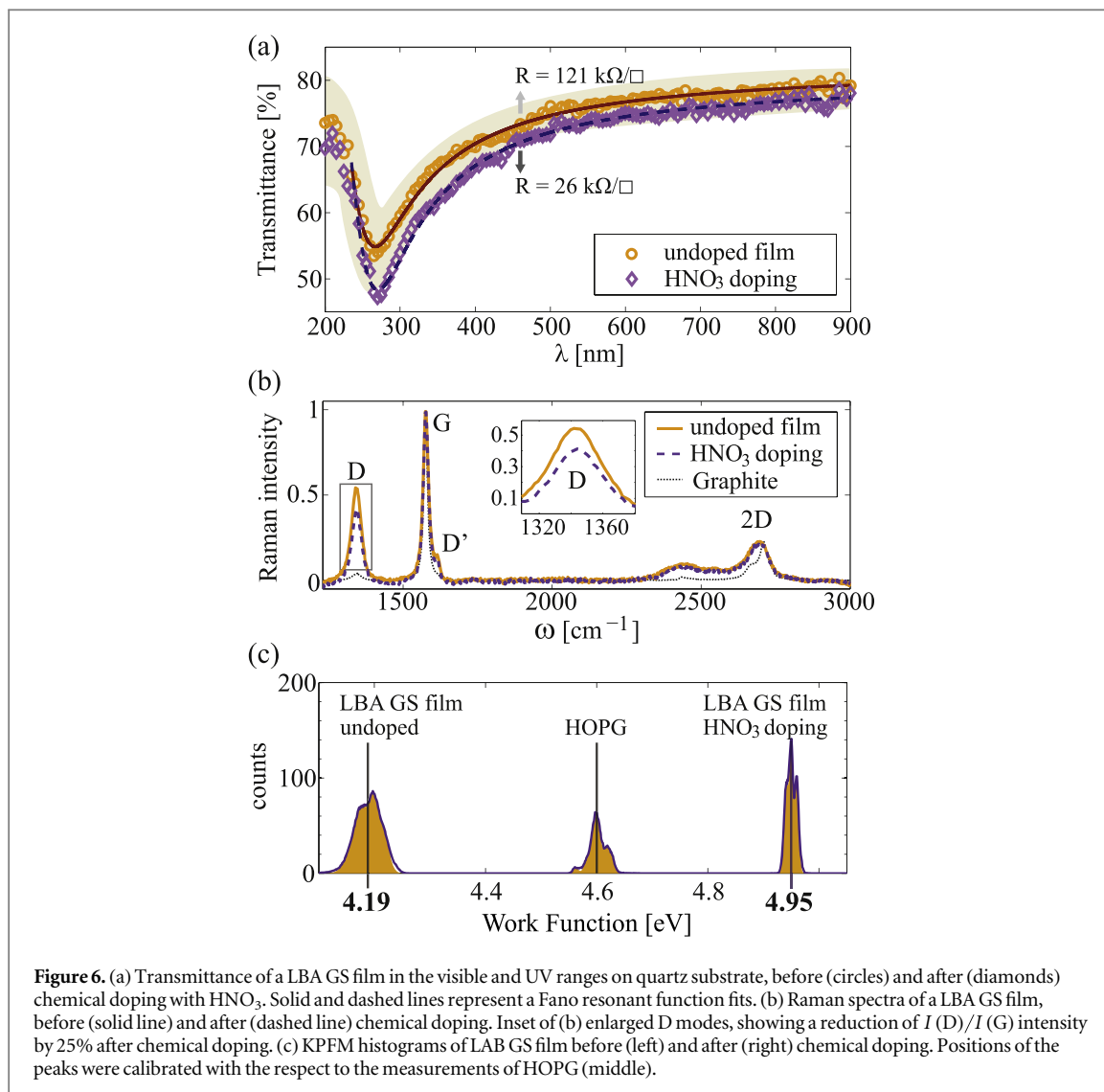
Figure 6. (a) Transmittance of a LBA GS film in the visible and UV ranges on quartz substrate, before (circles) and after (diamonds) chemical doping with HNO$_3$. Solid and dashed lines represent a Fano resonant function fits. (b) Raman spectra of a LBA GS film, before (solid line) and after (dashed line) chemical doping. Inset of (b) enlarged D modes, showing a reduction of I(D)/I(G) intensity by 25% after chemical doping. (c) KPFM histograms of LAB GS film before (left) and after (right) chemical doping. Positions of the peaks were calibrated with the respect to the measurements of HOPG (middle).

calibrating the AFM tip (details in supplementary information).

As a result, the work function values of (4.19 ± 0.05) eV and (4.95 ± 0.05) eV were obtained for the LBA GS films prior and after chemical doping, respectively. The results are presented in figure 6(c). Undoped films have much lower work function than HOPG, which is expected due to the presence of a large number of GS edges. Furthermore, this confirms that GSs are not functionalized, since in the case of reduced GO or surfactant assisted LPE much higher work functions of the resulting films are obtained [71].

Chemical doping with nitric acid increases the work function by as much as 0.75 eV, a 50% larger increase than in the case of a similar treatment of CVD graphene [17, 50]. An increase of the work function confirms that electrons migrate from GSs [72], resulting in further p-doping and a decrease of the Fermi level with the respect to Dirac point. Adsorption of NO$_3^-$ groups at the sheet edges is also expected to strongly contribute to the increase of the work function.

3.10 Dependence of the sheet resistivity upon axial strain

In addition to chemical doping, the change of the sheet resistivity of LBA GS films on PET substrates was investigated under various bending conditions. The curvature of the substrate was controlled by a micrometer screw in steps of 150 μm, as schematically presented in figure 7(a). The amount of bending is expressed as an axial strain (ϵ) that LBA GS films suffer at the surface of a PET substrate upon bending. Bending radii down to 6 mm were used, giving values of axial strain up to 1.6%. Stretched LBA GS films have shown an increase in the sheet resistivity, significantly larger than in the CVD graphene [9]. Upon axial strain of about 1.5% LBA GS films on PET substrate show an increase of sheet resistivity by as much as 50%. Furthermore, Raman spectra of strained films (given in supplementary information figure S5) did not show any detectable shifts of graphene modes. This indicates that individual GSs are not exhibiting a significant amount of strain. The change in sheet resistivity is attributed to increased separation between individual
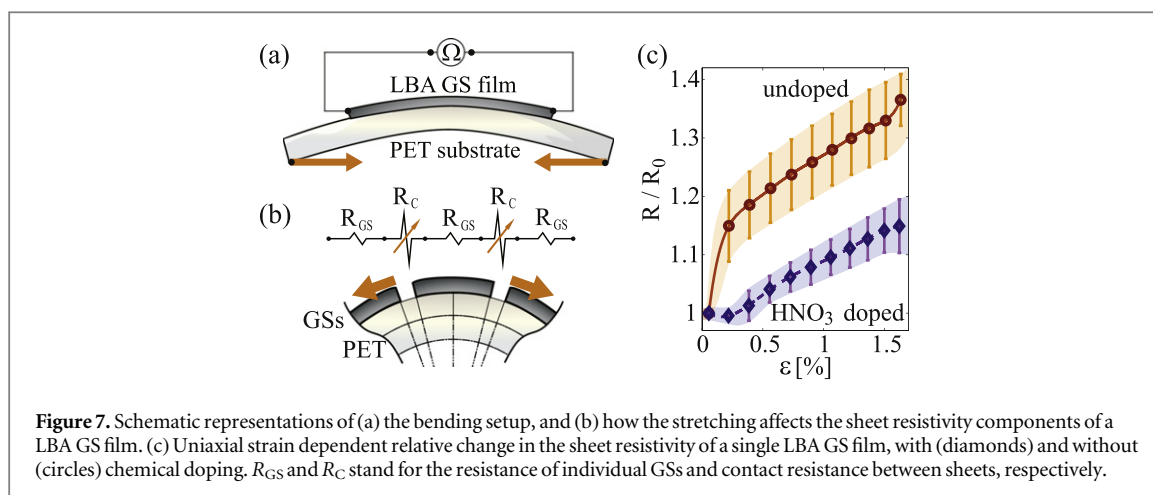
Figure 7. Schematic representations of (a) the bending setup, and (b) how the stretching affects the sheet resistivity components of a LBA GS film. (c) Uniaxial strain dependent relative change in the sheet resistivity of a single LBA GS film, with (diamonds) and without (circles) chemical doping. R_{GS} and R_C stand for the resistance of individual GSs and contact resistance between sheets, respectively.

GSs, which increases the contact resistance between them, as schematically presented in figure 7(b). The relative change in sheet resistivity upon bending reaches 20% larger values in undoped films, as presented in figure 7(c). A large change of resistance upon axial strain opens up a possibility to use LBA GS films in sensing applications as strain gauges, pressure sensors, touch screens or e-skin [73].

Chemically doped samples show a significantly different change in sheet resistivity under small axial strain. For bending radii greater than 30 mm (axial strain less than 0.3%) chemically doped samples show a negligible change in the sheet resistivity. On the other hand, undoped samples show more than 10% change for the same bending conditions. Axial strain of 0.3% would correspond to the separation between individual sheets of 0.36 nm when an averaged sheet diameter of 120 nm is considered. Interestingly, this is well matched with a thermochemical radii of NO_3^- anions. This indicates that NO_3^- groups attached at the edges of GSs provide a contact between the sheets until a high enough axial strain is reached. Afterwards, the sheet resistivity of the doped samples follow a similar trend as the undoped ones. This opens up a possibility to use chemically doped LBA GS films for flexible TCEs, in the cases when small bending radii are not required.

4 Conclusion

In summary, we have shown how the LBA of multilayer GSs produced from the dispersion in NMP and transferred on PET can be used to fabricate transparent and conductive films. An excellent adhesion of these films on PET enables for a straightforward chemical doping and stacking of multiple layers. In particular, p-type chemical doping with nitric acid has been used to reduce sheet resistivity and increase work function of these films, thus making them a more suitable low-cost alternative to CVD graphene for various TCE applications.

The sheet resistivity of deposited LBA GS layers on PET was found to be (70 ± 6) kΩ/□ with the transmittance of 78% at 650 nm wavelength. Upon a short exposure to nitric acid, sheet resistivity was reduced 5–6 fold, reaching the value of (12 ± 3) kΩ/□ with a minor reduction of the visible light transmittance. An increase of the LBA GS film work function by 0.75 eV was found upon chemical doping, yielding a value of 4.95 eV for the doped films. The work function measurements and the dependance of the sheet resistivity upon axial strain both indicate that a large reduction of the sheet resistivity occurs due to adsorption of NO_3^- groups at the edges of GSs. This reduces a contact resistance between the sheets, in addition to an increase of carrier concentration within the sheets.

Acknowledgments

References

[1] Novoselov K S, Falko V I, Colombo L, Gellert P R, Schwab M G and Kim K 2012 *Nature* **490** 192–200
[2] Ferrari A C *et al* 2014 *Nanoscale* **7** 4598–810
[3] Bonaccorso F, Colombo L, Yu G, Stoller M, Tozzini V, Ferrari A C, Ruoff R S and Pellegrini V 2015 *Science* **347** 1246501
[4] Segal M 2009 *Nat. Nanotechnol.* **4** 612–4
[5] Park S and Ruoff R S 2009 *Nat. Nanotechnol.* **4** 217–24
[6] Britnell L *et al* 2013 *Science* **340** 1311–4
[7] Bonaccorso F, Lombardo A, Hasan T, Sun Z, Colombo L and Ferrari A C 2012 *Mater. Today* **15** 564–89
[8] De S and Coleman J N 2010 *ACS Nano* **4** 2713–20
[9] Kim K S, Zhao Y, Jang H, Lee S Y, Kim J M, Kim K S, Ahn J-H, Kim P, Choi J-Y and Hong B H 2009 *Nature* **457** 706–10
[10] Blake P *et al* 2008 *Nano Lett.* **8** 1704–08
[11] Wang X, Zhi L and Mullen K 2008 *Nano Lett.* **8** 323–7
[12] Wang H-X, Wang Q, Zhou K-G and Zhang H-L 2013 *Small* **9** 1266–83

[13] Pang S, Hernandez Y, Feng X and Mullen K 2011 *Adv. Mater.* **23** 2779–95

[14] Kratzer M, Bayer B C, Kidambi P R, Matković A, Gajić R, Cabrero-Vilatela A, Weatherup R S, Hofmann S and Teichert C 2015 *Appl. Phys. Lett.* **106** 103101

[15] Chhikara M, Pavlica E, Matković A, Beltaos A, Gajić R and Bratina G 2014 *Carbon* **69** 162–8

[16] Miao X, Tongay S, Petterson M K, Berke K, Rinzler A G, Appleton B R and Hebard A F 2012 *Nano Lett.* **12** 2745–50

[17] Wu Y, Zhang X, Jie J, Xie C, Zhang X, Sun B, Wang Y and Gao P 2013 *J. Phys. Chem.* C **117** 11968–76

[18] Park H, Chang S, Zhou X, Kong J, Palacios T and Gradecak S 2014 *Nano Lett.* **14** 5148–54

[19] Bae S *et al* 2010 *Nat. Nanotechnol.* **5** 574–8

[20] Wu J, Agrawal M, Becerril H A, Bao Z, Liu Z, Chen Y and Peumans P 2010 *ACS Nano* **4** 43–8

[21] Han T-H, Lee Y, Choi M-R, Woo S-H, Bae S-H, Hong B H, Ahn J-H and Lee T-W 2012 *Nat. Photon.* **6** 105–10

[22] Coraux J, N'Diaye A T, Busse C and Michely T 2008 *Nano Lett.* **8** 565–70

[23] Reina A, Jia X, Ho J, Nezich D, Son H, Bulovic V, Dresselhaus M S and Kong J 2008 *Nano Lett.* **9** 30–5

[24] Li X *et al* 2009 *Science* **324** 1312–4

[25] Hao Y *et al* 2013 *Science* **342** 720–3

[26] Zaretski A V and Lipomi D J 2015 *Nanoscale* **7** 9963–9

[27] Li X, Zhu Y, Cai W, Borysiak M, Han B, Chen D, Piner R D, Colombo L and Ruoff R S 2009 *Nano Lett.* **9** 4359–63

[28] Kasry A, Kuroda M A, Martyna G J, Tulevski G S and Bol A A 2010 *ACS Nano* **4** 3839–44

[29] Stankovich S, Dikin D A, Dommett G H, Kohlhaas K M, Zimney E J, Stach E A, Piner R D, Nguyen S T and Ruoff R S 2006 *Nature* **442** 282–6

[30] Stankovich S, Dikin D A, Piner R D, Kohlhaas K A, Kleinhammes A, Jia Y, Wu Y, Nguyen S T and Ruoff R S 2007 *Carbon* **45** 1558–65

[31] Eda G, Fanchini G and Chhowalla M 2008 *Nat. Nanotechnol.* **3** 270–4

[32] Hernandez Y *et al* 2008 *Nat. Nanotechnol.* **3** 563–8

[33] Cai M, Thorpe D, Adamson D H and Schniepp H C 2012 *J. Mater. Chem.* **22** 24992–5002

[34] Coleman J N *et al* 2011 *Science* **331** 568–71

[35] Eda G, Yamaguchi H, Voiry D, Fujita T, Chen M and Chhowalla M 2011 *Nano Lett.* **11** 5111–6

[36] Withers F *et al* 2014 *Nano Lett.* **14** 3987–92

[37] Torrisi F *et al* 2012 *ACS Nano* **6** 2992–3006

[38] Secor E B, Prabhumirashi P L, Puntambekar K, Geier M L and Hersam M C 2013 *J. Phys. Chem. Lett.* **4** 1347–51

[39] Del S K, Bornemann R, Bablich A, Schäfer-Eberwein H, Li J, Kowald T, Östling M, Bolívar P H and Lemme M C 2015 *2D Mater.* **2** 011003

[40] Dikin D A, Stankovich S, Zimney E J, Piner R D, Dommett G H, Evmenenko G, Nguyen S T and Ruoff R S 2007 *Nature* **448** 457–60

[41] Li X, Zhang G, Bai X, Sun X, Wang X, Wang E and Dai H 2008 *Nat. Nanotechnol.* **3** 538–42

[42] Zhu Y, Cai W, Piner R D, Velamakanni A and Ruoff R S 2009 *Appl. Phys. Lett.* **95** 103104

[43] Kim H, Mattevi C, Kim H J, Mittal A, Mkhoyan K A, Riman R E and Chhowalla M 2013 *Nanoscale* **5** 12365–74

[44] Yang T, Yang J, Shi L, Mäder E and Zheng Q 2015 *RSC Adv.* **5** 23650–7

[45] Biswas S and Drzal L T 2008 *Nano Lett.* **9** 167–72

[46] Woltornist S J, Oyer A J, Carrillo J-M Y, Dobrynin A V and Adamson D H 2013 *ACS Nano* **7** 7062–6

[47] Salvatierra R V, Domingues S H, Oliveira M M and Zarbin A J 2013 *Carbon* **57** 410–5

[48] Geim A and Grigorieva I 2013 *Nature* **499** 419–25

[49] Yang H, Withers F, Gebremedhn E, Lewis E, Britnell L, Felten A, Palermo V, Haigh S, Beljonne D and Casiraghi C 2014 *2D Mater.* **1** 011012

[50] Lee S, Yeo J-S, Ji Y, Cho C, Kim D-Y, Na S-I, Lee B H and Lee T 2012 *Nanotechnology* **23** 344013

[51] Wei D, Liu Y, Wang Y, Zhang H, Huang L and Yu G 2009 *Nano Lett.* **9** 1752–8

[52] Das S, Sudhagar P, Ito E, Lee D-y, Nagarajan S, Lee S Y, Kang Y S and Choi W 2012 *J. Mater. Chem.* **22** 20490–7

[53] Zheng Q, Ip W H, Lin X, Yousefi N, Yeung K K, Li Z and Kim J-K 2011 *ACS Nano* **5** 6039–51

[54] Dresselhaus M S and Dresselhaus G 2002 *Adv. Phys.* **51** 1–86

[55] Fillaux F, Menu S, Conard J, Fuzellier H, Parker S, Hanon A and Tomkinson J 1999 *Chem. Phys.* **242** 273–81

[56] Lancellotti L, Bobeico E, Capasso A, Della Noce M, Dikonimos T, Lisi N and Delli Veneri P 2014 *2014 Fotonica AEIT Italian Conf. on Photonics Technologies* pp 1–3

[57] Larsen L J, Shearer C J, Ellis A V and Shapter J G 2015 *RSC Adv.* **5** 38851–8

[58] Wang J, Zhou M, Tan G, Chen S, Wu F, Lu J and Amine K 2015 *Nanoscale* **7** 8023–34

[59] Xie X, Su D, Zhang J, Chen S, Mondal A K and Wang G 2015 *Nanoscale* **7** 3164–72

[60] Liang X, Fu Z and Chou S Y 2007 *Nano Lett.* **7** 3840–4

[61] Wu Y, Fang S and Jiang Y 1999 *Solid State Ion.* **120** 117–23

[62] Kudin K N, Ozbas B, Schniepp H C, Prud'Homme R K, Aksay I A and Car R 2008 *Nano Lett.* **8** 36–41

[63] Kravets V G, Grigorenko A N, Nair R R, Blake P, Anissimova S, Novoselov K S and Geim A K 2010 *Phys. Rev.* B **81** 155413

[64] Mak K F, Shan J and Heinz T F 2011 *Phys. Rev. Lett.* **106** 046401

[65] Chae D-H, Utikal T, Weisenburger S, Giessen H, Klitzing K v, Lippitz M and Smet J 2011 *Nano Lett.* **11** 1379–82

[66] Matković A, Beltaos A, Milićević M, Ralević U, Vasić B, Jovanović D and Gajić R 2012 *J. Appl. Phys.* **112** 123523

[67] Nair R R, Blake P, Grigorenko A N, Novoselov K S, Booth T J, Stauber T, Peres N M R and Geim A K 2008 *Science* **320** 1308

[68] Khan U, O'Neill A, Lotya M, De S and Coleman J N 2010 *Small* **6** 864–71

[69] Yu Y-J, Zhao Y, Ryu S, Brus L E, Kim K S and Kim P 2009 *Nano Lett.* **9** 3430–4

[70] Takahashi T, Tokailin H and Sagawa T 1985 *Phys. Rev.* B **32** 8317

[71] Bausi F, Schlierf A, Treossi E, Schwab M G, Palermo V and Cacialli F 2015 *Org. Electron.* **18** 53–60

[72] Giovannetti G, Khomyakov P A, Brocks G, Karpan V M, van den Brink J and Kelly P J 2008 *Phys. Rev. Lett.* **101** 026803

[73] Zang Y, Zhang F, Di C-a and Zhu D 2015 *Mater. Horiz.* **2** 140–56

New Journal of Physics

CrossMark

OPEN ACCESS

PAPER

Enhanced structural stability of DNA origami nanostructures by graphene encapsulation

Aleksandar Matković[1,5], Borislav Vasić[1], Jelena Pešić[1], Julia Prinz[2], Ilko Bald[2,3], Aleksandar R Milosavljević[4,6] and Radoš Gajić[1]

1   Center for Solid State Physics and New Materials, Institute of Physics, University of Belgrade, Pregrevica 118, 11080 Belgrade, Serbia
2   Institute of Chemistry—Physical Chemistry, University of Potsdam, Potsdam, Germany
3   BAM Federal Institute for Materials Research and Testing, Richard-Willsttter Str. 11, D-12489 Berlin, Germany
4   Laboratory for Atomic Collision Processes, Institute of Physics, University of Belgrade, Pregrevica 118, 11080 Belgrade, Serbia
5   *Present address*: Institute of Physics, Montanuniversität Leoben, Franz Josef Straße 18, A-8700 Leoben, Austria.
6   *Present address*: Radiation Laboratory, University of Notre Dame, Notre Dame, IN 46556, USA.

E-mail: bvasic@ipb.ac.rs

Keywords: graphene, DNA origami nanostructures, atomic force microscopy

Abstract

We demonstrate that a single-layer graphene replicates the shape of DNA origami nanostructures very well. It can be employed as a protective layer for the enhancement of structural stability of DNA origami nanostructures. Using the AFM based manipulation, we show that the normal force required to damage graphene encapsulated DNA origami nanostructures is over an order of magnitude greater than for the unprotected ones. In addition, we show that graphene encapsulation offers protection to the DNA origami nanostructures against prolonged exposure to deionized water, and multiple immersions. Through these results we demonstrate that graphene encapsulated DNA origami nanostructures are strong enough to sustain various solution phase processing, lithography and transfer steps, thus extending the limits of DNA-mediated bottom-up fabrication.
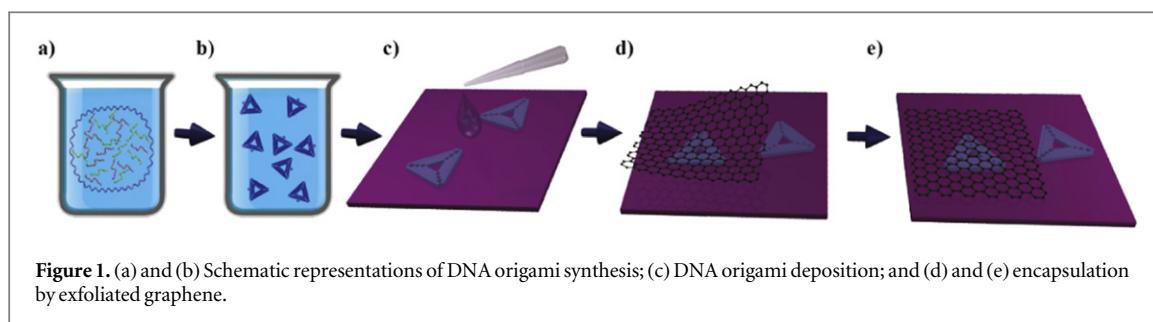
1. Introduction

Artificial deoxyribonucleic acid (DNA) macromolecules offer highly controllable bottom-up fabrication of various nanostructures. Since the first demonstration of DNA folding and the wide variety of structures and patterns that can be created at nanoscale [1], many 2D and 3D DNA origami nanostructures were fabricated using this method [2–4]. These structures often serve as substrates [5], offering a solution-based self-assembly with nanometer precision geometries. DNA nanostructures have been used as scaffolds for assembly of metallic nanoparticles [6–8], for routing polymers [9], surface-enhanced Raman scattering [10], as positive and negative masks for DNA nano-lithography [11–14], and even graphene patterning [15].

However, the delicate nature of DNA origami nanostructures constrains their applicability in bottom-up fabrication [16]. In particular any mechanical wear or solution phase processing could damage these nanostructures [7, 17, 18]. Thus enhancing the structural stability of DNA origami nanostructures is crucial for expanding the field of bottom-up nanofabrication.

On the other hand, graphene, a single atomic layer of crystal graphite, with its peerless mechanical properties can offer a solution to this issue. Youngs modulus of graphene is about five times greater than of the bulk steel [19, 20], while at the same time graphene can be folded by 180° over less than one nanometer in length, without breaking its in-plane bonds. The crystal lattice of graphene (and graphite) is so densely packed that it is impermeable to any gases, even H_2 [21]. Also, graphene has low friction coefficient [22], and has been employed as a protective coating for friction reduction [23–27], wear protection [28, 29] and as corrosion barriers [30].

Recently, graphene has been employed to encapsulate objects such as single yeast cells [31], bacteria [32], water molecules [33–42], fluorescent films [43], single-stranded DNA and DNA nanostructures [44, 45]. It was demonstrated that graphene replicates the topography of the DNA molecules [44, 45]. Also, the directed

Figure 1. (a) and (b) Schematic representations of DNA origami synthesis; (c) DNA origami deposition; and (d) and (e) encapsulation by exfoliated graphene.

deposition of DNA rectangles onto lithography patterned strips of nitrogen-doped reduced graphene oxide was demonstrated [46].

In this study we focus on enhancing the structural stability of DNA origami nanostructures by graphene encapsulation. For this purpose triangular DNA origami nanostructures are deposited onto silicon substrates and encapsulated by single layer exfoliated graphene. The morphology of DNA origami nanostructures is very well transferred to the graphene, having even the inner triangle clearly resolved by atomic force microscopy (AFM). The samples are tested for their structural stability using AFM based manipulation and aqueous solution exposure. The forces required to damage bare and graphene encapsulated nanostructures are compared, and the effects of cumulative damage introduced by successive manipulations are investigated. In addition, stability of graphene encapsulated DNA origami nanostructures is tested against prolonged exposure to deionized water (DI H_2O).

2. Materials and methods

2.1. DNA origami synthesis

Triangular DNA origami nanostructures were synthesized according to a modified version of Rothemund's method (schematically represented in figures 1(a) and (b)) [1]. Therefore, the M13mp18 virus strand (5 nM, New England Biolabs) serving as scaffold and 208 short staple strands (Integrated DNA Technologies) were mixed in a molar ratio of 1:30 in 1×TAE (Sigma Aldrich) with 10 mM $MgCl_2$ (total volume 100 μl). The mixture was annealed by gradually decreasing the temperature from 80 °C to 8 °C within 1 h 48 min using a Primus 25 advanced thermal cycler (Peqlab). Excess staple strands were removed by spin filtering the resulting DNA origami solution two times at 3830 g for 10 min using Amicon Ultra-0.5 filters (100 kDa MWCO, Millipore) after the addition of 200 μl (first run) or 300 μl (second run) of 1×TAE with 10 mM $MgCl_2$.
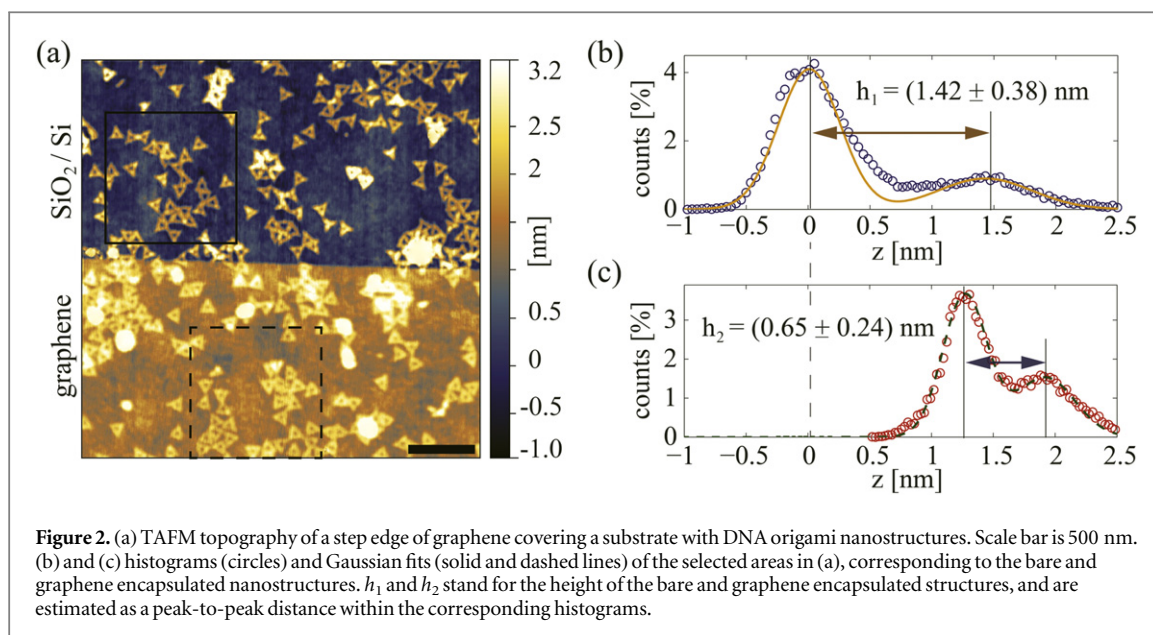
2.2. DNA origami deposition

After preparation, triangular DNA origami nanostructures were deposited onto ∼1 × 1 cm^2 silicon substrates covered with 80 nm thick dry thermal oxide (SiO_2/Si). Due to the interference of the light within the oxide layer, optical contrast of the graphene is enhanced and enables good visibility of graphene using optical microscopy, which is essential for the identification [47].

Before the deposition of DNA origami nanostructures, the substrates were cleaned and prepared by 5 min treatment in Novascan's ozone cleaner. Subsequently, drops of 0.5 μl of DNA origami solution were deposited on each substrate and covered with 10 μl of 10×TAE with 10 mM of $MgCl_2$. After one hour of incubation period in the water-saturated environment, the samples were rinsed in 1:1 water-ethanol solution to clean excess of material and dried with an argon gun (flow ∼10 l min^{-1}). As a result DNA origami nanostructures covered the entire substrates with an averaged density of twenty triangular nanostructures per square micrometer. The DNA origami deposition is schematically represented in figure 1(c).

2.3. Graphene exfoliation

Graphene was deposited using the procedure known as micromechanical cleavage [48], yielding high-quality layers of graphene but limited in lateral size (on the order of tens of micrometers in diameter). Kish graphite (Naturgraphite GmbH) was used as starting material. Graphite flakes were cleaved using sticky tape (Nitto Denko ELP BT150ECM) and deposited on the substrates with DNA origami nanostructures. In order to avoid damaging DNA origami nanostructures, the entire micromechanical exfoliation was carried out at room temperature. After the deposition of graphene on top of the DNA origami nanostructures, individual flakes were detected using optical microscopy and single atomic layer samples were chosen by the optical contrast, and confirmed by the AFM. Schematic representation of the encapsulation by graphene is shown in figures 1(d) and (e).

Figure 2. (a) TAFM topography of a step edge of graphene covering a substrate with DNA origami nanostructures. Scale bar is 500 nm. (b) and (c) histograms (circles) and Gaussian fits (solid and dashed lines) of the selected areas in (a), corresponding to the bare and graphene encapsulated nanostructures. h_1 and h_2 stand for the height of the bare and graphene encapsulated structures, and are estimated as a peak-to-peak distance within the corresponding histograms.
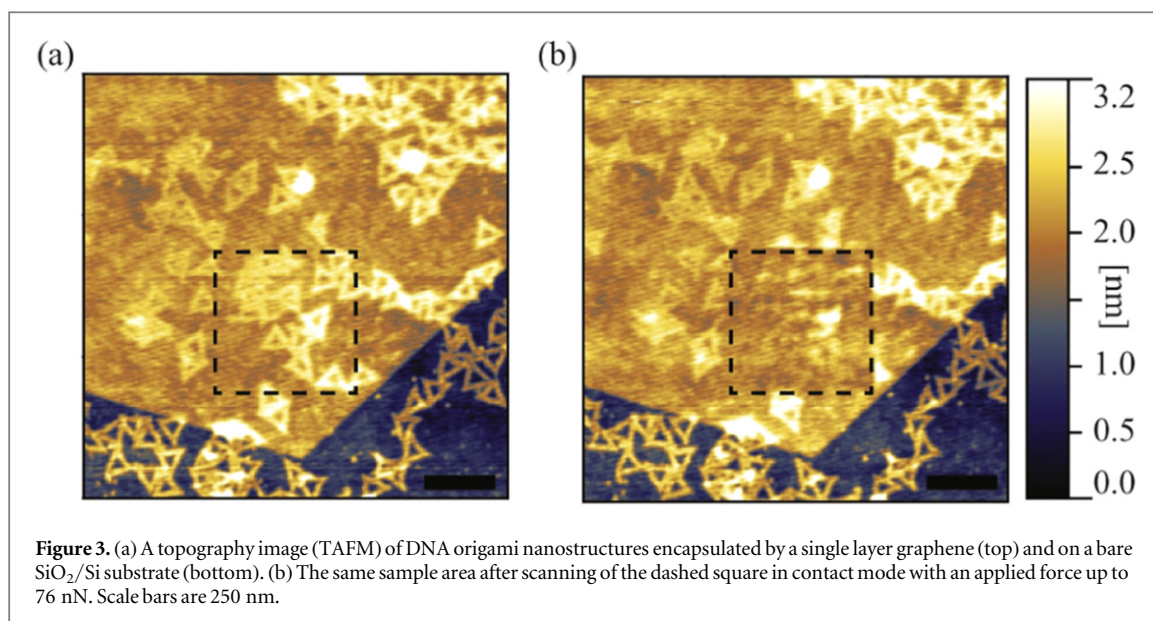
2.4. AFM measurements

AFM experiments were carried out on the NT-MDT's NTEGRA Prima system. Imaging before and after AFM manipulation was performed in tapping mode (TAFM), using NSG01 probes from NT-MDT (typical force constant 5.1 N m^{-1}). AFM manipulation was done in contact mode, using NT-MDT's CSG01 probes (typical force constant 0.03 N m^{-1}). All measurements were done at ambient conditions. Initial imaging of the samples was done in TAFM mode. In this mode, the vibrating AFM tip is free from a torsion, so it does not push DNA origami nanostructures laterally leaving them practically intact.

AFM manipulation of graphene has been done using both static [49, 50] and dynamic plowing [51]. Here, AFM manipulation experiments were done in the following way. After selected sample areas were found and visualized using TAFM mode, AFM manipulations were carried out in contact mode, by scanning a selected sample area. Every image was recorded at constant normal force (constant set point). Manipulation on the graphene encapsulated DNA origami nanostructures was carried out using TAFM (NGS01, force constant 5.1 N m^{-1}). However, imaging of bare DNA nanostructures was not possible in contact mode with these hard cantilevers. For this reason the manipulation of bare nanostructures was done using soft CSG01 probes (with two order of magnitude lower force constant).

AFM topography images of the samples were processed in an open source software Gwyddion. For each image first a mean plane was subtracted, followed by line corrections in the scanning direction, and finally a three point plane leveling is applied and the mean height is set to zero value. In the cases of graphene/substrate step edges, the three points were chosen on the bare substrate.

3. Results and discussion

A typical TAFM topography image of a step edge of graphene, with (1.26 ± 0.21) nm height, covering a substrate with DNA origami nanostructures is shown in figure 2(a). In order to estimate the structural damage, both the height and the shapes of the triangular DNA origami nanostructures were considered. The shapes were straightforwardly assessed from the topography images. The height of the structures was determined using a peak-to-peak difference from the selected area histograms, as shown in figures 2(b) and (c). Each histogram peak was fitted by a single Gaussian line. The uncertainty of the measured height was estimated as a half width at half maximum of the histogram peak that corresponds to either bare or graphene encapsulated DNA origami nanostructures. As a result, an average height of the bare triangular DNA origami nanostructures was found to be (1.42 ± 0.38) nm, while the graphene encapsulated ones were (0.65 ± 0.24) nm high. The observed difference is due to non-perfect replication of DNA origami by graphene. Some parts of graphene covering DNA nanostructures do not lie perfectly on SiO$_2$ substrate. These parts of graphene are slightly lifted above the substrate and make the effective height of the graphene covered DNA nanostructures smaller. This effect is even more pronounced for high density of deposited DNA origami nanostructures since graphene does not fall perfectly on SiO$_2$ substrate between adjacent DNA nanostructures.

Figure 3. (a) A topography image (TAFM) of DNA origami nanostructures encapsulated by a single layer graphene (top) and on a bare SiO$_2$/Si substrate (bottom). (b) The same sample area after scanning of the dashed square in contact mode with an applied force up to 76 nN. Scale bars are 250 nm.
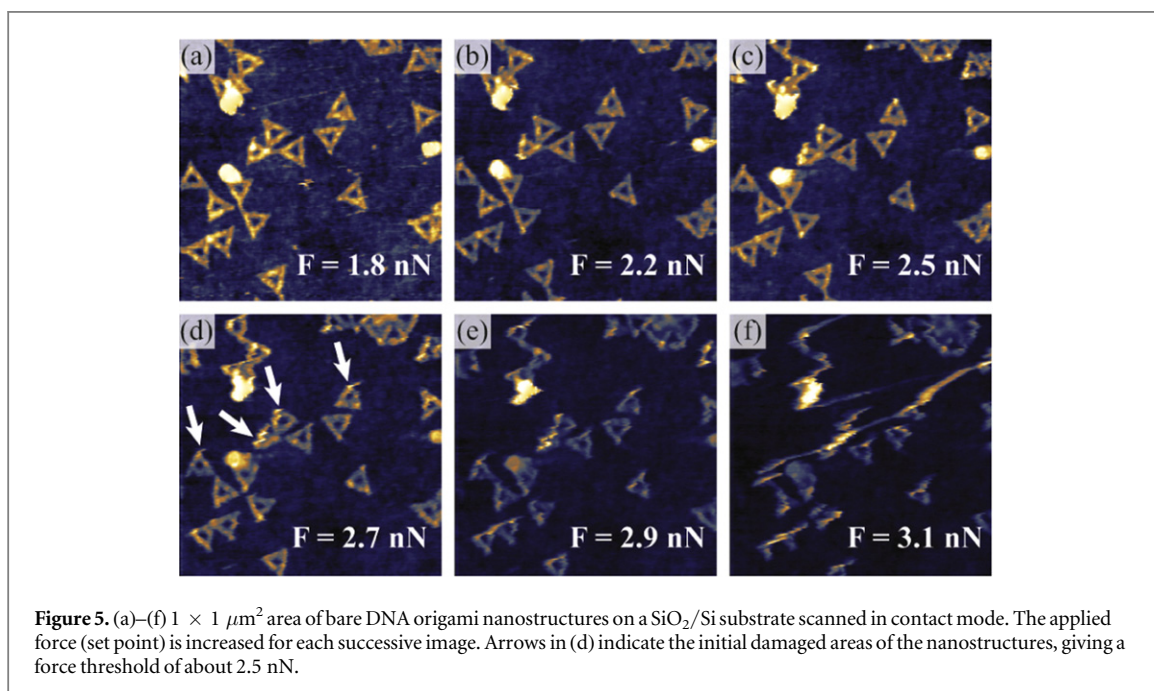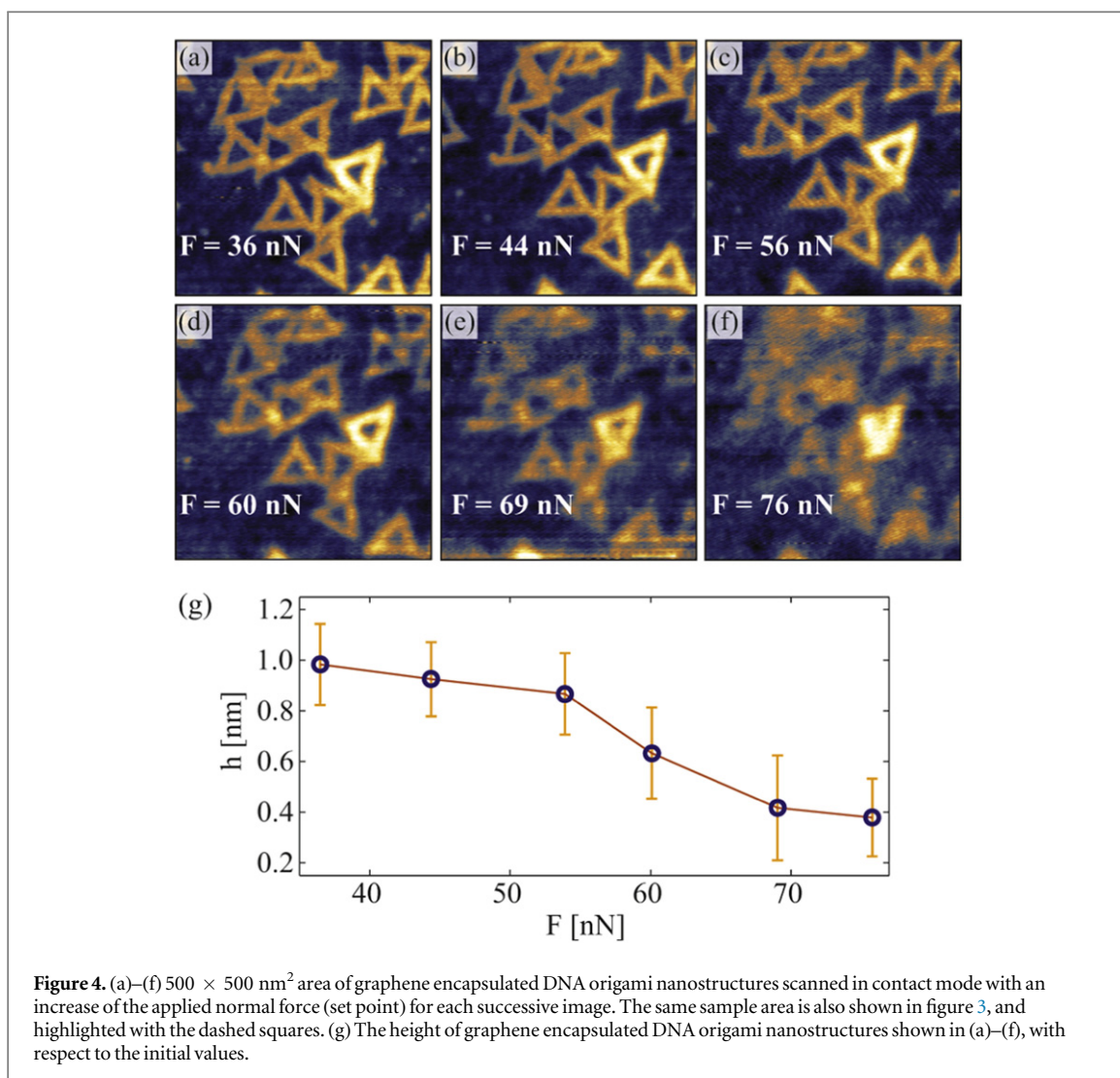
3.1. AFM manipulation

Imaging of DNA nanostructures in the contact mode is challenging [44]. Therefore, so far their mechanical properties and stability have been measured using peak force tapping mode with precisely controlled force in pico Newton range [52]. Here AFM manipulation in contact mode was applied in order to determine the forces required to damage both bare and graphene encapsulated DNA origami nanostructures. Figure 3 shows TAFM topography of DNA origami nanostructures before and after manipulation of a 500 $\times$ 500 nm^2 selected area, marked by the dashed square. The selected area was repeatedly scanned six times in contact mode. The applied normal force was increased for each successive scan ranging from 36 to 76 nN. The contact mode topography scans are shown in figures 4(a)–(f). The same probe (NGS01) was used both for the imaging of the sample in TAFM mode and for the manipulation in contact mode. The height of the encapsulated nanostructures was estimated for each contact mode scan using their corresponding histogram peak-to-peak distance. The results are presented in figure 4(g), showing encapsulated structure height as a function of the applied normal force. Both the height and the shape of the triangular origami nanostructures indicate that structural damage starts to occur when a normal force of about 60 nN is exerted.
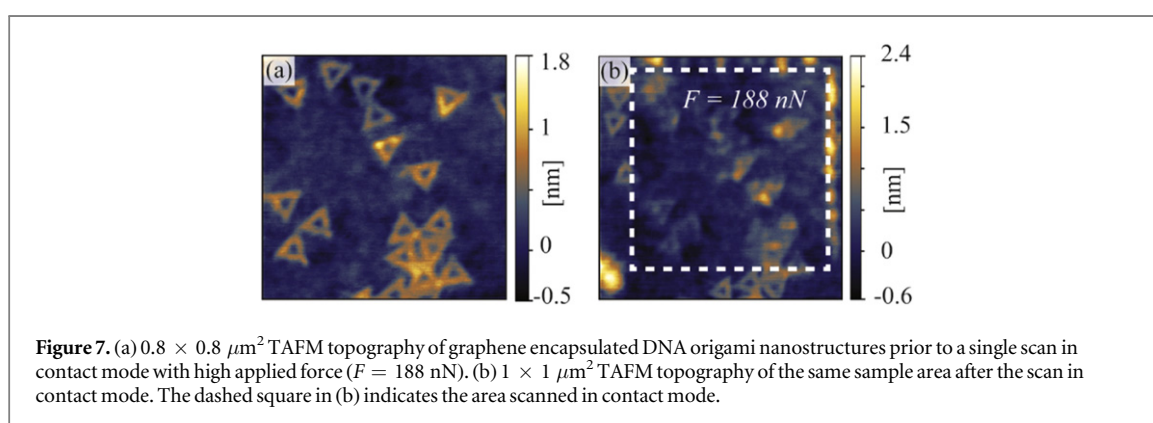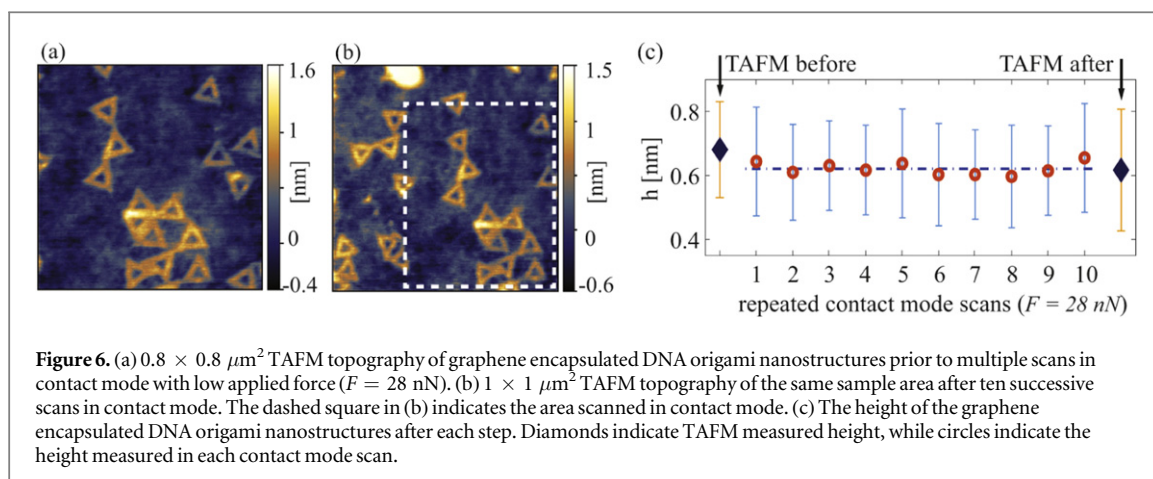
In order to estimate the amount of mechanical protection that graphene offers to DNA origami nanostructures, the same AFM manipulation experiments are carried out on the bare triangular DNA origami nanostructures (on SiO$_2$/Si substrate). Here much smaller normal forces are required to damage the structures. Thus, a soft mode probes (CSG01) were used, with the typical force constant of 0.03 N m^{-1}. Figure 5 shows six subsequent scans in contact mode. Again, the normal force is increased for each scan, ranging from 1.8 to 3.1 nN. The triangular DNA origami nanostructures appeared unchanged up to the normal force of 2.5 nN.

The nature of the structural damage that is introduced by the AFM probe is different for the bare and graphene encapsulated DNA origami nanostructures. In the case of the encapsulated nanostructures graphene protects them from attaching to the tip of the AFM probe. As a result, the damaged structures appeared ”smudged” and their height is reduced. On the other hand the bare nanostructures tend to attach to the tip and drift in the scanning direction. As a result the height of the bare structures that were not pushed and damaged by the AFM probe does not change significantly (figure 5(f)).

The arrows in figure 5(d) indicate the initial damage of the bare DNA origami nanostructures, that is introduced with the normal force of only 2.7 nN. Compared with the same tests carried out on the encapsulated structures (figure 4), the force required to damage the DNA origami nanostructures is over an order of magnitude greater for the ones encapsulated with graphene. The structural damage that can be introduced by AFM manipulation strongly depends on the adhesion of both the DNA nanostructures and the graphene layer to the substrate. For this reason it is not reliable to set the exact force threshold at which graphene offers wear protection to these structures.

Still the question remains whether the cumulative damage arises when the same graphene encapsulated structures are scanned multiple times. To test this the same graphene encapsulated area was scanned in contact mode ten times successively. The normal force was set to 28 nN for all scans. TAFM topography images of the same sample area before and after manipulation are respectively shown in figures 6(a) and (b). Figure 6(c) shows the height of the graphene encapsulated DNA origami nanostructures for each TAFM and contact mode scan.

Figure 4. (a)–(f) 500×500 nm^2 area of graphene encapsulated DNA origami nanostructures scanned in contact mode with an increase of the applied normal force (set point) for each successive image. The same sample area is also shown in figure 3, and highlighted with the dashed squares. (g) The height of graphene encapsulated DNA origami nanostructures shown in (a)–(f), with respect to the initial values.

Figure 5. (a)–(f) 1×1 μm^2 area of bare DNA origami nanostructures on a SiO$_2$/Si substrate scanned in contact mode. The applied force (set point) is increased for each successive image. Arrows in (d) indicate the initial damaged areas of the nanostructures, giving a force threshold of about 2.5 nN.

Figure 6. (a) 0.8 × 0.8 μm² TAFM topography of graphene encapsulated DNA origami nanostructures prior to multiple scans in contact mode with low applied force ($F = 28$ nN). (b) 1 × 1 μm² TAFM topography of the same sample area after ten successive scans in contact mode. The dashed square in (b) indicates the area scanned in contact mode. (c) The height of the graphene encapsulated DNA origami nanostructures after each step. Diamonds indicate TAFM measured height, while circles indicate the height measured in each contact mode scan.

Figure 7. (a) 0.8 × 0.8 μm² TAFM topography of graphene encapsulated DNA origami nanostructures prior to a single scan in contact mode with high applied force ($F = 188$ nN). (b) 1 × 1 μm² TAFM topography of the same sample area after the scan in contact mode. The dashed square in (b) indicates the area scanned in contact mode.

The heights were obtained as a peak-to-peak distance from their corresponding topography images. The results show that there is no cumulative damage effect if the applied normal force is below the damage threshold ($\sim$60 nN).

On the other hand, only a single contact mode scan with high enough force is sufficient to damage graphene encapsulated nanostructures. This is demonstrated in figure 7. Here, TAFM topography images are shown before and after the selected area was scanned in contact mode with the normal force set to 188 nN, well above the damage threshold.
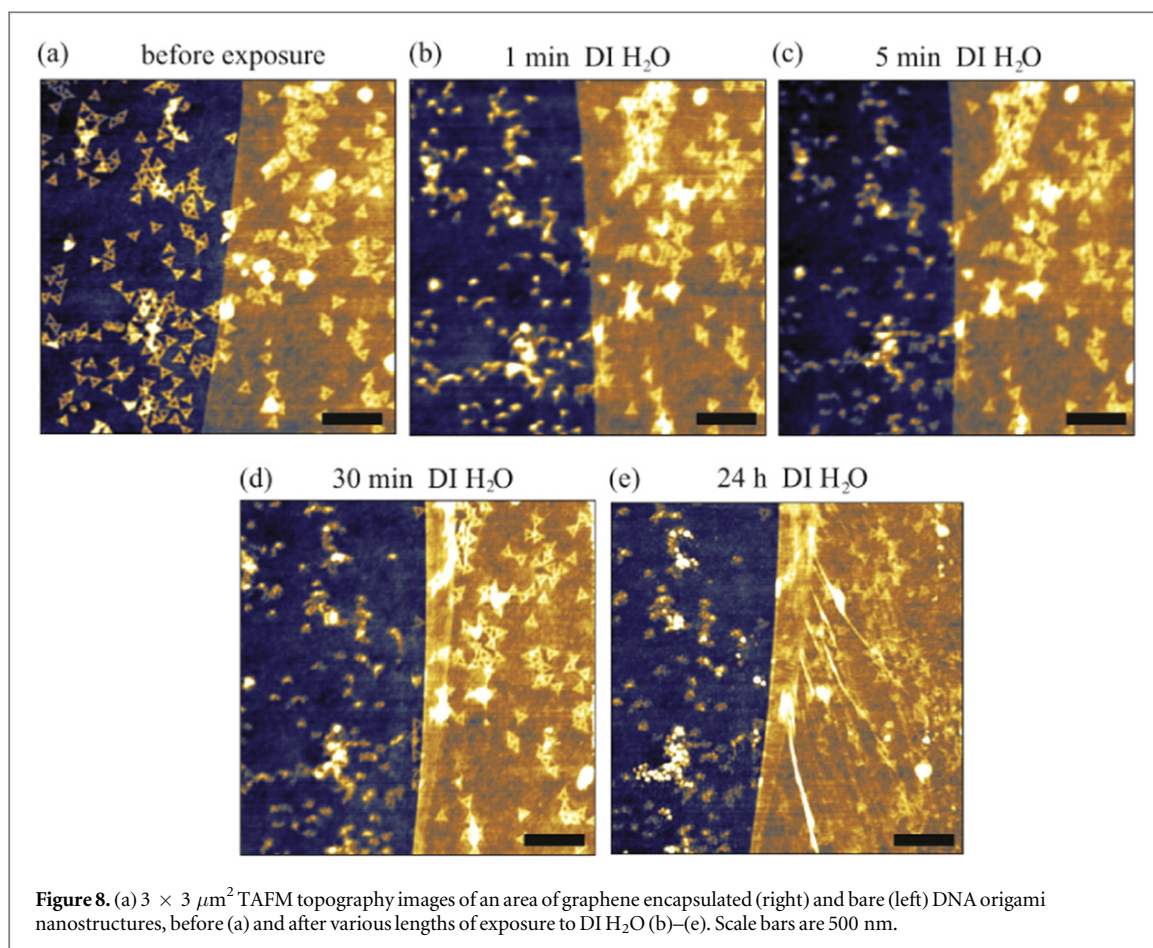
3.2. Deionized water exposure

In order to extend the use of DNA origami nanostructures as scaffolds in the bottom-up nanofabrication [16], these structures need to be strong enough to withstand the harsh conditions needed in many fabrication steps [18]. Commonly these steps include submersion into liquids. Either as the part of the solution phase processing or simple rinsing after a lithography step, DNA origami nanostructures need to withstand both short and prolonged liquid exposures.

In this study the exposure to deionized water was tested on both bare and graphene encapsulated structures. The exposure time was varied between 1 min and 24 h. The SiO$_2$/Si substrates covered with DNA origami nanostructures and partly encapsulated by graphene were submerged into 10 mL of DI H$_2$O (Millipore, 18,2 MΩ cm^{-1}) and after the set exposure time quickly dried with an argon gun (flow $\sim$10 l min^{-1}). Water exposure was done successively on each flake, e.g.: the flake was exposed to 1 min in DI H$_2$O, measured, then again exposed for 4 min more to give the total of 5 min exposure, and so on. This way properties that are unique for every sample, as adhesion of nanostructures and graphene to the substrate, did not figure in the test.

The selected sample areas were imaged using TAFM both prior and after DI H$_2$O exposure. Figure 8 shows TAFM topography images of triangular DNA origami nanostructures partly encapsulated by graphene before exposure (a) and after various lengths of exposure to DI H$_2$O (b)–(e).

The unprotected structures are significantly damaged even after only 1 min of DI H$_2$O exposure, and not lifted-off the substrate. Most likely the amount of residual Mg^{2+} ions on the substrate surface determines whether the structures are damaged or lifted-off the substrate [18].

Figure 8. (a) $3 \times 3 \ \mu m^2$ TAFM topography images of an area of graphene encapsulated (right) and bare (left) DNA origami nanostructures, before (a) and after various lengths of exposure to DI H_2O (b)–(e). Scale bars are 500 nm.

Graphene encapsulated DNA origami nanostructures appeared to be intact by the water exposure. Each individual triangular origami was preserved even after 30 min of DI H_2O exposure. The height of the nanostructures was also unchanged. In the case of the sample shown in figures 8(a)–(d) the height of the encapsulated origami nanostructures was $0.8(\pm0.2)$ nm, after each exposure. In figure 8(d) the edge of graphene sample was folded, most likely during the drying step.

The only exception occurred after twenty four hours of exposure. In this case graphene started to wrinkle. Although some triangular DNA origami nanostructures are still visible underneath graphene (figure 8(f)), most of the nanostructures were damaged and their height estimation was not reliable.

The exact exposure time threshold will again depend on the adhesion to the substrate of both graphene and DNA origami nanostructures, and varies from sample to sample. Still, very short exposures do damage or lift-off bare DNA nanostructures [18]. On the other hand graphene encapsulation offers significant protection increasing the exposure times by at least two orders of magnitude.

4. Conclusion

In summary, we have demonstrated that single layer exfoliated graphene can be used as a protective layer for DNA origami nanostructures. Through the AFM based manipulation we have shown that the normal force required to damage graphene encapsulated DNA origami nanostructures is over an order of magnitude greater than for the unprotected ones. The threshold for the normal force that induces structural damage to the graphene encapsulated DNA origami nanostructures was found to be about 60 nN. In addition, we have shown that graphene provides wear protection against multiple manipulations if the applied normal force is below the damage threshold.

Besides wear protection, graphene encapsulated DNA origami nanostructures were tested against prolonged exposure to deionized water, and multiple immersions. We show that graphene encapsulated nanostructures remain intact even after 30 min of the exposure to deionized water, while the bare structures are significantly damaged in the matter of seconds. The limits of graphene protection against deionized water exposure arise from wrinkling of the graphene layer itself.

We expect that other liquids will act in the similar manner as long as they do not damage graphene, and will only take different amount of time to damage bare DNA origami nanostructures. This extends the use of DNA origami scaffolds in many fabrication processes, as various lithography steps or wet transfer of 2D materials. Future studies could involve encapsulation by more than one layer of graphene and the use of other 2D materials, as hexagonal boron nitride, which could prove protection in harsh environments that graphene might not be suitable for.

Acknowledgments

References

[1] Rothemund P W K 2006 Folding DNA to create nanoscale shapes and patterns *Nature* **440** 297–302

[2] Han D, Pal S, Nangreave J, Deng Z, Liu Y and Yan H 2011 DNA origami with complex curvatures in three-dimensional space *Science* **332** 342–6

[3] Ke Y, Ong L L, Shih W M and Yin P 2012 Three-dimensional structures self-assembled from DNA bricks *Science* **338** 1177–83

[4] Wei B, Dai M and Yin P 2012 Complex shapes self-assembled from single-stranded DNA tiles *Nature* **485** 623–6

[5] Bald I and Keller A 2014 Molecular processes studied at a single-molecule level using DNA origami nanostructures and atomic force microscopy *Molecules* **19** 13803–23

[6] Li H, Park S H, Reif J H, LaBean T H and Yan H 2004 DNA-templated self-assembly of protein and nanoparticle linear arrays *J. Am. Chem. Soc.* **126** 418–9

[7] Geng Y, Liu J, Pound E, Gyawali S, Harb J N and Woolley A T 2011 Rapid metallization of lambda DNA and DNA origami using a Pd seeding method *J. Mater. Chem.* **21** 12126–31

[8] Schreiber R, Kempter S, Holler S, Schüller V, Schiffels D, Simmel S S, Nickels P C and Liedl T 2011 DNA origami-templated growth of arbitrarily shaped metal nanoparticles *Small* **7** 1795–9

[9] Knudsen J B *et al* 2015 Routing of individual polymers in designed patterns *Nat. Nanotechnol.* **10** 892–8

[10] Prinz J, Schreiber B, Olejko L, Oertel J, Rackwitz J, Keller A and Bald I 2013 DNA origami substrates for highly sensitive surface-enhanced Raman scattering *J. Phys. Chem. Lett.* **4** 4140–5

[11] Becerril H A and Woolley A T 2007 DNA shadow nanolithography *Small* **3** 1534–8

[12] Deng Z and Mao C 2004 Molecular lithography with DNA nanostructures *Angew. Chem. Int. Ed.* **43** 4068–70

[13] Surwade S P, Zhao S and Liu H 2011 Molecular lithography through DNA-mediated etching and masking of SiO_2 *J. Am. Chem. Soc.* **133** 11868–71

[14] Surwade S P, Zhou F, Wei B, Sun W, Powell A, ODonnell C, Yin P and Liu H 2013 Nanoscale growth and patterning of inorganic oxides using DNA nanostructure templates *J. Am. Chem. Soc.* **135** 6778–81

[15] Jin Z, Sun W, Ke Y, Shih C-J, Paulus G L C, Wang Q H, Mu B, Yin P and Strano M S 2013 Metallized DNA nanolithography for encoding and transferring spatial information for graphene patterning *Nat. Commun.* **4** 1663

[16] Zhang G, Surwade S P, Zhou F and Liu H 2013 DNA nanostructure meets nanofabrication *Chem. Soc. Rev.* **42** 2488–96

[17] Liu J, Geng Y, Pound E, Gyawali S, Ashton J R, Hickey J, Woolley A T and Harb J N 2011 Metallization of branched DNA origami for nanoelectronic circuit fabrication *ACS Nano* **5** 2240–7

[18] Kim H, Surwade S P, Powell A, ODonnell C and Liu H 2014 Stability of DNA origami nanostructure under diverse chemical environments *Chem. Mater.* **26** 5265–73

[19] Lee C, Wei X, Kysar J W and Hone J 2008 Measurement of the elastic properties and intrinsic strength of monolayer graphene *Science* **321** 385–8

[20] Lee G H *et al* 2013 High-strength chemical-vapor-deposited graphene and grain boundaries *Science* **340** 1073–6

[21] Bunch J S, Verbridge S S, Alden J S, van der Zande A M, Parpia J M, Craighead H G and McEuen P L 2008 Impermeable atomic membranes from graphene sheets *Nano Lett.* **8** 2458–62

[22] Kim K-S, Lee H-J, Lee C, Lee S-K, Jang H, Ahn J-H, Kim J-H and Lee H-J 2011 Chemical vapor deposition-grown graphene: the thinnest solid lubricant *ACS Nano* **5** 5107–14

[23] Berman D, Erdemir A and Sumant A V 2014 Graphene: a new emerging lubricant *Mater. Today* **17** 31–42

[24] Klemenz A, Pastewka L, Balakrishna S G, Caron A, Bennewitz R and Moseler M 2014 Atomic scale mechanisms of friction reduction and wear protection by graphene *Nano Lett.* **14** 7145–52

[25] Filleter T, McChesney J L, Bostwick A, Rotenberg E, Emtsev K V, Seyller Th, Horn K and Bennewitz R 2009 Friction and dissipation in epitaxial graphene films *Phys. Rev. Lett.* **102** 086102

[26] Lee C, Li Q, Kalb W, Liu X-Z, Berger H, Carpick R W and Hone J 2010 Frictional characteristics of atomically thin sheets *Science* **328** 76–80

[27] Lee H, Lee N, Seo Y, Eom J and Lee S W 2009 Comparison of frictional forces on graphene and graphite *Nanotechnology* **20** 325701

[28] Berma D, Erdemir A and Sumant A V 2013 Few layer graphene to reduce wear and friction on sliding steel surfaces *Carbon* **54** 454–9

[29] Lin L Y, Kim D-E, Kim W-K and Jun S-C 2011 Friction and wear characteristics of multi-layer graphene films investigated by atomic force microscopy *Surf. Coat. Tech.* **205** 4864–9

[30] Kirkland N T, Schiller T, Medhekar N and Birbilis N 2012 Exploring graphene as a corrosion protection barrier *Corros. Sci.* **56** 1–4

[31] Kempaiah R, Salgado S, Chung W L and Maheshwari V 2011 Graphene as membrane for encapsulation of yeast cells: protective and electrically conducting *Chem. Commun.* **47** 11480–2

[32] Mohanty N, Fahrenholtz M, Nagaraja A, Boyle D and Berry V 2011 Impermeable graphenic encasement of bacteria *Nano Lett.* **11** 1270–5

[33] Xu K, Cao P and Heath J R 2010 Graphene visualizes the first water adlayers on mica at ambient conditions *Science* **329** 1188–91

[34] Cao P, Xu K, Varghese J O and Heath J R 2011 The microscopic structure of adsorbed water on hydrophobic surfaces under ambient conditions *Nano Lett.* **11** 5581–6

[35] Cao P, Xu K, Varghese J O, Xu K and Heath J R 2012 Visualizing local doping effects of individual water clusters on gold(111)-supported graphene *Nano Lett.* **12** 1459–63

[36] Shim J, Lui C H, Ko T Y, Yu Y-J, Kim P, Heinz T F and Ryu S 2012 Water-gated charge doping of graphene induced by mica substrates *Nano Lett.* **12** 648–54

[37] Severin N, Lange P, Sokolov I M and Rabe J P 2012 Reversible dewetting of a molecularly thin fluid water film in a soft graphene-mica slit pore *Nano Lett.* **12** 774–9

[38] He K T, Wood J D, Doidge G P, Pop E and Lyding J W 2012 Scanning tunneling microscopy study and nanomanipulation of graphene-coated water on mica *Nano Lett.* **12** 2665–72

[39] Komurasaki H, Tsukamoto T, Yamazaki K and Ogino T 2012 Layered structures of interfacial water and their effects on Raman spectra in graphene-on-sapphire systems *J. Phys. Chem.* C **116** 10084–9

[40] Lee M J, Choi J S, Kim J-S, Byun I-S, Lee D H, Ryu S and Lee C 2012 Characteristics and effects of diffused water between graphene and a SiO_2 substrate *Nano Res.* **5** 710–7

[41] Li Q, Song J, Besenbacher F and Dong M 2015 Two-dimensional material confined water *Acc. Chem. Res.* **48** 119–27

[42] Song J, Li Q, Wang X, Li J, Zhang S, Kjems J, Besenbacher F and Dong M 2014 Evidence of Stranski–Krastanov growth at the initial stage of atmospheric water condensation *Nat. Commun.* **5** 4837

[43] Lange P, Dorn M, Severin N, Vanden Bout D A and Rabe J P 2011 Single- and double-layer graphenes as ultrabarriers for fluorescent polymer films *J. Phys. Chem.* C **115** 23057–61

[44] Severin N, Dorn M, Kalachev A and Rabe J P 2011 Replication of single macromolecules with graphene *Nano Lett.* **11** 2436–9

[45] Moon Y, Shin J, Seo S, Park J, Dugasani S R, Woo S H, Park T, Park S H and Ahn J R 2014 Nanoscale topographical replication of graphene architecture by artificial DNA nanostructures *Appl. Phys. Lett.* **104** 231904

[46] Yun J M, Im K N, Kim J Y, Shin D O, Lee W J, Lee S H, Lieberman M and Kim S O 2012 DNA origami nanopatterning on chemically modified graphene *Angew. Chem.* **124** 936–9

[47] Blake P, Hill E W, Castro Neto A H, Novoselov K S, Jiang D, Yang R, Booth T J and Geim A K 2007 Making graphene visible *Appl. Phys. Lett.* **91** 063124

[48] Novoselov K S, Geim A K, Morozov S V, Jiang D, Zhang Y, Dubonos S V, Grigorieva I V and Firsov A A 2004 Electric field effect in atomically thin carbon films *Science* **306** 666–9

[49] Giesbers A J M, Zeitler U, Neubeck S, Freitag F, Novoselov K S and Maan J C 2008 Nanolithography and manipulation of graphene using an atomic force microscope *Solid State Commun.* **147** 366–9

[50] Eilers S and Rabe J P 2009 Manipulation of graphene within a scanning force microscope *Phys. Status Solidi* B **246** 2527–9

[51] Vasić B, Kratzer M, Matković A, Nevosad A, Ralević U, Jovanović D, Ganser C, Teichert C and Gajić R 2013 Atomic force microscopy based manipulation of graphene using dynamic plowing lithography *Nanotechnology* **24** 015303

[52] Song J, Zhang Z, Zhang S, Liu L, Li Q, Xie E, Gothelf K V, Besenbacher F and Dong M 2013 Isothermal hybridization kinetics of DNA assembly of two-dimensional DNA origami *Small* **9** 2954–9

Hybrid Structures for Surface-Enhanced Raman Scattering: DNA Origami/Gold Nanoparticle Dimer/Graphene

Julia Prinz, Aleksandar Matković, Jelena Pešić, Radoš Gajić, and Ilko Bald*

A combination of three innovative materials within one hybrid structure to explore the synergistic interaction of their individual properties is presented. The unique electronic, mechanical, and thermal properties of graphene are combined with the plasmonic properties of gold nanoparticle (AuNP) dimers, which are assembled using DNA origami nanostructures. This novel hybrid structure is characterized by means of correlated atomic force microscopy and surface-enhanced Raman scattering (SERS). It is demonstrated that strong interactions between graphene and AuNPs result in superior SERS performance of the hybrid structure compared to their individual components. This is particularly evident in efficient fluorescence quenching, reduced background, and a decrease of the photobleaching rate up to one order of magnitude. The versatility of DNA origami structures to serve as interface for complex and precise arrangements of nanoparticles and other functional entities provides the basis to further exploit the potential of the here presented DNA origami–AuNP dimer–graphene hybrid structures.

1. Introduction

With the introduction of the DNA origami technique by Paul Rothemund in 2006[1] a versatile tool for the folding of DNA into almost any desired shapes and patterns was created. Initially applied for the fabrication of 2D structures the technique was rapidly extended to construct 3D objects.[2]

J. Prinz, Prof. I. Bald
Institute of Chemistry
University of Potsdam
Karl-Liebknecht-Str. 24-25, 14469 Potsdam, Germany
E-mail: bald@uni-potsdam.de

Dr. A. Matković,[+] J. Pešić, Prof. R. Gajić
Center for Solid State Physics and New Materials
Institute of Physics
University of Belgrade
Pregrevica 118, 11080 Belgrade, Serbia

Prof. I. Bald
BAM Federal Institute for Materials Research and Testing
Richard-Willstätter Str. 11, 12489 Berlin, Germany

[+]Present address: Institute of Physics, Montanuniversität Leoben, Franz Josef Straße 18, A-8700 Leoben, Austria

Due to the addressability of every single DNA staple strand being part of the self-assembly process, functional units, e.g., gold nanoparticles (AuNPs), can be attached to DNA origami templates with nm precision. Such hybrid structures have been used for the study of plasmonic effects[3–6] or surface-enhanced spectroscopies such as fluorescence enhancement[7] or quenching,[8] surface-enhanced Raman scattering (SERS),[9–12] and even for single-molecule SERS.[13]

The basis of surface-enhanced spectroscopy methods is a metal surface—in most cases a metal nanoparticle (NP)—which is brought in close vicinity to the analyte molecule(s). Caused by the excitation of the surface plasmon resonance the electromagnetic field surrounding the NP is enhanced resulting in an increase of the detected signal, that is, fluorescence or Raman scattering. Dimers of AuNPs turned out to be superior over single AuNPs regarding their performances in electromagnetic field enhancements due to hot spot formation.[14,15]

Graphene is a 2D material consisting of sp^2-hybridized carbon atoms which are arranged in a honeycomb lattice. It exhibits a unique combination of electronical, mechanical, and optical properties including high electronic[16] and thermal conductivities,[17] impermeability to any gases,[18] as well as high optical transparency.[19] Although graphene flatly

adsorbs on various substrates, it has been shown to replicate the shape of underlying macromolecules such as double stranded plasmid DNA,[20] 1D five-helix ribbon structures and 2D double-crossover lattices,[21] as well as DNA origami structures[22] very well due to its flexible nature. Recently, it has been reported that the structural stability of triangular DNA origami substrates toward mechanical forces or prolonged exposure to deionized water can be enhanced by graphene encapsulation.[22]

Combining graphene and metal NPs within one hybrid structure is especially advantageous due to the resulting synergy of unique electrical, mechanical, and optical properties introduced by both initial materials. Especially within the fields of biomedicine[23,24] and biosensing[25,26] various types of hybrid materials based on graphene and NPs have been created. Principally, graphene–NP hybrid structures can be obtained either by decorating graphene sheets using metal NPs[27–29] or by wrapping[30,31] or covering[32,33] NPs with graphene. Furthermore, graphene has been reported to remarkably suppress the photobleaching of dye molecules during continuous laser exposure. In shell-isolated SERS experiments using metal nanoparticles encapsulated by few-layer graphene (FLG), the SERS signal intensity of cobalt phthalocyanine (CoP) has been shown to be constant over a time range of 160 s.[30] In another study, Zhao et al. presented R6G molecules being sandwiched between a Ag surface and a monolayer of graphene leading to enhanced photostability of the R6G molecules due to isolation from ambient oxygen.[34]

Here, we introduce a novel kind of multifunctional hybrid material in which the programmability of DNA origami structures, the optical properties of AuNPs, as well as the protective properties of graphene are efficiently merged. The synergistic properties of these hybrid structures are investigated with respect to their SERS performance, polarization dependence of the SERS signal, and photostability of the dyes.

2. Results and Discussion

2.1. Synthesis of DNA Origami–AuNP Dimer–Graphene (AuDG) Hybrid Structures and Atomic Force Microscopy (AFM)-SERS Correlation

An overview of the two-step synthesis of the AuDG hybrid structures is depicted in **Figure 1**a. Initially, triangular DNA origami substrates are folded with a set of 208 staple strands using the genome of the bacteriophage M13mp18 as scaffold. Each DNA origami substrate contains four capture sequences for each AuNP (5′-(AAA)$_8$T$_4$-3′) protruding from opposite sides of the DNA origami triangle. Furthermore, 40 nm AuNPs are coated with dye-modified ssDNA (5′-(TTT)$_4$TX-SH-3′ or 5′-X-(TTT)$_4$T-SH-3′; X = carboxytetramethylrhodamine (TAMRA)). During a DNA hybridization process between the capture strands of the DNA origami substrates and the coating strands of the AuNPs the initial dimeric structures are created. Subsequently, the dimers are adsorbed on Si wafers covered with a layer of 290 nm thick dry thermal oxide (Si/SiO$_2$), which enhances the optical contrast within graphene and therefore allows for its identification.[35] Since the mixture is not further purified after DNA hybridization AuNP dimers coexist with unbound AuNPs. In a second step graphene is deposited on top of the immobilized structures following the classical micromechanical exfoliation process[16] resulting in AuDG hybrid structures.

Subsequent correlation of AFM and SERS images allows for a direct assignment of SERS signals to defined structures which is illustrated in Figure 1b (left: AFM image; right: SERS image). Usually, in AFM images of AuDG
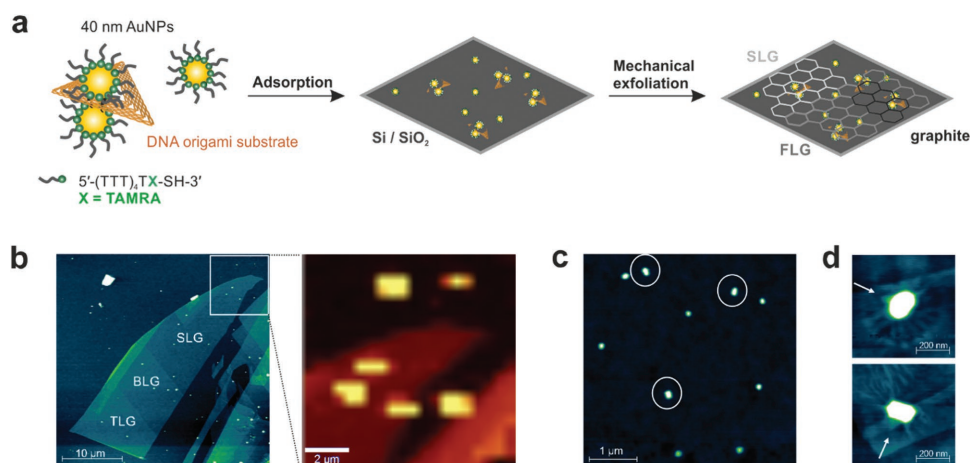
Figure 1. Scheme of sample preparation and correlated AFM-SERS imaging. a) AuNP dimers attached to DNA origami substrates coexisting with single 40 nm TAMRA-modified AuNPs are adsorbed on an Si/SiO$_2$ substrate. In a second step graphene is exfoliated on top of the aforementioned structures by mechanical exfoliation resulting in numerous variations of structures: AuNP dimers can be covered by single-layer graphene (SLG), bilayer graphene (BLG), trilayer graphene (TLG), few-layer graphene (FLG), or graphite. b) Large-size AFM image of one graphene flake exfoliated on top of AuNPs (left) as well as the corresponding Raman map of a selected area (right). c) AFM image of single AuNPs as well as AuNP dimers (marked with white circles) covered by SLG. d) High-resolution AFM images of AuDG hybrid structures with two 40 nm AuNPs attached to one side of the triangle in which a part of the DNA origami triangle is visible (white arrows). The folds of the SLG flake surrounding the hybrid structure are also clearly apparent.

hybrid structures solely the AuNP dimers are visible (Figure 1c, white circles) due to the geometrical arrangement of the AuNPs with respect to the DNA origami substrate preventing the DNA origami from flat adsorption.[13] However, when the two AuNPs are attached to one side of the DNA origami substrate and when the structures are located in close proximity to the edge of the graphene flake the apex of the DNA origami triangle might become visible (Figure 1d, white arrows). Due to the larger gap size between the two AuNPs and the related reduced SERS signal this design of hybrid structure is not further investigated.

2.2. Dye-Modified Single AuNPs Covered by SLG

Basically, the TAMRA modification might be introduced at any position within the DNA coating strands of the AuNPs. Upon covering the structures with SLG some TAMRA molecules surrounding the AuNPs are sandwiched in between the Au surface and the graphene layer. Since both materials are known to influence the optical properties of dye molecules such as fluorescence[7,8,36] and Raman scattering[37,38] it is crucial to investigate the SERS performance of individual structures in dependence of the relative dye position. To disentangle additional effects due to hot spot formation within dimeric structures, also very basic SERS experiments on differently designed single 40 nm AuNPs are performed.

In the first case, the TAMRA dye is positioned in close vicinity to the AuNP surface using the 5′-(TTT)$_4$TX-SH-3′ (X = TAMRA) sequence as coating strands (**Figure 2**a). The same type of AuNPs is studied with SLG on top (Figure 2b). In the second case, the TAMRA dye is positioned further away from the AuNP surface by coating the particles with the 5′-X-(TTT)$_4$T-SH-3′ sequence and thereby introducing a DNA spacer of 13 bases between dye and Au surface. In order to reduce the concentration of TAMRA molecules per particle, coating strands without dye are introduced (Figure 2c). Again, the same type of AuNPs covered by SLG is studied (Figure 2d). In all cases SERS measurements on single AuNPs are accompanied by AFM measurements in order to confirm the origin of each signal. In every SERS series (Figure 2a–d) the characteristic TAMRA bands[13] are marked with a green star whereby the peaks at ≈1361 and 1654 cm^{-1} are visible in all spectra and additional peaks at 1222, 1509, 1538, and 1570 cm^{-1} only appear in some cases. For AuNPs coated by DNA with TAMRA at the 5′-end (Figure 2c,d) a slight red-shift of 4 cm^{-1} for the two most prominent TAMRA bands is observed resulting in spectral
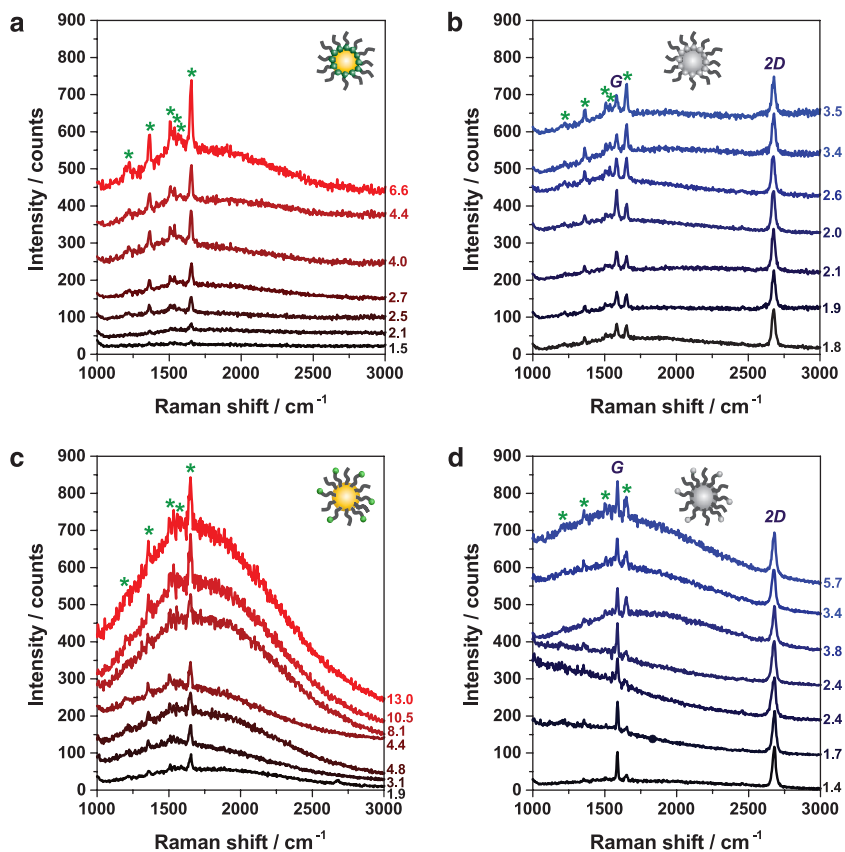

Figure 2. SERS spectra of differently functionalized AuNPs. Comparison of SERS spectra arising from several different single 40 nm AuNPs coated with TAMRA-modified ssDNA. a,b) In these cases the TAMRA dye is located close to the AuNP surface (5′-(TTT)$_4$TX-SH-3′ (X = TAMRA)), whereas c,d) in these cases dye and AuNP surface are separated by 13 DNA bases (5′-X-(TTT)$_4$T-SH-3′ (X = TAMRA)). Additionally, AuNPs in (b) and (d) are covered by SLG. The characteristic TAMRA bands (green stars) as well as the typical G and 2D bands of SLG are marked. Laser wavelength: 532 nm, laser power: 80 µW, integration time: 10 s. Recorded noise data are given in counts.

positions of 1357 and 1650 cm^{-1}, which is attributed to distance-dependent interactions between the dye molecules and the gold surface. Upon graphene encapsulation no further shift of the spectral positions of the TAMRA bands is noticed.

Furthermore, in the two cases with SLG (Figure 2b,d) the two characteristic bands arising from graphene (G band (1586 cm^{-1}) and 2D band (2680 cm^{-1})) are highlighted. Both bands are highly sensitive to doping[39–41] and strain[42–44] which can cause peak shifts of several cm^{-1} even for pristine graphene without underlying AuNPs. Therefore, the slight variations in peak positions for the G and the 2D band which can be observed over the whole area of the graphene flake cannot be directly correlated to doping or strain caused by the AuNPs. For all SERS spectra of each series the noise within the spectral range of 1800–2200 cm^{-1} is determined and stated next to each spectrum (in units of counts, Figure 2a–d).

Comparing the two cases without SLG (Figure 2a,c) it is obvious that the fluorescence background due to the resonant excitation of the TAMRA molecules (λ_{em} = 582 nm ≙ 1610 cm^{-1}) is more pronounced when the dyes are located at the 5′-end and thereby separated from

the AuNP surface (Figure 2c). This is in good agreement with the known distance dependence of fluorescence enhancement[7] and fluorescence quenching.[8] In both cases without graphene a broad distribution of SERS intensities can be observed which is attributed to slight variations in AuNP sizes, numbers of TAMRA molecules per particle, as well as different photobleaching rates for individual AuNPs. The absolute SERS intensities obtained from AuNPs coated by DNA with TAMRA at the 3′-end or 5′-end cannot directly be compared since in the latter case a mixture of dye-modified and non-modified sequences was used as coating strands. However, both the noise averaged over all spectra and the maximum noise among all spectra are higher in the case of TAMRA being at the 5′-end (average: 6.5 counts; maximum: 13.0 counts) (Figure 2c) compared to TAMRA at the 3′-end (average: 3.4 counts; maximum: 6.6 counts) (Figure 2a).

For both types of AuNPs (with TAMRA being close to the AuNP surface (Figure 2a) or further apart from it and thus closer to graphene (Figure 2c)) the appearance of the SERS spectra is dramatically influenced by graphene encapsulation (Figure 2b,d). In the case of TAMRA being at the 3′-end (Figure 2b) the fluorescence background appears to be efficiently quenched resulting in a cleaner baseline compared to the analogue non-covered AuNPs (Figure 2a). The function of graphene as a potential quencher of fluorescence from dye (R6G) molecules was first described by Xie et al.[36] and afterward also confirmed for the photoluminescence arising from a gold surface.[45] In the first case the quenching process was postulated to be caused by a resonance energy transfer from dyes to graphene enabled by considerable π–π interactions.[36,46] However, within the here presented structures direct π–π interactions between the TAMRA molecules and the graphene layer may not occur since both are separated by the DNA coating whose thickness is estimated to be 2.5 nm.[10] Nevertheless, a remarkable quenching of the fluorescence background is observed. Although the nature of this effect is not resolved here, two possible explanations might be considered. On the one hand, based on the distance between TAMRA molecules and graphene an energy transfer from excited dye molecules to SLG is conceivable. Typical energy transfer processes such as Förster resonance energy transfer (FRET) can be observed for distances between 1 and 10 nm[47] which is in good agreement with the here considered system. On the other hand, it cannot be excluded that a DNA-mediated charge transfer mechanism from the AuNPs to SLG is involved in the fluorescence quenching process similar to observations by Fritzsche and co-workers.[48,49] They found that the excitation of a silver nanoparticle can be transferred via a dsDNA nanowire over a distance of several micrometers resulting in photobleaching of intercalating dyes. In the case of the here presented structures, also a combination of both, energy transfer and charge transfer, is conceivable.

Compared to their non-covered analogues the values for the average noise and the maximum noise are reduced for both, TAMRA located at the 3′-end (average: 2.6 counts; maximum: 3.5 counts; Figure 2b) as well as at the 5′-end (average: 3.0 counts, maximum: 5.7 counts; Figure 2d). Furthermore, the distribution of SERS intensities arising from

the TAMRA signals is much narrower compared to the three other cases (Figure 2a,c,d).

The aforementioned π–π interactions responsible for an effective resonance energy transfer between dye molecules and graphene should be enabled if the TAMRA modification is located at the 5′-end of the AuNP coating strands. Interestingly, the SERS spectra arising from those types of structures seem to be categorized in two classes (Figure 2d). On the one hand, the three upper SERS spectra clearly display the characteristic fluorescence background of TAMRA with a maximum at ≈1610 cm^{-1}. However, the different appearance of the backgrounds in the following three spectra can be assigned to the typical photoluminescence background characteristic for AuNPs with diameters less than 150 nm.[27] The occurring differences are most probably due to a different extent of contact between SLG and the underlying AuNPs. Although at least some of the TAMRA molecules get in direct contact to the SLG their fluorescence is not significantly quenched in the case of the upper three spectra. For the following three AuNPs the interactions between graphene and the TAMRA molecules are more pronounced resulting in efficient fluorescence quenching and a remaining background whose appearance is defined by the photoluminescence of the AuNPs. This type of luminescence in turn is not quenched due to an insufficient contact between the AuNPs and SLG. Phase AFM images of all AuNPs corresponding to the SERS spectra presented in Figure 2b are shown in Figure S1 (Supporting Information). Additionally, analogue measurements are performed using cyanine 3 (Cy3) as Raman reporter molecule instead of TAMRA (see Figure S2, Supporting Information).

In summary, these experiments show that the best reproducible TAMRA signals as well as the cleanest baselines are obtained under two conditions: (a) the TAMRA molecules have to be located in close proximity to the AuNP surface in order to experience efficient fluorescence quenching and (b) the dye-modified AuNPs have to be covered by SLG to benefit from an additional fluorescence quenching, a reduced noise level, as well as a narrow distribution of TAMRA signal intensities. As a consequence, the following discussions are based on AuDG hybrid structures containing AuNPs with TAMRA at the 3′-end.

2.3. Comparison of AuNP Dimers and AuDG Hybrid Structures

In the next step AuNP dimers attached to one DNA origami substrate are investigated. In **Figure 3**a typical Raman maps of a surface area covered by different types of graphene (SLG, FLG, and graphite) are presented. The four maps exhibit the SERS intensity distributions of the four most important bands arising from AuNP dimers/AuDG hybrid structures, that is, (i) the G band (1586 cm^{-1}), (ii) the 2D band (2670 cm^{-1}), (iii) the TAMRA band at 1361 cm^{-1}, and (iv) the TAMRA band at 1654 cm^{-1}. It has to be mentioned that the TAMRA band at 1361 cm^{-1} can be spectrally overlapped by the D band of graphene at 1338 cm^{-1}. For this reason Raman map (iii) exhibits the SERS intensity distribution of both peaks. Especially Raman map (iv) shows that there
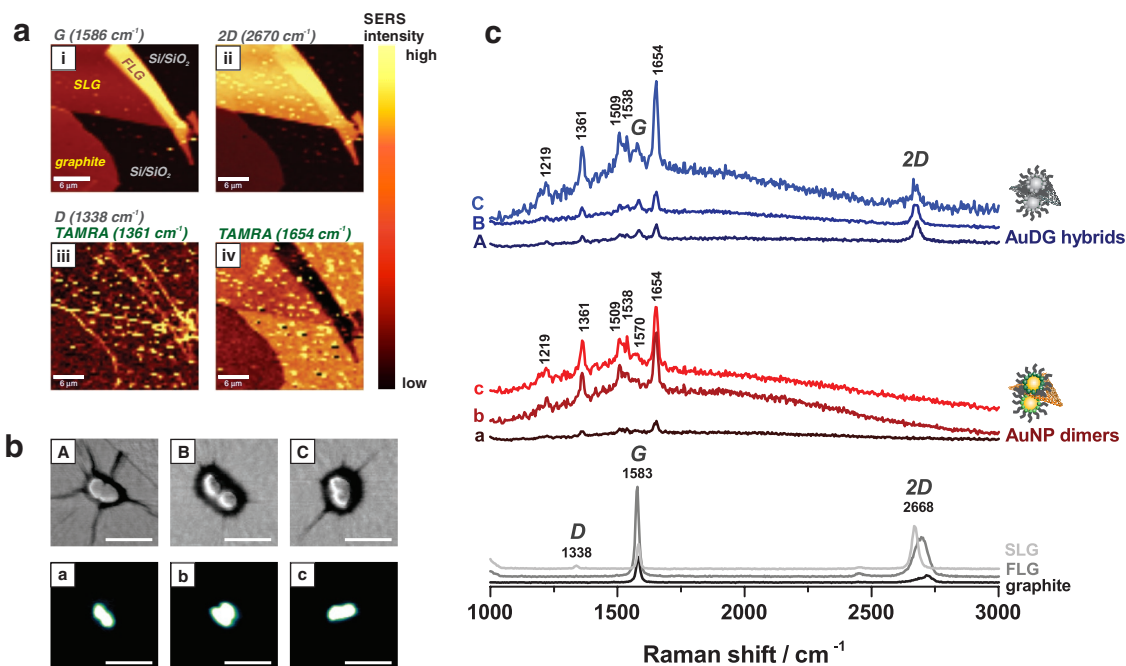
Figure 3. AFM–SERS correlation of AuNP dimers and AuDG hybrid structures. a) Raman maps visualizing the SERS intensity distribution of the G band at 1586 cm^{-1} (i), the 2D band at 2670 cm^{-1} (ii), the D band at 1338 cm^{-1} (spectral overlap with the TAMRA band at 1361 cm^{-1}) (iii), and the most characteristic TAMRA band at 1654 cm^{-1} (iv). b) AFM images of three AuDG hybrid structures (first row; phase images) and three AuNP dimers (second row; topography images). Scale bars: 200 nm. c) Typical SERS spectra of SLG, FLG, and graphite (gray and black spectra). Extended SERS spectra including the 2D' band at 3245 cm^{-1} which has not been used for any analysis is shown in Figure S3 (Supporting Information). Additionally, SERS spectra of the AuNP dimers (red spectra) and the hybrid structures (blue spectra) originating from the structures shown in (b) are presented. Laser wavelength: 532 nm, laser power: 80 µW, integration time: 10 s.

are three different types of AuNP dimers: some covered by SLG, some covered by FLG, and also non-covered structures. In Figure 3b phase AFM images of representative AuDG hybrid structures (A, B, C; first row) as well as topography AFM images of non-covered AuNP dimers (a, b, c; second row) are shown. In the case of the AuDG hybrid structures it is obvious that the graphene layer covering the hybrid structures is differently folded and therefore the extent of contact between AuNPs and SLG differs for each individual structure. For hybrid A several folds within the graphene layer can be observed as a result of AuNP replication. This is not the case for hybrid B, and for hybrid C only a few folds are visible. In Figure 3c correlated SERS spectra arising from the AuNP dimers (red spectra) and the AuDG hybrid structures (blue spectra) shown in the AFM images in Figure 3b are presented. Additionally, for comparison typical SERS spectra obtained from SLG, FLG, and graphite are shown in gray and black. A comparison of SERS spectra from AuNP dimers and AuDG hybrid structures reveals that in both cases the characteristic TAMRA bands[13] at 1219, 1361, 1509, 1538, 1570 (superimposed by the G band for hybrids; blue spectra), and 1654 cm^{-1} can be detected which coincide with the recorded bands for the single AuNPs (Figure 2b,d). Furthermore, the SERS spectra of AuDG hybrid structures (blue spectra) also show the two most characteristic graphene bands at 1586 cm^{-1} (G band) and at 2670 cm^{-1} (2D band) whose spectral positions are in good agreement with the ones detected for SLG (light gray spectrum). For both types of structures (AuNP dimers/AuDG hybrids) the overall SERS intensity

differs for individual structures, which is caused by slight differences in AuNP and gap sizes.

2.4. Polarization-Dependent SERS Measurements on AuDG Hybrid Structures

To test the extent of contact between SLG and underlying AuNP dimers which is related to induced strain within graphene, polarization-dependent SERS measurements are performed. In **Figure 4** the obtained results for one representative AuDG hybrid are presented. Figure 4a shows two AFM images (left: topography; right: phase) of the investigated structure clearly exhibiting the folds within the covering SLG flake. In the right image the extension of folds is marked by yellow dashed lines and the position of the dimer axis (0°) relative to the angle of polarization is shown. SERS measurements are performed by using polarized laser light for excitation (parallel to the dimer axis; 0°; λ = 532 nm) and by changing the angle of the detection plane in steps of 15° for each measurement starting with +90°. In Figure 4b the corresponding SERS spectra for different polarization angles are presented. Both, TAMRA signals (green stars) as well as SLG signals (G and 2D band) arising from the AuDG hybrid structure in Figure 4a are polarization-dependent.

On the one hand, highest intensities for the TAMRA signals are detected for the polarization angle parallel to the axis of the AuNP dimer due to the optimal geometry for plasmon coupling of the two individual AuNPs.[14] Moving
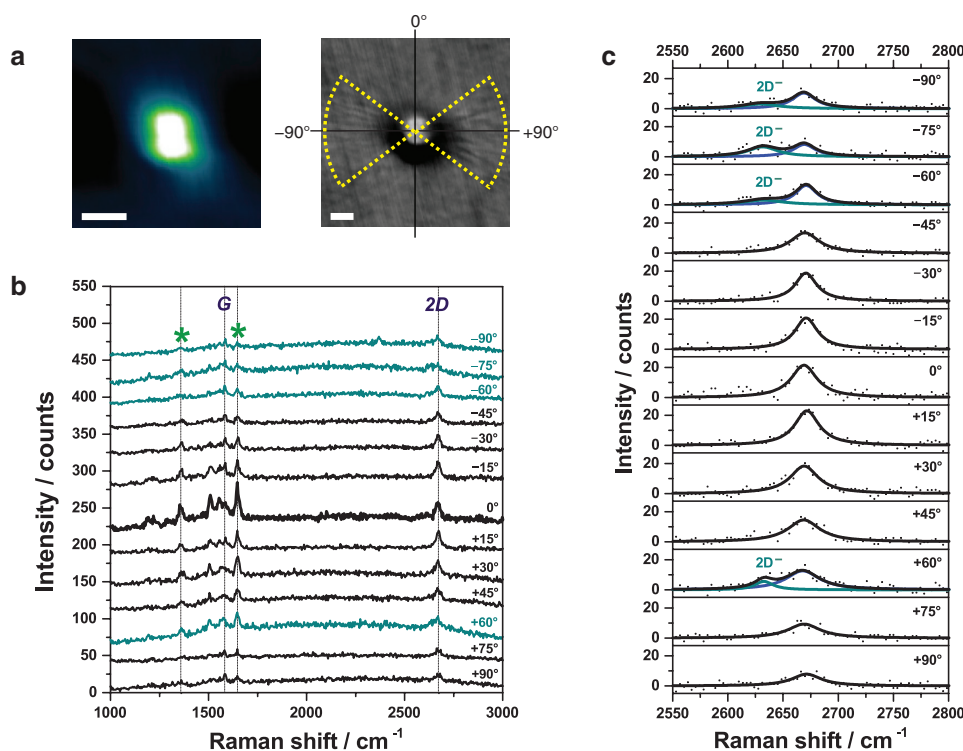
Figure 4. Polarization-dependent SERS measurements of one individual AuDG hybrid structure. a) AFM images (left: topography; right: phase) of one representative AuDG hybrid structure for which polarization-dependent SERS measurements are performed. Scale bars: 100 nm. b) SERS spectra obtained for different polarization angles in steps of 15°. The most characteristic bands for TAMRA (green stars) and SLG (G and 2D band) are highlighted. c) Lorentzian fit curves for the 2D band in dependence of the polarization angle. A splitting of the 2D band is observed for polarization angles of +60°, −60°, −75°, and −90°.

away from this optimal polarization angle for plasmon coupling toward −90°/+90° leads to a decrease of the TAMRA signal intensities. The remaining signal is due to the detection of scattered light, which is not or only to a small extent affected by plasmon coupling of the two individual AuNPs.

On the other hand, in the case of SLG a polarization-dependence of the 2D band at ≈2670 cm^{-1} can be observed. This is clarified in Figure 4c where Lorentzian fit curves for the 2D band under different polarization angles are presented. Nine of the 13 different SERS spectra can be described by a single Lorentzian function with a maximum at around 2670 cm^{-1} (+90°, +75°, +45°, +30°, +15°, 0°, −15°, −30°, −45°). However, in the case of polarization angles of +60°, −60°, −75°, and −90° a second peak at ≈2630 cm^{-1} arises resulting in fit curves consisting of two Lorentzian functions (blue and cyan bands in Figure 4c). From previous reports it is known that the G band[44,50] as well as the 2D band[43] in SLG can split in two components upon uniaxial strain. However, under the currently applied conditions the G band at 1586 cm^{-1} is not clearly resolved due to low laser intensities and arising luminescence from the TAMRA dyes, especially for polarization along the axis of the dimer. Therefore, the following considerations concerning strain-induced observations are only based on the 2D band. Generally, splitting of the 2D band is induced by a change in symmetry of the graphene lattice upon uniaxial strain.[43] As a consequence, the Dirac cone—representing a scheme of the electronic dispersion—is displaced from its original position resulting in altered interactions with its three nearest neighbors. This

should result in the appearance of three contributions to the 2D band, however, the third peak is usually difficult to observe.[43]

In the case of the AuDG hybrid structure in Figure 4a a clear correlation between the direction of folds surrounding the underlying AuNP dimer (yellow dashed lines in Figure 4a, right) and the polarization-dependent SERS signal is observed. The relative orientation of the polarization angles for which a splitting of the 2D band appears (Figure 4c; +60°, −60°, −75°, and −90°) to the AuNP dimer is in excellent agreement with the direction of folds and therefore with the direction of uniaxial strain.

It has to be mentioned that the laser spot size (≈1.3 µm in diameter) is much larger compared to the size of the AuDG hybrid structure. The detected SERS signals arising from SLG therefore contain information about several influences such as folding, doping,[39–41] or strain[42–44] summed up over the graphene area irradiated by the laser. Therefore, the main proportion of the band at 2670 cm^{-1} is arising from the area of SLG which is surrounding the AuDG hybrid structure and therefore only weakly influenced by the induced strain. The 2D$^+$ mode which is expected to appear red-shifted upon uniaxial strain is most probably superimposed by the band at 2670 cm^{-1}. Nevertheless, confirmed by the appearance of the 2D$^-$ band at 2630 cm^{-1} the strain caused by the underlying AuNP dimer is obviously high enough to induce a mode splitting of the 2D band which is on the order of ≈40 cm^{-1}. Based on results obtained by applying controlled strain to SLG[43] we estimate that the underlying structure in Figure 4a

induces an uniaxial strain component within the covering SLG of about 1%–2%.

2.5. Suppression of Photobleaching due to SLG

Photobleaching is an undesired side effect which often accompanies SERS measurements. It arises from irreversible decomposition of the analyte molecules caused by photochemical reactions.[51] Under the here applied conditions we expect heating effects[52] as well as reactions with ambient oxygen[53,54] to be the two main sources for damages of the dye molecules.

In order to investigate the potential of graphene in terms of suppressing the photobleaching of the TAMRA dyes SERS time series measurements under continuous laser exposure for 800 s are performed for individual AuNP dimers and AuDG hybrid structures (**Figure 5**). Therefore, SERS spectra are recorded in time intervals of 10 s and for every spectrum the signal-to-noise (S/N) ratio for the most intense TAMRA band at 1654 cm^{-1} is calculated (the noise level is determined within the spectral range of 1800–2200 cm^{-1} of each spectrum). As can be seen in Figure 5a the S/N ratio is continuously decreasing for all three AuNP dimers with increasing laser exposure time. Since the amount of the aforementioned processes resulting in damages of the TAMRA molecules differ for each individual structure different photobleaching rates are obtained for dimers i–iii (inset of Figure 5a). More precisely, for dimers i (black data) and ii (dark red data) photobleaching rates (with regards to the S/N ratios) of 3.6×10^{-2} and 1.7×10^{-2} s^{-1} are determined. On the contrary, the S/N ratio arising from dimer iii (light red

data) is decreasing following two different photobleaching rates: 4.7×10^{-2} s^{-1} within the first 250 s of laser exposure and 1.0×10^{-2} s^{-1} within the subsequent time interval. In Figure 5b the time evolution of the associated SERS spectra for the three investigated AuNP dimers are shown (the two most characteristic TAMRA bands are marked with a green star). The SERS spectra are presented in time intervals of 50 s starting with 10 s and ending with 800 s of laser exposure. Again, the first spectrum of each dimer recorded after 10 s of integration exhibits different overall SERS intensities, which is consistent with the aforementioned diversity for individual structures. In all three SERS time series measurements a significant photobleaching during laser exposure for 800 s can be observed. Interestingly, not only the SERS intensities of the TAMRA bands but also the noise level is reduced over time for all AuNP dimers, confirming the correlation between high SERS intensities and high noise levels (see Figure S4, Supporting Information for independent time evolutions of the signal and the noise level).

In contrast to the AuNP dimers a different photobleaching behavior is observed for the AuDG hybrid structures (Figure 5c,d). For hybrid I and II (Figure 5c, black and light blue data) the photobleaching rate of the S/N ratio is nearly identical (5.9×10^{-3} and 4.2×10^{-3} s^{-1}). Thus, compared to the non-covered dimers (Figure 5a,b) the photobleaching rate is reduced by approximately one order of magnitude.

In the case of AuDG hybrid I (black data) the time evolution of the SERS signal (Figure S4c, Supporting Information) can be divided in two parts: (1) an initial rapid decrease of the TAMRA band at 1654 cm^{-1} within the first 60 s of laser exposure and (2) in between the time interval of 60 and 800 s the decrease of signal intensity is significantly slowed down.
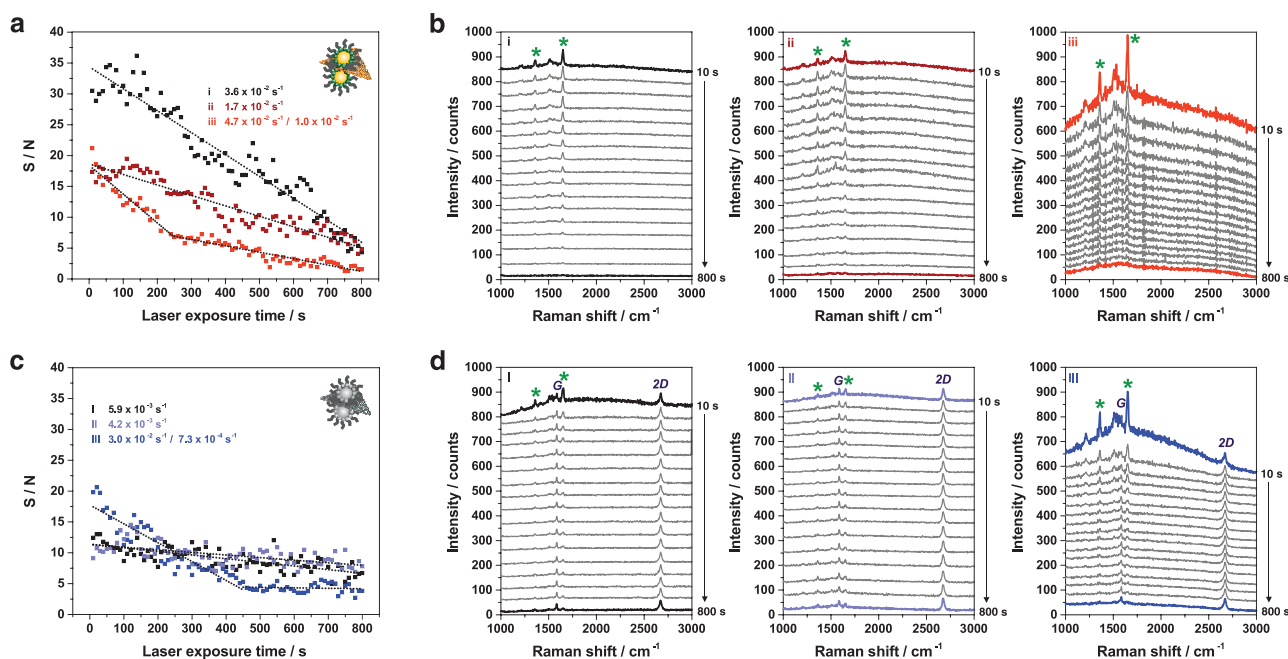

Figure 5. Photobleaching behavior of AuNP dimers and AuDG hybrid structures. Time series SERS measurements of a,b) individual non-covered AuNP dimers as well as of c,d) AuDG hybrid structures. SERS spectra are recorded in time intervals of 10 s using 532 nm laser excitation, a laser power of 25 µW, and integration times of 10 s. The temporal evolution of the S/N ratio of the TAMRA band at 1654 cm^{-1} is presented as a function of continuous laser exposure for three AuNP dimers (a) as well as for three AuDG hybrid structures (c). The corresponding SERS spectra recorded during 800 s of laser exposure are presented in steps of 50 s exposure time for AuNP dimers (b) and AuDG hybrid structures (d).

This behavior is attributed to different extents of interactions between the TAMRA molecules and the graphene layer. During the first 60 s of laser exposure the observed photobleaching is probably caused by those TAMRA dyes which are not or only weakly interacting with the SLG. Subsequently, the signal is more stable since the remaining intact TAMRA dyes efficiently interact with the SLG. On the contrary, after a slow decrease within the first 200 s the SERS signal of AuDG hybrid II (Figure S4c, Supporting Information, light blue data) stays constant until the end of the laser exposure confirming that SLG can provide extensive protection against photobleaching if the dye molecules interact strongly with the graphene layer. A damage of the SLG upon laser exposure can be excluded since no Raman modes characteristic for graphene damage such as D band (1338 cm^{-1}), D' band ($\approx$1620 cm^{-1}),[55] or the combination band D+D' ($\approx$2940 cm^{-1})[55] are observed.

However, AuDG hybrid III (blue data in Figure 5c,d) also exhibits a time evolution of the TAMRA signal which can be divided in two different parts, similar to the non-covered dimer iii (light red data in Figure 5a,b). The initial time interval (0–450 s of laser exposure) is defined by a rapid decrease of the S/N ratio with a photobleaching rate of 3.0×10^{-2} s^{-1} which is of the same order as for AuNP dimers. Subsequently, the rate is dramatically reduced to 7.3×10^{-4} s^{-1} within the time interval between 450 and 800 s of laser exposure.

The fact that for some structures two successive photobleaching rates can be determined allows for the assumption that the observed decrease in SERS signal intensity is based on at least two different contributions. This is also confirmed by the time evolutions of the corresponding noise levels (Figure S4b,d, Supporting Information) and attributed to (a) heating effects caused by the laser exposure which should be especially pronounced within the hot spot[52,56] and (b) reactions with ambient oxygen. In the cases of AuNP dimers both should significantly contribute to the total photobleaching rate. However, for AuDG hybrid structures the SLG is expected to have an effect on both contributions for two reasons: (1) Since SLG has been demonstrated to be impermeable to any kind of gases[18] the reaction with ambient oxygen can be excluded as possible photobleaching mechanism. (2) Graphene is known to be an excellent heat conductor exhibiting values of $\approx$5 × 10^3 W mK^{-1}.[17] Thus, the plasmonically generated heat can be dissipated by the graphene.

The stronger the coupling of the surface plasmon resonances of the two individual AuNPs within a dimer the higher is the resulting electromagnetic field enhancement and thus the expected heating.[52] This postulation is in good agreement with the experimentally observed behavior for different structures. In the case of AuNP dimers (Figure 5a,b) the highest initial SERS signal has been recorded for dimer iii (light red data) which is attributed to a hot spot providing the highest field enhancements among the three investigated structures (i–iii). As a consequence, the initial photobleaching is more significant compared to the other two AuNP dimers (black and red data) due to higher heat induced damage.

A similar behavior is observed for AuDG hybrid structure III (Figure 5c,d; Figure S4c,d, Supporting Information; blue data). In this case the contact between SLG and the underlying AuNPs is probably not strong enough to enable efficient heat conduction. On the contrary, AuDG hybrid II exhibits a relatively low initial SERS signal correlated with a low noise level which both remain constant over the whole period of 800 s (Figure 5c,d; Figure S4c,d, Supporting Information; light blue data). This is caused by a less pronounced electromagnetic field enhancement within the hot spot resulting in lower heating effects.

3. Conclusion

In summary, the synthesis of novel AuDG hybrid structures is reported and their optical properties with regard to SERS are carefully characterized. We find that AuNPs and graphene have a competing influence on the appearance of the fluorescence background obtained by sandwiched dye molecules. Moreover, a deeper understanding of the hybrid material is gained by polarization-dependent SERS measurements which allows for precise correlation of visible disorder within the graphene layer and spectral mode splitting of the 2D band. Furthermore, an improved photostability due to graphene encapsulation resulting in significantly lower photobleaching rates is clearly demonstrated. This is attributed to the efficient protection of the dye molecules from reactions with ambient oxygen by graphene and heat dissipation from the SERS hot spots.

The novel AuDG hybrid structures combine unique properties of three different building blocks within one material. Since every component can be independently tuned, hybrid structures represent a multifunctional tool in fields such as biosensing and bioelectronics. In this context, the addressability of the system introduced by the DNA origami template is highly beneficial since it allows for the precise arrangement of nanoparticles and other functional entities such as dyes, conducting polymers,[57] etc. On the other hand, the structures might be suitable for promoting investigations in the field of graphene-enhanced Raman scattering (GERS)[37,58] and correlated mechanisms. The main profit in this context is the possibility of using the DNA origami substrate as mediator in order to precisely tune the interaction between NPs and graphene.

4. Experimental Section

Preparation of AuDG Hybrid Structures: DNA origami structures, DNA-coated AuNPs, as well as AuNP dimers were prepared following a previously published procedure.[13] The synthesis of DNA origami structures is based on the M13mp18 virus strand (New England Biolabs) used as scaffold which is folded to triangular shape by the addition of 208 short ssDNA staple strands.[1] Eight staple strands (t-1s6e, t1s6i, t-1s8g, t1s8i and t-2s5f, t-2s7f, t2s5f, t2s7f) were extended at the 5′-end by the capture sequence 5′-(AAA)$_8$T$_4$-3′ in order to realize the attachment of two AuNPs per DNA origami substrate. Extended ssDNA strands were purchased

from metabion, non-extended from Integrated DNA Technologies. Citrate-capped 40 nm AuNPs from BBI solutions were coated with two different types of TAMRA-modified ssDNA (5′-(TTT)$_4$ TX-SH-3′ or 5′-X-(TTT)$_4$ T-SH-3′; X = TAMRA) or Cy3-modified ssDNA (5′-(ATT)$_3$-T$_4$X-SH-3′; X = Cy3) (Metabion) similar to the protocol of Ding et al.[59] using adjusted concentrations, reaction times, and 0.02% sodium dodecyl sulfate (SDS, Sigma Aldrich). DNA-coated AuNPs were attached to DNA origami substrates via DNA hybridization. Therefore, a temperature program was applied to a mixture of DNA origami structures and AuNPs (ratio 1:1). After hybridization the solution was used without further purification resulting in a coexistence of AuNP dimers and unbound AuNPs.

Preparation of Si Substrates: Si wafers covered with 290 nm thick dry thermal oxide (SiO$_2$/Si) (IDB Technologies Ltd.) were cleaned with acetone (absolute), heated to 250 °C for 10 min, and finally cleaned using an ozone cleaner (Diener electronic, ZEPTO) for 10 min. Immediately after ozone cleaning the AuNP dimers (coexisting with unbound AuNPs) were immobilized by transferring a 0.5−1.0 μL drop of the hybridization solution to the Si substrate and adding 40 μL of 10× TAE with 100 × 10^{-3} M MgCl$_2$. After an incubation time of 60 min Si wafers were rinsed with ethanol (absolute)/Millipore water (1:1) and dried with compressed air.

Mechanical Exfoliation of Graphene: Graphene was deposited by the well-established process of micromechanical cleavage.[16] Flakes of Kish graphite (Naturgraphite GmbH) were repeatedly cleaved using sticky tape (Nitto Denko ELP BT150ECM) and afterward deposited on top of the AuNP dimers immobilized on Si substrates. As-prepared Si wafers were stored in methyl isobutyl ketone (MIBK, Sigma Aldrich) at room temperature for ≈ 3 h. After removal of the sticky tape, wafers were washed with MIBK and 2-propanole and dried with compressed air. Finally, exfoliated flakes were cleaved another time using sticky tape and flakes of SLG were identified using an optical microscope.

AFM Imaging: AFM images were recorded in tapping mode with a Nanosurf FlexAFM using Tap150Al-G cantilevers (force constant 5 N m^{-1}) (Budget Sensors). For analysis of AFM images the software Gwyddion 2.34 (freeware) was used.

Raman Imaging: For SERS measurements a confocal Raman microscope (WITec alpha300) with an upright optical microscope was used. The 532 nm excitation laser was coupled into a single-mode optical fiber and focused to a diffraction-limited point (1.3 μm^2) on the sample by passing a 100× objective (Olympus MPlanFL N, NA = 0.9). Raman images in Figure 3a were performed using a laser power of 900−1000 μW and an integration time of 2 s. The SERS spectra of SLG, FLG, and graphite (Figure 3c) were extracted from these Raman images. Further Raman images (including the image in Figure 1b) were recorded with a laser power of 80 μW and an integration time of 10 s, and the SERS spectra a-c and A-C in Figure 3c as well as the spectra in Figure 2 were extracted from these Raman images. All other SERS spectra were obtained by recording single spectra on predefined positions. The laser power was further decreased to 25 μW for polarization-dependent measurements (Figure 4) and time series measurements (Figure 5). Before the beginning of the polarization series (Figure 4) it was ensured that the SERS signal stayed constant over three unpolarized measurements. In all cases, the grating of the spectrograph was set to 600 g mm^{-1}. SERS spectra were vertically shifted for better visualization.

Supporting Information

Supporting Information is available from the Wiley Online Library or from the author.

Acknowledgements

[1] P. W. K. Rothemund, *Nature* **2006**, *440*, 297.
[2] S. M. Douglas, H. Dietz, T. Liedl, B. Hogberg, F. Graf, W. M. Shih, *Nature* **2009**, *459*, 414.
[3] X. Shen, A. Asenjo-Garcia, Q. Liu, Q. Jiang, F. J. G. de Abajo, N. Liu, B. Ding, *Nano Lett.* **2013**, *13*, 2128.
[4] C. Zhou, X. Duan, N. Liu, *Nat. Commun.* **2015**, *6*, 8102.
[5] A. Kuzyk, R. Schreiber, Z. Fan, G. Pardatscher, E.-M. Roller, A. Hogele, F. C. Simmel, A. O. Govorov, T. Liedl, *Nature* **2012**, *483*, 311.
[6] T. Schlichthaerle, M. T. Strauss, F. Schueder, J. B. Woehrstein, R. Jungmann, *Curr. Opin. Biotechnol.* **2016**, *39*, 41.
[7] G. P. Acuna, F. M. Möller, P. Holzmeister, S. Beater, B. Lalkens, P. Tinnefeld, *Science* **2012**, *338*, 506.
[8] G. P. Acuna, M. Bucher, I. H. Stein, C. Steinhauer, A. Kuzyk, P. Holzmeister, R. Schreiber, A. Moroz, F. D. Stefani, T. Liedl, F. C. Simmel, P. Tinnefeld, *ACS Nano* **2012**, *6*, 3189.
[9] J. Prinz, B. Schreiber, L. Olejko, J. Oertel, J. Rackwitz, A. Keller, I. Bald, *J. Phys. Chem. Lett.* **2013**, *4*, 4140.
[10] V. V. Thacker, L. O. Herrmann, D. O. Sigle, T. Zhang, T. Liedl, J. J. Baumberg, U. F. Keyser, *Nat. Commun.* **2014**, *5*, 3448.
[11] M. Pilo-Pais, A. Watson, S. Demers, T. H. LaBean, G. Finkelstein, *Nano Lett.* **2014**, *14*, 2099.
[12] P. Kühler, E.-M. Roller, R. Schreiber, T. Liedl, T. Lohmüller, J. Feldmann, *Nano Lett.* **2014**, *14*, 2914.
[13] J. Prinz, C. Heck, L. Ellerik, V. Merk, I. Bald, *Nanoscale* **2016**, *8*, 5612.
[14] C. E. Talley, J. B. Jackson, C. Oubre, N. K. Grady, C. W. Hollars, S. M. Lane, T. R. Huser, P. Nordlander, N. J. Halas, *Nano Lett.* **2005**, *5*, 1569.
[15] K. L. Wustholz, A.-I. Henry, J. M. McMahon, R. G. Freeman, N. Valley, M. E. Piotti, M. J. Natan, G. C. Schatz, R. P. Van Duyne, *J. Am. Chem. Soc.* **2010**, *132*, 10903.
[16] K. S. Novoselov, A. K. Geim, S. V. Morozov, D. Jiang, Y. Zhang, S. V. Dubonos, I. V. Grigorieva, A. A. Firsov, *Science* **2004**, *306*, 666.
[17] A. A. Balandin, S. Ghosh, W. Bao, I. Calizo, D. Teweldebrhan, F. Miao, C. N. Lau, *Nano Lett.* **2008**, *8*, 902.
[18] J. S. Bunch, S. S. Verbridge, J. S. Alden, A. M. van der Zande, J. M. Parpia, H. G. Craighead, P. L. McEuen, *Nano Lett.* **2008**, *8*, 2458.
[19] R. R. Nair, P. Blake, A. N. Grigorenko, K. S. Novoselov, T. J. Booth, T. Stauber, N. M. R. Peres, A. K. Geim, *Science* **2008**, *320*, 1308.

[20] N. Severin, M. Dorn, A. Kalachev, J. P. Rabe, *Nano Lett.* **2011**, *11*, 2436.

[21] Y. Moon, J. Shin, S. Seo, J. Park, S. R. Dugasani, S. H. Woo, T. Park, S. H. Park, J. R. Ahn, *Appl. Phys. Lett.* **2014**, *104*, 231904.

[22] A. Matković, B. Vasić, J. Pešić, J. Prinz, I. Bald, A. R. Milosavljević, R. Gajić, *New J. Phys.* **2016**, *18*, 25016.

[23] X. Ma, Q. Qu, Y. Zhao, Z. Luo, Y. Zhao, K. W. Ng, Y. Zhao, *J. Mater. Chem. B* **2013**, *1*, 6495.

[24] C. Xu, D. Yang, L. Mei, Q. Li, H. Zhu, T. Wang, *ACS Appl. Mater. Interfaces* **2013**, *5*, 12911.

[25] S. Mao, G. Lu, K. Yu, Z. Bo, J. Chen, *Adv. Mater.* **2010**, *22*, 3521.

[26] S. He, K.-K. Liu, S. Su, J. Yan, X. Mao, D. Wang, Y. He, L.-J. Li, S. Song, C. Fan, *Anal. Chem.* **2012**, *84*, 4622.

[27] K. Balasubramanian, L. Zuccaro, K. Kern, *Adv. Funct. Mater.* **2014**, *24*, 6348.

[28] F. Schedin, E. Lidorikis, A. Lombardo, V. G. Kravets, A. K. Geim, A. N. Grigorenko, K. S. Novoselov, A. C. Ferrari, *ACS Nano* **2010**, *4*, 5617.

[29] H. Zhou, C. Qiu, Z. Liu, H. Yang, L. Hu, J. Liu, H. Yang, C. Gu, L. Sun, *J. Am. Chem. Soc.* **2010**, *132*, 944.

[30] Y. Liu, Y. Hu, J. Zhang, *J. Phys. Chem. C* **2014**, *118*, 8993.

[31] W. Xu, J. Xiao, Y. Chen, Y. Chen, X. Ling, J. Zhang, *Adv. Mater.* **2013**, *25*, 928.

[32] S. Heeg, R. Fernandez-Garcia, A. Oikonomou, F. Schedin, R. Narula, S. A. Maier, A. Vijayaraghavan, S. Reich, *Nano Lett.* **2013**, *13*, 301.

[33] P. Wang, W. Zhang, O. Liang, M. Pantoja, J. Katzer, T. Schroeder, Y.-H. Xie, *ACS Nano* **2012**, *6*, 6244.

[34] Y. Zhao, Y. Xie, Z. Bao, Y. H. Tsang, L. Xie, Y. Chai, *J. Phys. Chem. C* **2014**, *118*, 11827.

[35] P. Blake, E. W. Hill, A. H. Castro Neto, K. S. Novoselov, D. Jiang, R. Yang, T. J. Booth, A. K. Geim, *Appl. Phys. Lett.* **2007**, *91*, 63124.

[36] L. Xie, X. Ling, Y. Fang, J. Zhang, Z. Liu, *J. Am. Chem. Soc.* **2009**, *131*, 9890.

[37] X. Ling, L. Xie, Y. Fang, H. Xu, H. Zhang, J. Kong, M. S. Dresselhaus, J. Zhang, Z. Liu, *Nano Lett.* **2010**, *10*, 553.

[38] K. A. Willets, R. P. Van Duyne, *Annu. Rev. Phys. Chem.* **2007**, *58*, 267.

[39] C. Casiraghi, S. Pisana, K. S. Novoselov, A. K. Geim, A. C. Ferrari, *Appl. Phys. Lett.* **2007**, *91*, 233108.

[40] A. Das, S. Pisana, B. Chakraborty, S. Piscanec, S. K. Saha, U. V. Waghmare, K. S. Novoselov, H. R. Krishnamurthy, A. K. Geim, A. C. Ferrari, A. K. Sood, *Nat. Nanotechnol.* **2008**, *3*, 210.

[41] W. X. Wang, S. H. Liang, T. Yu, D. H. Li, Y. B. Li, X. F. Han, *J. Appl. Phys.* **2011**, *109*, 07C501.

[42] F. Ding, H. Ji, Y. Chen, A. Herklotz, K. Dörr, Y. Mei, A. Rastelli, O. G. Schmidt, *Nano Lett.* **2010**, *10*, 3453.

[43] M. Huang, H. Yan, T. F. Heinz, J. Hone, *Nano Lett.* **2010**, *10*, 4074.

[44] T. M. G. Mohiuddin, A. Lombardo, R. R. Nair, A. Bonetti, G. Savini, R. Jalil, N. Bonini, D. M. Basko, C. Galiotis, N. Marzari, K. S. Novoselov, A. K. Geim, A. C. Ferrari, *Phys. Rev. B* **2009**, *79*, 205433.

[45] Y. Wang, Z. Ni, H. Hu, Y. Hao, C. P. Wong, T. Yu, J. T. L. Thong, Z. X. Shen, *Appl. Phys. Lett.* **2010**, *97*, 163111.

[46] W. Xu, N. Mao, J. Zhang, *Small* **2013**, *9*, 1206.

[47] L. Olejko, P. J. Cywinski, I. Bald, *Nanoscale* **2016**, *8*, 10339.

[48] J. Wirth, F. Garwe, G. Hähnel, A. Csáki, N. Jahr, O. Stranik, W. Paa, W. Fritzsche, *Nano Lett.* **2011**, *11*, 1505.

[49] J. J. Toppari, J. Wirth, F. Garwe, O. Stranik, A. Csaki, J. Bergmann, W. Paa, W. Fritzsche, *ACS Nano* **2013**, *7*, 1291.

[50] M. Huang, H. Yan, C. Chen, D. Song, T. F. Heinz, J. Hone, *Proc. Natl. Acad. Sci. USA* **2009**, *106*, 7304.

[51] E. M. S. Stennett, M. A. Ciuba, M. Levitus, *Chem. Soc. Rev.* **2014**, *43*, 1057.

[52] A. O. Govorov, H. H. Richardson, *Nano Today* **2007**, *2*, 30.

[53] C. G. Hübner, A. Renn, I. Renge, U. P. Wild, *J. Chem. Phys.* **2001**, *115*, 9619.

[54] I. Rasnik, S. A. McKinney, T. Ha, *Nat. Methods* **2006**, *3*, 891.

[55] L. G. Cançado, A. Jorio, E. H. M. Ferreira, F. Stavale, C. A. Achete, R. B. Capaz, M. V. O. Moutinho, A. Lombardo, T. S. Kulmala, A. C. Ferrari, *Nano Lett.* **2011**, *11*, 3190.

[56] H. H. Richardson, M. T. Carlson, P. J. Tandler, P. Hernandez, A. O. Govorov, *Nano Lett.* **2009**, *9*, 1139.

[57] J. B. Knudsen, L. Liu, A. L. B. Kodal, M. Madsen, Q. Li, J. Song, J. B. Woehrstein, S. F. J. Wickham, M. T. Strauss, F. Schueder, J. Vinther, A. Krissanaprasit, D. Gudnason, A. A. A. Smith, R. Ogaki, A. N. Zelikin, F. Besenbacher, V. Birkedal, P. Yin, W. M. Shih, R. Jungmann, M. Dong, K. V. Gothelf, *Nat. Nanotechnol.* **2015**, *10*, 892.

[58] X. Ling, L. G. Moura, M. A. Pimenta, J. Zhang, *J. Phys. Chem. C* **2012**, *116*, 25112.

[59] B. Ding, Z. Deng, H. Yan, S. Cabrini, R. N. Zuckermann, J. Bokor, *J. Am. Chem. Soc.* **2010**, *132*, 3248.

CrossMark

Transparent and conductive films from liquid phase exfoliated graphene

**Tijana Tomašević-Ilić[1] · Jelena Pešić[1] · Ivana Milošević[1] ·
Jasna Vujin[1] · Aleksandar Matković[1] · Marko Spasenović[1] ·
Radoš Gajić[1]**

Abstract We describe transparent and conductive films of liquid-phase exfoliated graphene deposited with the Langmuir–Blodgett (LB) method. Graphene sheets (GS) were exfoliated from graphite by ultrasonic treatment in N-Methyl-2-pyrrolidone (NMP) and N, N-dimethylacetamide (DMA) solvents. For comparison, graphene sheets were also exfoliated in a water solution of surfactants. We confirm a higher exfoliation rate for surfactant-based processing compared to NMP and DMA. Furthermore, we demonstrate that our films exfoliated in NMP and DMA, deposited with LB and annealed have a higher optical transmittance and lower sheet resistance compared to films obtained with vacuum filtration, which is a necessary step for GS exfoliated in water solutions. The structural, optical and electrical properties of graphene layers were characterized with scanning electron microscopy, atomic force microscopy, UV/VIS spectrophotometry and sheet resistance measurements. Our facile and reproducible method results in high-quality transparent conductive films with potential applications in flexible and printed electronics and coating technology.

Keywords Graphene · LPE · Langmuir–Blodgett assembly

1 Introduction

Transparent conductors are an essential part of many optical devices. Many of the thin metallic or metal oxide films used as transparent conductors (Granqvist 2007) exhibit nonuniform absorption across the visible spectrum (Phillips et al. 1994), or they are

✉ Tijana Tomašević-Ilić
   ttijana@ipb.ac.rs

[1] Center for Solid State Physics and New Materials, Institute of Physics, University of Belgrade, Pregrevica 118, 11080 Belgrade, Serbia

🙋 Springer

chemically unstable, or both (Scott et al. 1996; Schlatmann et al. 1996). The experimental discovery of graphene (Novoselov et al. 2004) brought a new alternative to this field. Graphene is a material with high optical transparency, large carrier mobility, good chemical stability, and mechanical strength, making it an excellent choice for transparent electrodes in various optoelectronic devices (Blake et al. 2008).

Although graphene is a natural choice for transparent conductive films (Bonaccorso et al. 2010), the feasibility of its mass production is essential for applications. In order to produce large quantities of graphene Blake et al. (Blake et al. 2008) and Hernandez et al. (2008) developed a method of graphene production using solvent assisted exfoliation (or liquid phase exfoliation, LPE) of bulk graphite, which is simpler and less costly than chemical vapor deposition and returns a higher yield than mechanical exfoliation (Novoselov et al. 2004, 2005). LPE allows the possibility to scale up the synthesis of graphene making it economically available in a large amount, presenting a promising route for large-scale production (Paton et al. 2014).

Numerous research efforts followed up to increase the concentration and quality of the graphene flakes produced. One of the most promising synthesis routes for LPE graphene is non-covalent exfoliation using solvents that have surface energy values comparable to that of graphite (Hernandez et al. 2008). Typically ultrasound assists the separation of graphene flakes from graphite powder in solvent. Exfoliation conditions such as the initial concentration of graphite powder, sonication time (Khan et al. 2010), solvent type (O'Neill et al. 2011; Bourlinos et al. 2009; Hernandez et al. 2010; Lotya et al. 2009; Guardia et al. 2011), and possible filtration (Khan et al. 2011) were tuned in order to optimize the yield and quality of graphene dispersions. These graphene dispersions can be used to form films by various methods, for example spray coating (Blake et al. 2008), vacuum filtration (Hernandez et al. 2008; Lotya et al. 2009) or Langmuir–Blodgett assembly (LBA) (Cote 2009; Kim et al. 2013; Li et al. 2008).

In this study, graphene sheets (GS) were exfoliated from graphite by ultrasonic treatment in organic solvents with high boiling points, N-Methyl-2-pyrrolidone (NMP), N, N-dimethylacetamide (DMA), and for comparison, in a water solution of surfactant, sodium dodecylbenzenesulfonate (SDBS) and Pluronic P-123 (P-123). The graphene dispersions from NMP and DMA were used to form films by controlled deposition of few-layer graphene using the Langmuir–Blodgett (LB) method on a water–air interface. We confirm a higher exfoliation rate for surfactant-based processing, but demonstrate that our films exfoliated in organic solvents with high boiling points and deposited with LB have a higher optical transmittance and lower sheet resistance compared to films obtained with vacuum filtration, which is a necessary step for GS exfoliated in water solutions. The structural, optical and electrical properties of graphene layers were characterized with scanning electron microscopy, atomic force microscopy, UV/VIS spectrophotometry and sheet resistance measurements.

2 Experimental procedure

All chemicals used were purchased from Sigma Aldrich: graphite powder (product number 332461), N-Methyl-2-pyrrolidone (product number 328634), N, N-dimethylacetamide (product number 38840), sodium dodecylbenzenesulfonate (product number 289957) and Pluronic P-123 (product number 435467). The particular graphite powder product was chosen for its large initial flake size, which should result in the largest possible graphene

flakes after exfoliation. Stock solutions of SDBS and P-123 of different concentrations were prepared in deionized water (resistivity 18 MΩ) by stirring overnight. A range of graphene dispersions were prepared. A typical sample was prepared by dispersing graphite in the desired solvent using from 30 min to 14 h of sonication in a low power sonic bath. The resulting dispersion was centrifuged for 60 min at 3000 rpm in order to reduce the amount of unexfoliated graphite.

The graphene sheets exfoliated from graphite by ultrasonic treatment in NMP were used to form films at a water–air interface. Beakers filled with deionized water, 10 mL volume, were used for film formation. A 1.5–2 vol% of GS + NMP was added to the interface with a continuous flow rate of 5–10 mL/s (Fig. 1a). This set of parameters provides enough surface pressure for the film to be close-packed. After the film is formed, it is slowly scooped onto the targeted substrate (Fig. 1b), as shown in our previous work (Matković et al. 2016). PET and SiO$_2$/Si were used as substrates. As it has been shown that annealing decreases sheet resistance due to solvent evaporation (Hernandez et al. 2008; Lotya et al. 2009), some of these deposited films were annealed. Annealing was carried out in a tube furnace at 250 °C in an argon atmosphere for 2 h.

For optical characterization, UV–VIS spectra were taken using a SUPER SCAN Varian spectrophotometer with quartz cuvettes. The resistance of each sample was measured in a two-point probe configuration, and the sheet resistance was obtained by including the sample geometry factors. AFM measurements were taken with an atomic force micro-scope, NTEGRA Spectra, in tapping mode. SiO$_2$/Si was chosen as a substrate for AFM due to its low surface roughness. The lateral profile of graphene flakes was analyzed with a Tescan MIRA3 field-emission gun SEM.

3 Results and discussion

We optimized for high graphene concentration and large flake size, tuning exfoliation conditions such as initial graphite concentration, sonication time and solvent type. The Lambert–Beer law was applied to UV–VIS absorption spectra to find graphene concen-tration. The concentration was estimated from the absorbance at 660 nm by using the extinction coefficient of graphene ($\alpha = 13.90$ mL mg^{-1} m^{-1}) previously determined in surfactant/water solutions (Hernandez et al. 2008; Lotya et al. 2009; Guardia et al. 2011) and ($\alpha = 24.60$ mL mg^{-1} m^{-1}) in NMP and DMA solutions (Hernandez et al. 2008). Figure 2a depicts a higher final concentration for surfactant-based processing for all initial concentrations of graphite powder, from 0.5 to 18 mg mL^{-1}. The most commonly used deposition technique for LPE GS is vacuum filtration. This is a necessary step for GS exfoliated in water solutions. For GS films formed by evaporation of a high boiling point

Fig. 1 Schematic representations of **a** LBA GS film formation, **b** scooping of the film onto a targeted substrate
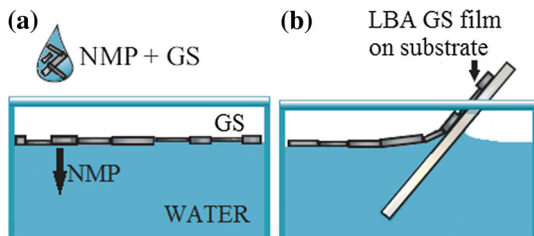
solvent, one of the biggest problems is that graphene flakes aggregate during evaporation (O'Neill et al. 2011) hindering fine control over the film thickness (Hernandez et al. 2008). This can be avoided by depositing with LB, which allows reliable and reproducible thickness control and prevents further agglomeration of graphene flakes during drying (Kim et al. 2013). We chose the dispersion in NMP with the highest graphene concentration (Fig. 2b) for experiments on LB films.

A single LB deposition resulted in films with an average thickness 3.3 nm, as measured with AFM, indicating an average GS thickness of 10 layers (Fig. 3).

Figure 4 shows optical transmittance versus sheet resistance for varying number of LB depositions on PET, compared to graphene film obtained with vacuum filtration of GS exfoliated from the same graphite precursor using the same experimental procedure (Hernandez et al. 2008; Lotya et al. 2009) before and after annealing. The highest transparency for a single LB film deposition prior to annealing was found to be about 83 %, which is between 20 and 40 % higher than the transmittance that can be accomplished with vacuum-filtration. The sheet resistance of one LB film deposition is between 70 and 250 kΩ/sq, 2–5 times lower than sheet resistance achieved with vacuum filtration without annealing. Increasing the graphene film thickness with additional LB depositions led to consistent increases in conductivity, but a decrease in transparency. Our graphene films for three LB depositions prior to annealing have comparable sheet resistance but higher optical transmittance compared to vacuum-filtered films after annealing.

The electrical conductivity is affected by the size and connectivity of the flakes as well as the thickness of the films. Our average GS diameter was is 120 nm, as measured with SEM (Fig. 5). SEM also revealed the presence of pinholes between flakes for a single LB deposition, which probably results in parasitic sheet resistance (Fig. 5a). In order to remove the residual solvent between the overlapping flakes, which may affect transport, we employed thermal annealing. Annealing does not repair the holes and other irreversible defects (Fig. 5b), but it can remove residual solvents, improving the coupling between graphene flakes and hence decreasing sheet resistance. For a single LB deposition, annealing reduced sheet resistance by about six times, without considerably decreasing transparency (Fig. 4). The sheet resistance of a singly deposited film after annealing was found to be between 10 and 20 kΩ/sq, a significant improvement over other published data. After annealing we performed a second LB deposition and achieved sheet resistance of
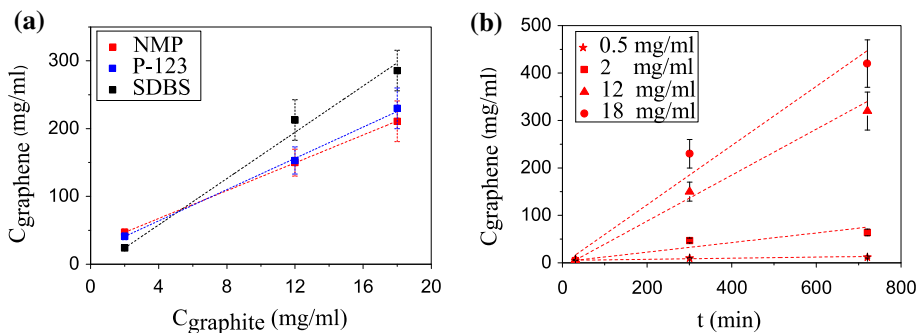

Fig. 2 Concentration of dispersed graphene: **a** in different solutions for different initial graphite concentration and sonication time of 5 h, **b** in NMP for different sonication time and different initial graphite concentration
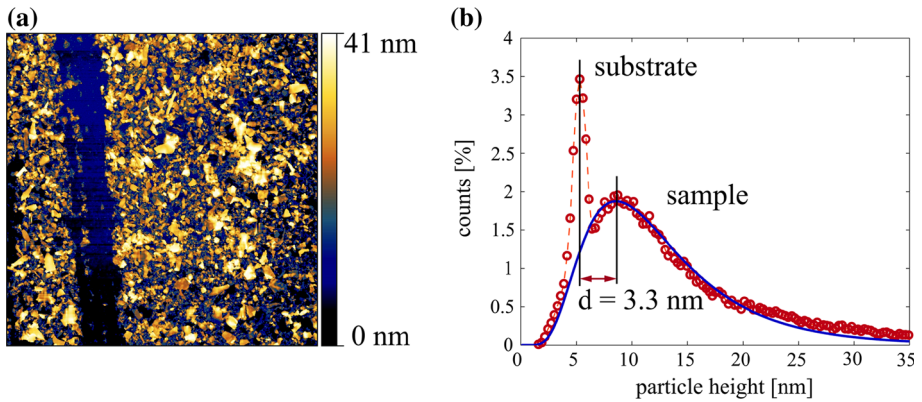
Fig. 3 **a** AFM image of a LB graphene film on a SiO$_2$/Si substrate, **b** an LB GS film/substrate height histogram fitted with a log-normal curve
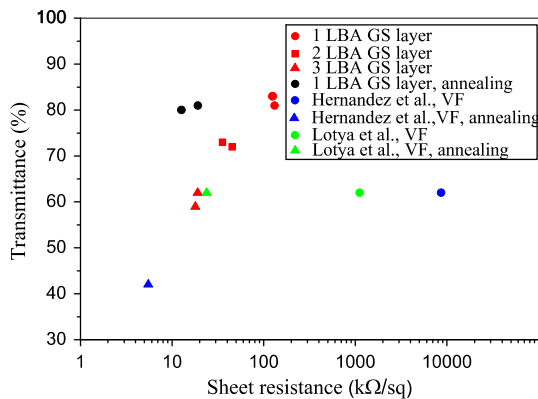

Fig. 4 Optical transmittance versus sheet resistance for varying number of LB deposition of graphene sheets on PET exfoliated in NMP before (*red*) and after annealing (*black*), compared to graphene films obtained with vacuum filtration in the same solvent (*blue*) (Hernandez et al. 2008) and graphene films obtained with vacuum filtration in surfactant/water solutions (*green*) (Lotya et al. 2009) before and after annealing. (Color figure online)
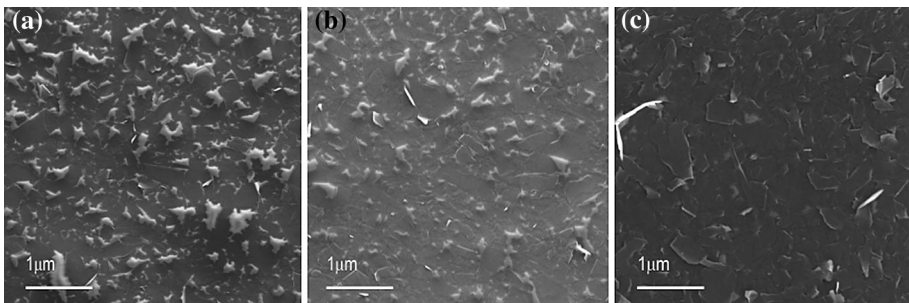

Fig. 5 SEM images of: **a** singly deposited LB film on a glass substrate, **b** the same film after annealing, **c** two LB depositions with an annealing step in between

3 kΩ/sq and a transparency of more than 70 %. Decreased resistance is the result of reduced density of pinholes (Fig. 5c) as well as increased film thickness.

4 Conclusion

In summary, we have shown that Langmuir–Blodgett assembly of multi-layer graphene sheets produced from liquid phase exfoliation of graphite powder in solvents can be used to fabricate transparent and conductive films. The sheet resistance of deposited LBA GS layers was found to be between 15 and 250 kΩ/sq, with transmittance between 60 and 85 %, depending on the number of deposited LBA graphene layers. The conductivity of these LBA films can be further increased by about six times with annealing, without considerably decreasing transparency. Optoelectronic properties of these films are much better compared to graphene films obtained with vacuum filtration of GS exfoliated with the same experimental procedure, which is the most commonly used deposition technique for LPE GS. Ours is a facile, reproducible and low-cost technique for transparent conductive films with potential applications in coating technology.

References

Blake, P., et al.: Graphene-based liquid crystal device. Nano Lett. **8**, 1704–1708 (2008)

Bonaccorso, F., et al.: Graphene photonics and optoelectronics. Nat. Photonics **4**, 611–622 (2010)

Bourlinos, A.B., et al.: Liquid-phase exfoliation of graphite towards solubilized graphenes. Small **5**, 1841–1845 (2009)

Cote, L.J.: Langmuir–Blodgett assembly of graphite oxide single layers. J. Am. Chem. Soc. **131**, 1043–1049 (2009)

Granqvist, C.G.: Transparent conductors as solar energy materials: a panoramic review. Sol. Energy Mater. Sol. Cells **91**, 1529–1598 (2007)

Guardia, L., et al.: High-throughput production of pristine grapheme in an aqueous dispersion assisted by non-ionic surfactants. Carbon **49**, 1653–1662 (2011)

Hernandez, Y., et al.: High-yield production of graphene by liquid-phase exfoliation of graphite. Nat. Nanotechnol. **3**, 563–568 (2008)

Hernandez, Y., et al.: Measurement of multicomponent solubility parameters for graphene facilitates solvent discovery. Langmuir **26**, 3208–3213 (2010)

Khan, U., et al.: High-concentration solvent exfoliation of graphene. Small **6**, 864–871 (2010)

Khan, U., et al.: Solvent-exfoliated graphene at extremely high concentration. Langmuir **27**, 9077–9082 (2011)

Kim, H.K., et al.: Optoelectronic properties of graphene thin films deposited by a Langmuir–Blodgett assembly. Nanoscale **5**, 12365–12374 (2013)

Li, X., et al.: Highly conducting graphene sheets and Langmuir–Blodgett films. Nat. Nanotechnol. **3**, 538–542 (2008)

Lotya, M., et al.: Liquid phase production of graphene by exfoliation of graphite in surfactant/water solutions. J. Am. Chem. Soc. **131**, 3611–3620 (2009)

Matković, A., et al.: Enhanced sheet conductivity of Langmuir-Blodgett assembled graphene thin films by chemical doping. 2D Mater. **3**(1), 015002 (2016)

Novoselov, K.S., et al.: Electric field effect in atomically thin carbon. Science **306**, 666–669 (2004)

Novoselov, K.S., et al.: Two-dimensional atomic crystals. Natl. Acad. Sci. U.S.A. **102**, 10451–10453 (2005)

O'Neill, A., et al.: Graphene dispersion and exfoliation in low boiling point solvents. J. Phys. Chem. C **115**, 5422–5428 (2011)

Paton, K.R., et al.: Scalable production of large quantities of defect-free few-layer graphene by shear exfoliation in liquids. Nat. Mater. **13**, 624–630 (2014)

Phillips, J.M., et al.: Transparent conducting thin films of GalnO3. Appl. Phys. Lett. **65**, 115–117 (1994)

Schlatmann, A.R., et al.: Indium contamination from the indium–tin–oxide electrode in polymer light emitting diodes. Appl. Phys. Lett. **69**, 1764–1766 (1996)

Scott, J.C., et al.: Degradation and failure of MEH-PPV light-emitting diodes. J. Appl. Phys. **79**, 2745–2751 (1996)

Република Србија
Универзитет у Београду
Физички факултет
Д.Бр.2012/8037
Датум: 06.02.2017. године

На основу члана 161 Закона о општем управном поступку и службене евиденције издаје се

УВЕРЕЊЕ

Пешић (Радмило) Јелена, бр. индекса 2012/8037, рођена 17.12.1986. године, Београд, Београд-Савски Венац, Република Србија, уписана школске 2016/2017. године, у статусу: самофинансирање; тип студија: докторске академске студије; студијски програм: Физика.

Према Статуту факултета студије трају (број година): три.
Рок за завршетак студија: у двоструком трајању студија.

Ово се уверење може употребити за регулисање војне обавезе, издавање визе, права на дечији додатак, породичне пензије, инвалидског додатка, добијања здравствене књижице, легитимације за повлашћену вожњу и стипендије.

Овлашћено лице факултета

На основу члана 82. Закона о научноистраживачкој делатности ("Службени гласник Републике Србије", број 110/2005, 50/2006 - испр. и 18/2010), члана 33. тачка 5. Статута Института за физику и захтева који је поднела

ЈЕЛЕНА ПЕШИЋ

на седници Научног већа Института за физику одржаној 23.12.2014. године, донета је

ОДЛУКА
О СТИЦАЊУ ИСТРАЖИВАЧКОГ ЗВАЊА

ЈЕЛЕНА ПЕШИЋ
стиче истраживачко звање
Истраживач сарадник

ОБРАЗЛОЖЕЊЕ

Јелена Пешић је 20.10.2014. године поднела захтев за стицање истраживачког звања истраживач сарадник. Научно веће Института за физику је на седници одржаној 28.10.2014. године образовало Комисију за спровођење поступка у саставу др Радош Гајић, научни саветник у Институту за физику, др Владимир Дамљановић, научни сарадник у Институту за физику и др Горан Попарић, ванредни професор на Физичком факултету у Београду. Научно веће је на седници од 23.12.2014. године утврдило да именована испуњава услове из члана 70. став 3. Закона о научноистраживачкој делатности за стицање истраживачког звања **истраживач сарадник,** па је одлучило као у изреци ове одлуке.

Одлуку доставити подносиоцу, архиви Института за физику, кадровској служби Института за физику и рачуноводственој служби Института за физику.

Председник Научног већа
др Жељка Никитовић

Директор Института за физику
др Александар Богојевић